

**N^* Resonances in Pseudoscalar-meson photo-production
from Polarized Neutrons in $\vec{H} \cdot \vec{D}$
and a complete determination of the $\gamma n \rightarrow K^0 \Lambda$ amplitude**

Collaboration

K. Ardashev¹⁸, N. Benmouna⁷, M. Blecher¹⁹, D. Branford⁵, W. Briscoe⁷, V. Burkert¹²,
P. Cole²⁰, V. Crede²¹, A. D'Angelo¹³, D.S. Dale²⁰, R. Di Salvo¹⁴, A. Fantini¹⁴, R. Gothe¹⁷,
K. Hicks¹¹, S. Hoblit², D. Ireland¹⁶, B. Juliá-Díaz¹⁵, T. Kageya¹⁹, J. Kellie¹⁶, M. Khandaker¹⁰,
O.C. Kistner², F. Klein⁴, T.S.-H. Lee¹, P. Levi Sandri⁹, R. Lindgren¹⁸, K. Livingston¹⁶,
M. Lowry², J. Mahon¹¹, L. Miceli², D. Moricciani¹⁴, B. Norum¹⁸, J. Price³, G. Rosner¹⁶,
A.M. Sandorfi², C. Schaerf¹³, D. Sober⁴, I. Strakovsky⁷, S. Strauch¹⁷, H. Ströher⁶,
D. Tedeschi¹⁷, C. Thorn², X. Wei², K. Wang¹⁸, D. Watts⁵, C.S. Whisnant⁸ and R. Workman⁷

and

the CLAS Collaboration

- ¹Argonne National Laboratory, Argonne, IL 60439
- ²Brookhaven National Laboratory, Upton, NY 11973
- ³California State University at Dominguez Hills, Caeson, CA 90747
- ⁴Catholic University of America, Washington, DC 20064
- ⁵Edinburgh University, Edinburgh EH9-3JZ, UK
- ⁶Forschungszentrum Jülich, D-52425 Jülich, Germany
- ⁷George Washington University, Washington, DC 20052
- ⁸James Madison University, Harrisonburg, VA 22807
- ⁹Laboratori Nazionali di Frascati-INFN, Frascati 000044, Italy
- ¹⁰Norfolk State University, Norfolk, VA 23504
- ¹¹Ohio University, Athens, OH 45701
- ¹²Thomas Jefferson National Accelerator Facility, Newport News, VA 23606
- ¹³Universita di Roma-“Tor Vergata” and INFN-Sezione di Roma 2, Rome, Italy
- ¹⁴INFN-Sezione di Roma 2, Rome, Italy
- ¹⁵Universitat de Barcelona, 08028 Barcelona, Spain
- ¹⁶University of Glasgow, Glasgow G12-8QQ, UK
- ¹⁷University of South Carolina, Columbia, SC 29208
- ¹⁸University of Virginia, Charlottesville, VA 22904
- ¹⁹Virginia Polytechnic Institute & State University, Blacksburg, VA 24061
- ²⁰Idaho State University, Pocatello, ID 83209
- ²¹Florida State University, Tallahassee, FL 32306

Abstract

The internal structure of the nucleon, as manifested in its excitation spectrum, has presented a crucial challenge to nuclear and elementary-particle physics. The quark model predicts many resonances that appear to be *missing* from the spectrum of πN states. However, the quark model also predicts a rapid decrease with energy in the $G_{\pi N}$ coupling for the states in each oscillator band. Higher mass states may couple to other pseudoscalar meson channels such as $\pi\pi N$, ΔN , ρN , ωN , ηN , $K\Lambda$ or $K\Sigma$. Alternatively, other models involving diquarks or phase transitions have been proposed to account for the current baryon spectrum, which is chiefly determined from πN reactions. The apparent success of such alternatives questions the effective degrees of freedom within the nucleon.

Higher mass resonances are generally overlapping with significant interfering backgrounds from u -channel processes. As a result, their properties cannot be extracted without detailed partial-wave analyses, preferably in a frame-work which accounts for the coupling between the various meson-decay channels. Constraining such analyses requires a large number of polarization observables. This has not been achieved in any channel, despite nearly 50 years of research into πN scattering and photo-production. Most of the available data has been taken with proton targets and a new set of polarized target experiments will soon expand this data base at JLab. In contrast, the available neutron data is extremely sparse. While $I = 3/2$ Δ resonances can be determined from proton data alone, $I = 1/2$ N^* resonances necessarily require *both* neutron and proton data.

We propose to measure a suite of pseudoscalar-meson photo-production reactions using circularly and linearly polarized beams on a longitudinally polarized deuterium target. We have considered two possible frozen-spin targets, a deuterated-butanol version of the FROST target now under construction at JLab and the HD target which has been developed at BNL, and have carried out detailed simulations for each. Since anticipated running times with Butanol are factors of 50-90 times longer, depending on kinematics, we plan to use a polarized HD target.

Asymmetries from *free* neutrons will be isolated by kinematically restricting the meson-baryon decay. Beam-target double-polarization asymmetries for the π^+p , $\pi^+\pi^-n$, $K^0\Lambda$, $K^0\Sigma^0$ and $K^+\Sigma^-$ channels will all be measured simultaneously. Since the weak decay of the hyperons

provides an analysis of their recoil polarization, target-recoil and beam-recoil data will also be measured for those channels. The simultaneous measurement of beam-recoil asymmetries from the neutron, using the same kinematic restrictions, is possible because the target molecule contains a single neutron in deuterium and the small contaminations from non-HD material in the beam path can be subtracted from concurrent empty cell measurements.

The recoil analyzing power in Λ decay is appreciable and this provides a unique opportunity. For the $\gamma n \rightarrow K^0 \Lambda$ reaction, a total of 13 different polarization observables will be determined in a single experiment, including single-polarization and beam-target, target-recoil and beam-recoil double-polarization asymmetries, along with the cross section. This will provide the first (over-) determination of a pseudoscalar meson photo-production amplitude and will be free of the PWA ambiguities that have plagued this field for decades.

A small fraction of running is also planned for polarized H which will verify the effectiveness of kinematic requirements in the extraction of neutron observables, by comparing *free* protons in H and *bound* protons in D, and set limits on possible corrections to the neutron asymmetries from deuteron tensor observables. At the same time, this will provide polarized proton data on beam-target and target-recoil asymmetries taken under the same conditions and so create a uniquely large data set on both isospin channels that is locked together with common systematics. When combined with other proton beam-recoil measurements, this will determine the complete $\gamma N \rightarrow K \Lambda$ isospin amplitude, free of ambiguities.

The total beam request for this experiment is 75 days with polarized $H\bar{D}$ and 10 with polarized $\bar{H}D$, for a total of 85 days.

Contents

	<i>page</i>
1 Motivation	6
1.1 Proposed Measurement of Polarization Observables	18
1.2 Extraction of <i>neutron</i> amplitudes	23
1.2.1 Empirical Analysis	23
1.2.2 Theoretical analysis	25
1.3 Polarized proton data runs	29
2 Monte Carlo Simulations	31
2.1 Studies of KY Channels	31
2.2 Backgrounds	34
2.3 Sample analyses	36
3 Experimental Parameters	54
3.1 Target Parameters	54
3.2 Photon Beam Parameters	55
3.3 Trigger	59
3.4 Count Rate Estimates	59
3.5 Beam Time Requirements for KY Channels	65
4 Simulations of $\gamma n \rightarrow \pi^+ \pi^- n$	70
5 Simulations of $\gamma n \rightarrow \pi^- p$	73
6 Discussion of Systematic Uncertainties	76
7 Summary of Beam Time Request	79
Appendix A: Description and Characteristics of the Frozen-Spin HD target	80
Appendix B: Relation to other photo-production experiments at JLab	96
References	99

1 Motivation

One of the most important and challenging topics in the intersection between nuclear and elementary-particle physics is the internal structure of the nucleon as revealed in its excitation spectrum. A complete characterization of the spectrum of N^* and Δ resonances is essential to understanding nucleon structure within QCD. Given the difficulty in evaluating the QCD Lagrangian, theoretical efforts have focused on identifying the effective degrees of freedom. While models with constituent quarks interacting via one-gluon exchange, Chiral models with Goldstone-boson exchange and Instanton models all have had some level of success in describing the resonance spectrum, many puzzles remain. Symmetric $SU(6) \times O(3)$ quark models predict many states presently *missing* from the baryon spectrum^[1], while such extra states are absent from *diquark* models in which two of the constituent quarks are tightly bound^[2]. While Lattice simulations have shown some evidence for such di-quark clusters, these are associated with large orbital angular momentum^[3]. Even a phase transition has been suggested as a mechanism that could reorganize the baryon spectrum into the present set of observed resonances^[4]. Models that attribute confinement to gluon flux tubes between quarks predict additional hybrid resonances that have yet to be identified convincingly.

Most recognized baryon states were initially discovered in πN scattering. It has been suggested that many quark model states may be missing from the current catalogue of resonances simply because they couple weakly to the πN channel^[5]. In fact, while the lowest-energy quark model state in each oscillator band couples strongly to πN , the πN coupling strengths tend to decrease rapidly as the masses of states increase^[1]. Photo-production of pseudo-scalar mesons is expected to be a very fruitful sector for the study of the baryon resonance spectrum and may yet reveal new states that couple to other decay channels such as $\pi\pi N$, ρN , ωN , ηN , $K\Lambda$ or $K\Sigma$ ^[6]. In fact, a structure recently observed in $\gamma p \rightarrow K^+ \Lambda$ with the SAPHIR detector at Bonn^[7] has been proposed as a new $D_{13}(\sim 1950)$ resonance, corresponding to the *missing* $[N_{\frac{3}{2}}^-]_3$ quark model state^[8]. The $\gamma p \rightarrow KY$ cross sections are plotted in Figure 1 together with predictions from two recent model calculations^[8, 9]. The candidate $D_{13}(1950)$ appears as a subtle inflection on the cross sections. The variations in the predicted $\gamma n \rightarrow KY$ cross sections are considerable, which largely

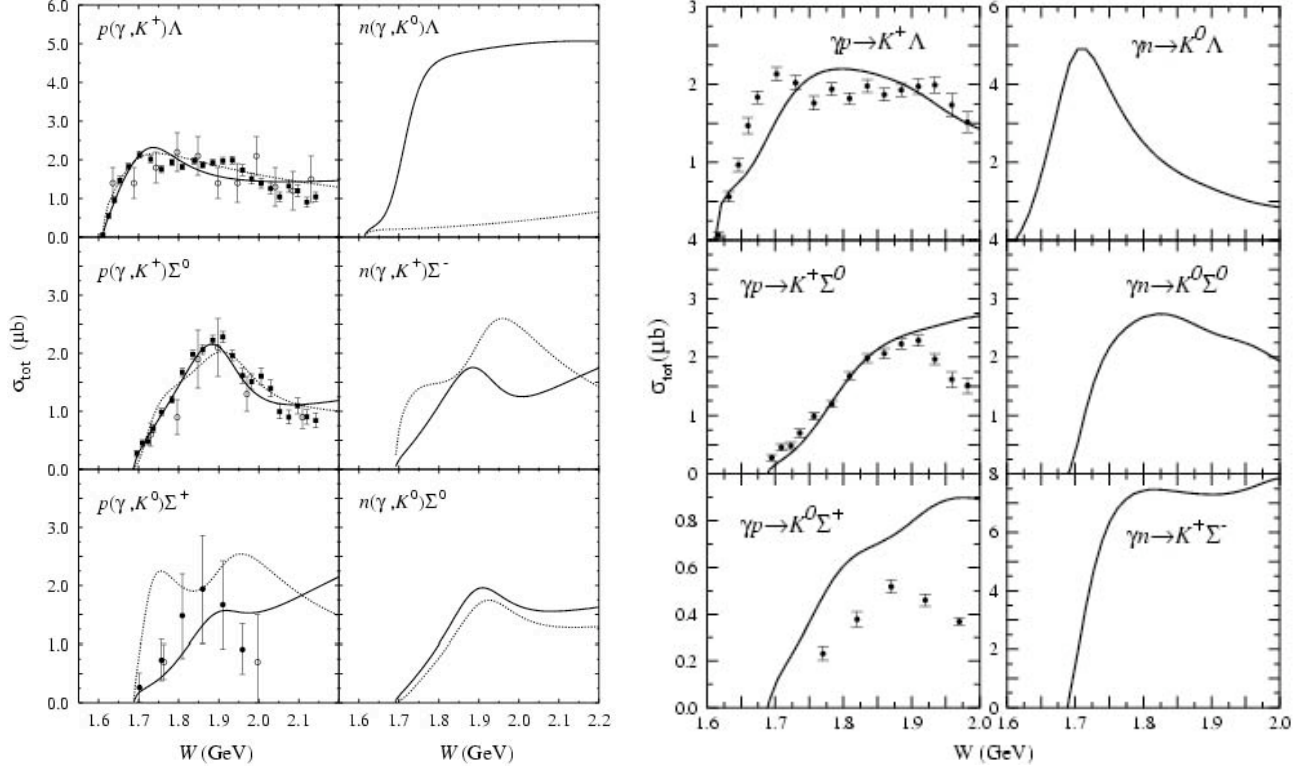


Figure 1. Cross section for Λ and Σ photoproduction from SAPHIR for $\gamma p \rightarrow KY$,^[10] compared with predictions from the isobar model by Mart and Bennhold^[8] (left two panels) and with the coupled-channel model by Waluyo and Bennhold^[9] (right two panels). Solid curves are the full calculations while dotted curves show the effect of excluding a $D_{13}(1950)$.

results from the lack of constraining data. Subsequently, in other partial wave analyses, this candidate resonance has appeared interfering strongly with the $P_{13}(1720)$ ^[11], moved in energy by 200 MeV^[12], disappeared altogether^[13], recently reappeared as a possible radial excitation of the $D_{13}(1520)$ ^[14] and appeared with a moderately strong signal in a new πN -KY coupled-channel analysis^[15].

There are several problems contributing to the variations in apparent results from partial wave analyses (PWA). First, resonances are generally broad and overlapping, with decay branches to many final states. Second, the very presence of an s -channel resonance guarantees contributions from the corresponding u -channel processes, which are non-resonant, contribute to large numbers of partial waves and interfere with other resonances. Third, cross sections alone do not define meson-production amplitudes and many polarization observables are needed to avoid ambiguities^[16]. For this, polarization asymmetries are particularly attractive since they are constructed as ratios of cross sections in which systematic uncertainties largely cancel. The

particular case of $\gamma p \rightarrow K^+ \Lambda$ analyses is in fact plagued by the comparison of cross section data from SAPHIR and from CLAS^[17], both of high statistics, but having 20% energy-dependent normalization differences between them; at the same time, very limited polarization data are available for this reaction – only recoil polarization from CLAS and some beam asymmetry points from LEPS^[18].

Since Kaon photo-production has considerably smaller cross sections than π production, multi-step processes such as $\gamma N \rightarrow \pi N \rightarrow KY$ are important and can even be comparable to the direct $\gamma N \rightarrow KY$ reaction. Coupled-channel PWA are needed to treat such interfering channels consistently and such fits require data on many channels, ideally taken simultaneously to lock data on different channels together with a common systematic uncertainty. The effects of channel coupling can be substantial. Juliá-Díaz, Saghai, Lee and Tabakin have carried out an analysis of the γN , πN and $K\Lambda$ channels and observed large multi-step contributions^[15] in the excitation of N^* resonances. They have reported evidence for the third S_{11} , P_{13} and D_{13} quark model candidates, with the $D_{13}(\sim 1950)$ giving the strongest indication, although the improvements in χ^2 are not dramatic, owing to the limited data available. The recent coupled-channel PWA by the Bonn-Gatchina (BOGA) collaboration^[14] included (σ, Σ, P) data for a restricted set of channels, $\gamma + p$ to $\pi^0 p$, $\pi^+ n$, ηp , $K^+ \Lambda$, $K^+ \Sigma^0$ and $K^0 \Sigma^+$ final states. They have reported three new N^* resonance candidates, a shift in the energy of a three-star P_{11} from the PDG value of 1710 to 1840 MeV (which would suggest a shift in the association of the corresponding quark model state to the $[N \frac{1}{2}^+]_4$) and, curiously, no evidence for a four-star G_{17} resonance that the PDG lists at 2190 MeV (although this is near the upper limit of their analyses)¹.

The identification of the nucleon's excited state spectrum and the coupling strengths of its resonances to meson decay channels are the benchmarks for testing models of the nucleon and identifying its effective internal degrees of freedom. But significant progress requires the elimination of ambiguities in the meson photo-production amplitudes that limit current analyses. This has been identified by the U.S. Nuclear Science Advisory Committee (*NSAC*) as a major milestone for the Department of Energy's Medium-Energy Physics program. Overcoming the

¹ This is not an unusual situation. The PDG gives a three star rating (*existence ranging from very likely to certain*) to a $P_{11}(1710)$, while the current SAID analysis see no trace of such a state in either πN scattering or photo-production.

present ambiguities requires a suite of polarization observables. A new campaign has begun at Jefferson Lab, with the goal of measuring single and double polarization asymmetries in π , η and K photo-production from the proton (E03-105/E01-104, E05-012, E02-112, E06-013). The JLab program of approved experiments with a polarized proton target (Butanol), which is now under development, can accomplish this for the spectrum of $I=3/2$ Δ states. However, for the $I=1/2$ N^* states those experiments alone will be inconclusive. The amplitudes for photo-producing pseudoscalar mesons have three components, which arise from the iso-scalar and iso-vector nature of the photon field. For $\gamma + p$ reactions, these can be written:

$$\begin{aligned}
\mathbf{A}_{\gamma p \rightarrow \begin{pmatrix} \pi^0 p \\ K^+ \Sigma^0 \end{pmatrix}} &= \mp \left[\frac{1}{\sqrt{3}} \mathbf{A}_{\begin{pmatrix} \pi N \\ K \Sigma \end{pmatrix}}^{(0)} - \frac{1}{3} \mathbf{A}_{\begin{pmatrix} \pi N \\ K \Sigma \end{pmatrix}}^{(1)} \right]^{(I=1/2)} + \frac{2}{3} \mathbf{A}_{\begin{pmatrix} \pi N \\ K \Sigma \end{pmatrix}}^{(I=3/2)} \\
\mathbf{A}_{\gamma p \rightarrow \begin{pmatrix} \pi^+ n \\ K^0 \Sigma^+ \end{pmatrix}} &= \pm \sqrt{2} \left[\frac{1}{\sqrt{3}} \mathbf{A}_{\begin{pmatrix} \pi N \\ K \Sigma \end{pmatrix}}^{(0)} - \frac{1}{3} \mathbf{A}_{\begin{pmatrix} \pi N \\ K \Sigma \end{pmatrix}}^{(1)} \right]^{(I=1/2)} + \frac{\sqrt{2}}{3} \mathbf{A}_{\begin{pmatrix} \pi N \\ K \Sigma \end{pmatrix}}^{(I=3/2)} \\
\mathbf{A}_{\gamma p \rightarrow \begin{pmatrix} \eta p \\ K^+ \Lambda \end{pmatrix}} &= + \left[\mathbf{A}_{\begin{pmatrix} \eta N \\ K \Lambda \end{pmatrix}}^{(0)} - \frac{1}{\sqrt{3}} \mathbf{A}_{\begin{pmatrix} \eta N \\ K \Lambda \end{pmatrix}}^{(1)} \right]^{(I=1/2)} .
\end{aligned} \tag{1.1}$$

Here, the $\mathbf{A}^{(0)}$ and $\mathbf{A}^{(1)}$ components result from coupling the $I=1/2$ nucleon with iso-scalar and iso-vector components of the photon field² to yield a total isospin of $1/2$. The terms in the square brackets are the projections of the isospin $1/2$ amplitudes onto the proton. These $I=1/2$ combinations are the same for the different charge channels of π or K production from a proton target. As such, measurements of two charge channels in π or K production from protons alone are sufficient to isolate the $I=3/2$ amplitudes which characterize the Δ states. But such proton data are insufficient to disentangle $\mathbf{A}^{(0)}$ and $\mathbf{A}^{(1)}$. For that, neutron data is required. Similarly, two isospin amplitudes contribute to either η or Λ production and only one linear combination can be

² Here we use the standard particle physics convention in which the positively charged member of a multiplet is assigned the positive value for I_3 . (This differs from some PDG sign conventions.)

accessed with a proton target. The two isospin $\frac{1}{2}$ amplitudes appear with different signs in photo-production from neutron and proton targets.

$$\begin{aligned}
\mathbf{A}_{\gamma n \rightarrow \begin{pmatrix} \pi^0 n \\ K^0 \Sigma^0 \end{pmatrix}} &= \pm \left[\frac{1}{\sqrt{3}} \mathbf{A}_{\begin{pmatrix} \pi N \\ K \Sigma \end{pmatrix}}^{(0)} + \frac{1}{3} \mathbf{A}_{\begin{pmatrix} \pi N \\ K \Sigma \end{pmatrix}}^{(1)} \right]^{(I=\frac{1}{2})} + \frac{2}{3} \mathbf{A}_{\begin{pmatrix} \pi N \\ K \Sigma \end{pmatrix}}^{(I=\frac{3}{2})} \\
\mathbf{A}_{\gamma n \rightarrow \begin{pmatrix} \pi^- p \\ K^+ \Sigma^- \end{pmatrix}} &= \mp \sqrt{2} \left[\frac{1}{\sqrt{3}} \mathbf{A}_{\begin{pmatrix} \pi N \\ K \Sigma \end{pmatrix}}^{(0)} + \frac{1}{3} \mathbf{A}_{\begin{pmatrix} \pi N \\ K \Sigma \end{pmatrix}}^{(1)} \right]^{(I=\frac{1}{2})} + \frac{\sqrt{2}}{3} \mathbf{A}_{\begin{pmatrix} \pi N \\ K \Sigma \end{pmatrix}}^{(I=\frac{3}{2})} \\
\mathbf{A}_{\gamma n \rightarrow \begin{pmatrix} \eta n \\ K^0 \Lambda \end{pmatrix}} &= + \left[\mathbf{A}_{\begin{pmatrix} \eta N \\ K \Lambda \end{pmatrix}}^{(0)} + \frac{1}{\sqrt{3}} \mathbf{A}_{\begin{pmatrix} \eta N \\ K \Lambda \end{pmatrix}}^{(1)} \right]^{(I=\frac{1}{2})} .
\end{aligned} \tag{1.2}$$

Confronting models of $I = \frac{1}{2}$ N^* resonances requires a separation of the $\mathbf{A}^{(0)}$ and $\mathbf{A}^{(1)}$ amplitudes and this can only be accomplished with data from *both* neutrons and protons. These two $I = \frac{1}{2}$ components determine the coupling strengths to N^* states and, in fact, it is their difference that drives the spin-sum rules (GDH for example) to different values for the proton and neutron. A determination of the $\mathbf{A}^{(0)}$ and $\mathbf{A}^{(1)}$ amplitudes is essential to constrain models of the nucleon and for that, neutron data are essential.

The available cross section data from a neutron target are very sparse, even for π -production. Between 0.4 and 2.0 GeV there are 1381 cross section points for $\gamma n \rightarrow \pi^- p$ and 108 points for the $\gamma n \rightarrow \pi^0 n$ channel. At the same time there are only 326 single-polarization (Σ , T , P) data points for $\gamma n \rightarrow \pi^- p$, none at all for $\gamma n \rightarrow \pi^0 n$ and no double-polarization data for either charge channel. As a result, the neutron production amplitudes have large uncertainties, even in the $\gamma n \rightarrow \pi^- p$ channel. Predictions from the SAID and MAID multipole analyses for the polarization observables of $\gamma n \rightarrow \pi^- p$ which can be measured in this experiment are shown in Figure 2 for a few sample energies. Σ is the linearly-polarized beam asymmetry and E and G are beam-target double-polarization asymmetries measured with circular and linear polarized photons, respectively.

Below 2π threshold, amplitude phases are constrained by πN scattering through unitarity (Watson's theorem). But at higher energies multipole analyses become increasingly model dependent. The SAID and MAID analyses use different schemes to extend amplitude unitarization and different approaches to extract resonance couplings. The SAID analysis fits

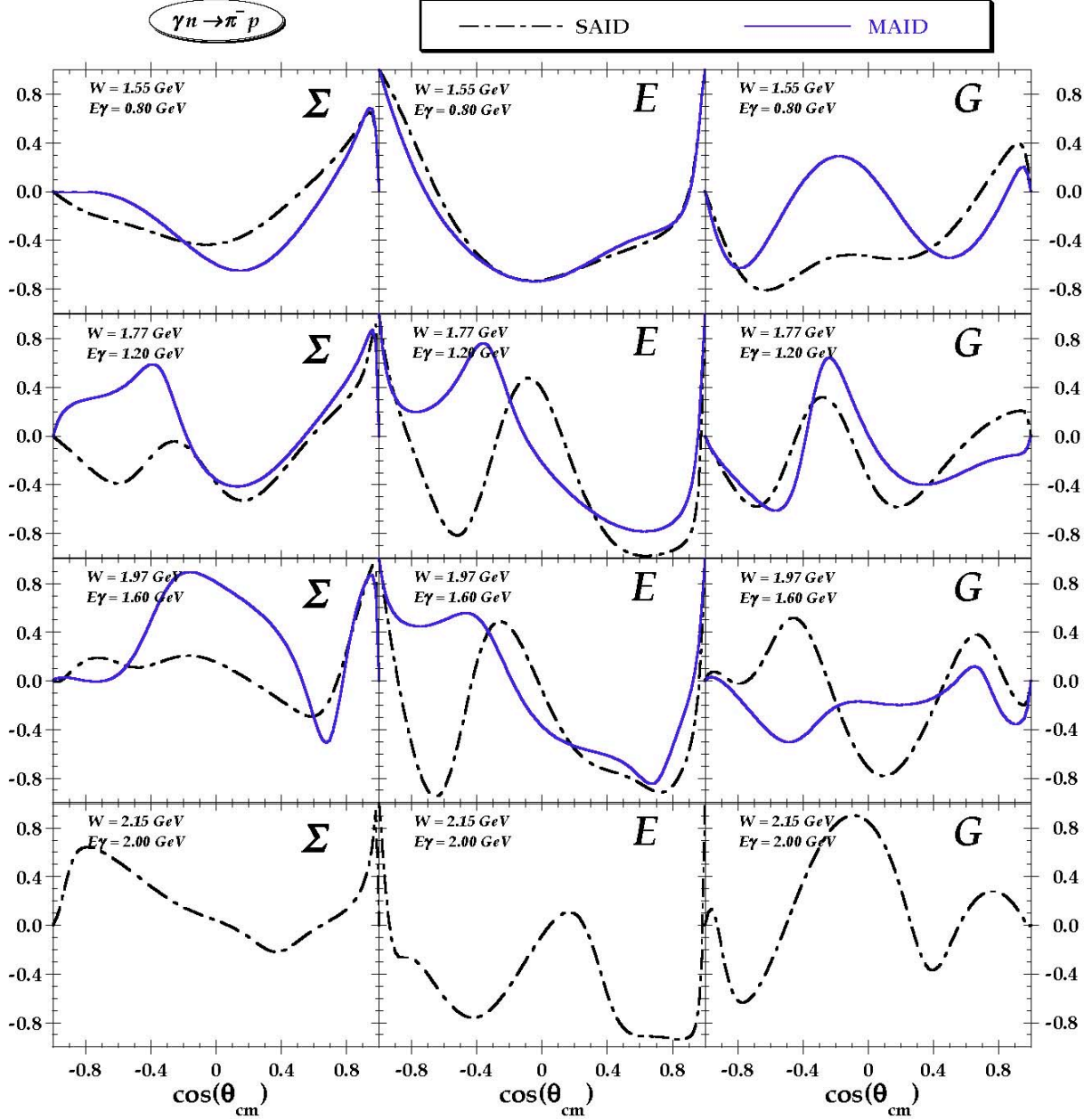


Figure 2. Polarization observables Σ (left), E (center) and G (right) for the $\gamma n \rightarrow \pi^- p$ channel as predicted by the SAID and MAID multipoles at the indicated four energies.

multipoles first and then parameterizes these in terms of Breit-Wigner resonance and background contributions. The MAID analysis varies resonance parameters directly when fitting data. The large variations evident in Figure 2, particularly at the higher energies, reflect the severe lack of experimental constraints. As a result, the uncertainties on the γn photo-couplings listed in the PDG compilation are considerably larger than the γp couplings for all of the N^* resonances (and are probably under-estimated); in some cases their values are consistent with zero.

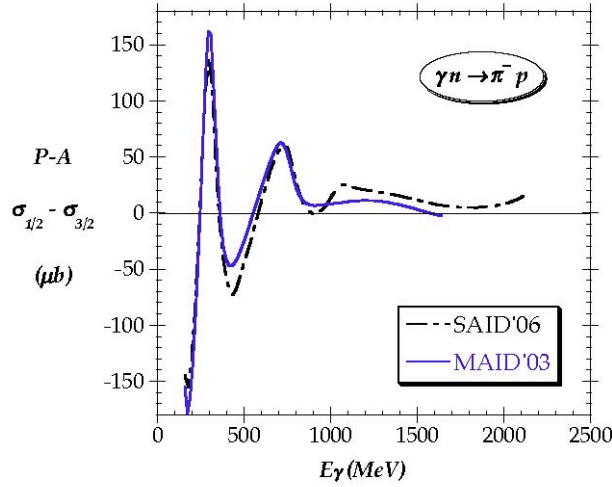


Figure 3. Helicity difference cross section for $\gamma n \rightarrow \pi^- p$ predicted by the SAID and MAID PWA.

The numerator of the E asymmetry is the difference of helicity dependent cross sections that can be measured with circularly polarized beams and longitudinally polarized targets, $\sigma^{1/2} - \sigma^{3/2}$. The integral of this observable over angle enters the GDH spin-sum rule. Predictions for this helicity difference cross section in the $\gamma n \rightarrow \pi^- p$ channel from the SAID and MAID multipole analyses are plotted in Figure 3. The two PWA are quite similar below 800 MeV but exhibit distinctly different trends at higher energies.

Both the SAID solution^[19] summed over all channels, as well as recent helicity-dependent total absorption data from Bonn^[20], also suggest a positive rise in the difference cross section from a neutron target at high energies. Considering the absence of such a trend in proton GDH data^[21] (Figure 4), this feature could reflect contributions from as yet unidentified resonances that couple strongly to γn but weakly to γp .

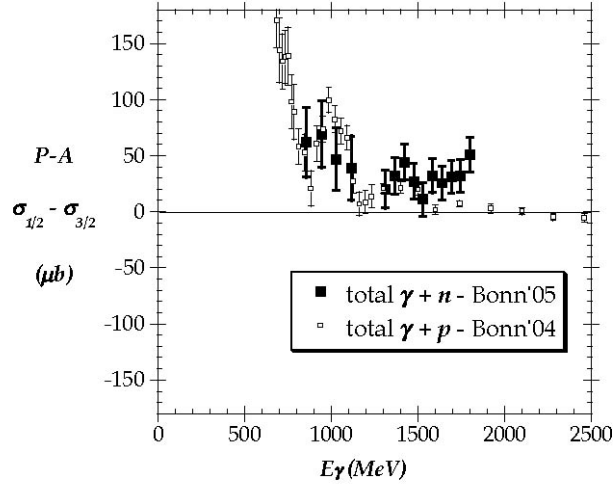


Figure 4. Total helicity difference for n and p targets as measured in Bonn [20,21].

Data on η and K production from the neutron are almost non-existent. The consequence of under-constrained amplitudes in the search for *missing* quark model states can be illustrated with the $\gamma n \rightarrow K^0 \Lambda$ reaction. Predictions for a sampling of polarization observables are plotted in Figure 5 at two energies, the higher one near the peak of the new D_{13} candidate. In addition to Σ , E and G , O_x and C_z are linear and circular beam - recoil asymmetries, with in-plane Λ polarization, and L_x is the longitudinally polarized target - in-plane Λ recoil asymmetry. The solid curves are calculated with Kaon-MAID [22], while the dashed curves are from a *Chiral Symmetry Inspired (CSI)* variant [9]. Red curves include the proposed $D_{13}(1950)$; the blue curves are generated by setting the couplings of this resonance to zero.

There is a strong overlap between the theoretical groups that developed the predictions of Figure 5 and the large variations simply reflect the lack of constraining data. In all likelihood, neither are correct.

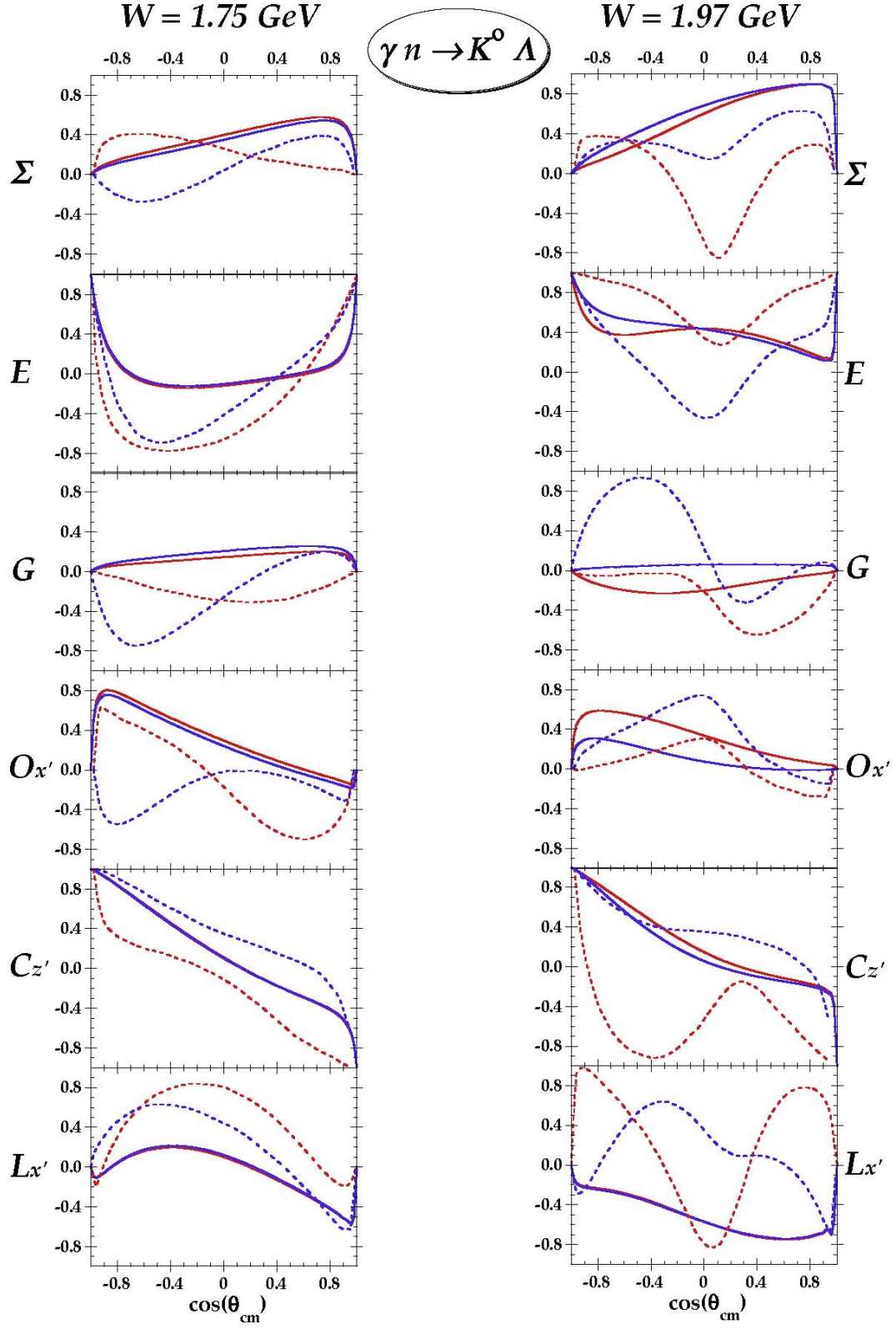


Figure 5. Polarization observables for $\gamma n \rightarrow K^0 \Lambda$ from Kaon-MAID [22] (solid curves) and from the CSI model [9] (dashed). Predictions are shown with (red) and without (blue) the proposed $D_{13}(1950)$.

In addition to excited baryon decays to single meson and nucleon final states, decays to intermediate excited baryons with subsequent emission of a second meson, $\gamma n \rightarrow \pi \Delta \rightarrow \pi^+ \pi^- n$ for example, have substantial cross sections. In fact, the $\pi^+ \pi^- n$ final state is sensitive to sequential decays of resonances and potentially *missing* states may have much stronger couplings to $\pi\pi N$ than πN ^[6]. Above 1.6 GeV, many nucleon resonances decay predominantly through either $\pi\Delta$ or ρN intermediate states into $\pi\pi N$ final states. Thus any attempts to understand the higher mass region completely, *e.g.* through PWA, without including the $\pi\pi N$ channel are inherently incomplete.

The amplitude for producing $\pi\pi N$ final states has a considerably larger number of parameters owing to the greater kinematic freedom in the reaction. The process is described by eight amplitudes^[23]. There are 64 possible polarization observables, of which 15 are independent. This experiment will measure several for the $\gamma n \rightarrow \pi^+ \pi^- n$ channel and these have the potential to address interesting questions.

The $F_{15}(1680)$ decays with a $\sim 10\%$ branch to $\pi\Delta$ in the midst of many overlapping (and interfering) resonances. The contribution of this branch to the $\pi\pi N$ amplitude is usually included with a negative phase ^[24], following analyses of Manley *et al.* However, Fix and Arenhövel have pointed out that a +ve sign for the $F_{15} \rightarrow \pi \Delta$ contribution is needed to reproduce recent $\pi^0 \pi^0 N$ data from GRAAL²⁵ and ELSA²⁶.

The P_z^S polarization asymmetry^[23] for $\gamma n \rightarrow \pi^+ \pi^- n$, measured with linearly polarized photons and a longitudinally polarized target (analogous to the G observable of πN), is plotted in Figure 6 as a function of some of the available kinematic variables: $\Theta_{\pi^-}^*$ (right-top panel) and $\Theta_{\pi^+}^*$ (right-middle) are the polar angles of one pion in the c.m. frame of that pion and the neutron; θ_{π^-} (left-top) is the polar angle of the pion relative to the beam axis; ϕ_{π^+} is the azimuthal angle of the pion in the c.m. frame of that pion and the nucleon; and the Invariant Mass (bottom two panels) is calculated for the indicated charged pion and the neutron. There is a strong sensitivity to the sign of the $F_{15} \rightarrow \pi \Delta$ term in all of the plots of Figure 6. This is just one example of many interesting issues that can be addressed with the new $\pi^+ \pi^- n$ polarization data of the proposed experiment.

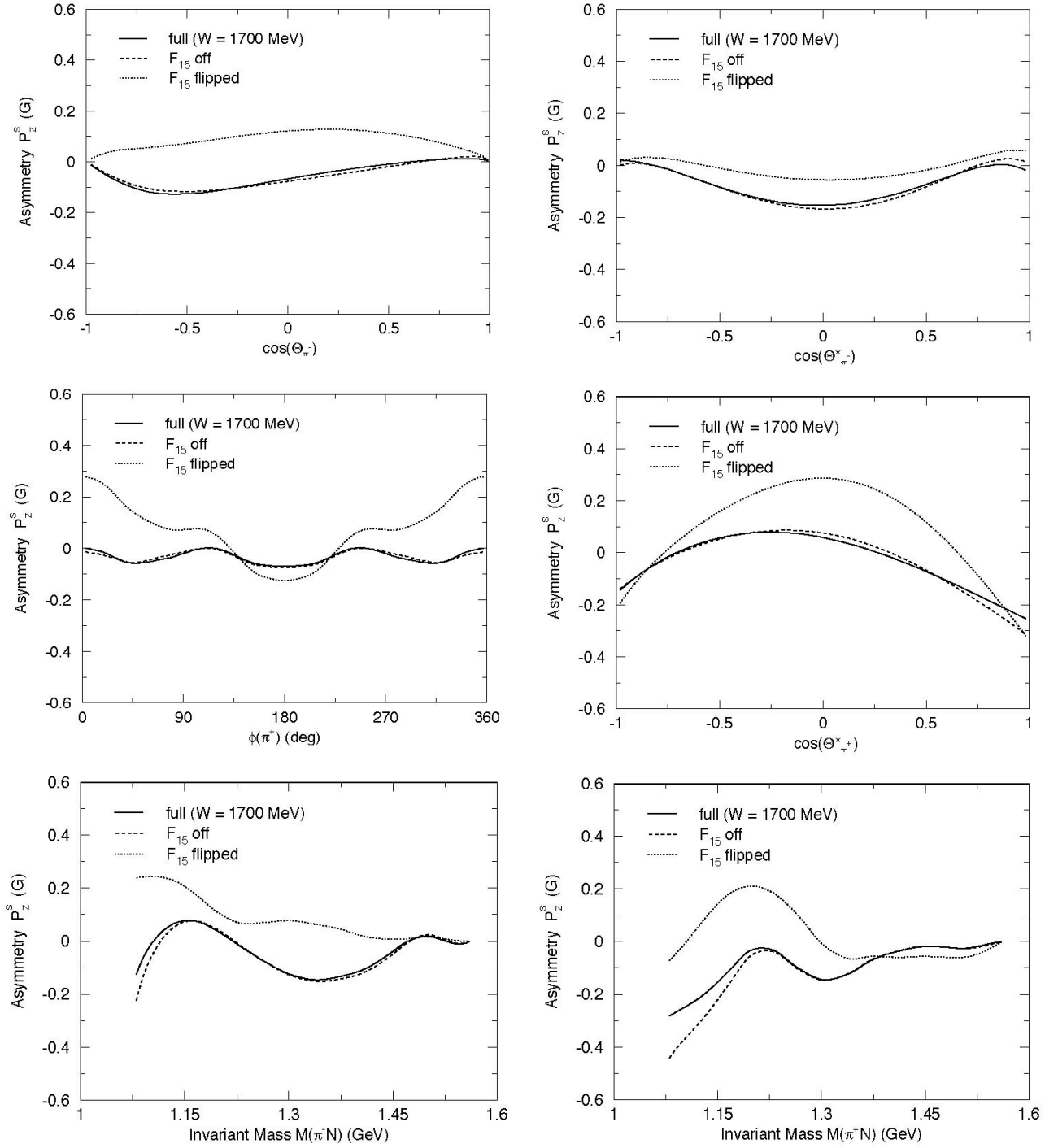


Figure 6. The P_z^S ("G") asymmetry in the $\gamma n \rightarrow \pi^+ \pi^- n$ reaction, plotted against some of the variables of the $\pi\pi N$ reaction. Calculations are from [24]. The *flipped* condition corresponds to a change in sign of the $F_{15} \rightarrow \pi \Delta$ contribution to the $\pi\pi N$ amplitude, as has recently been suggested.

The $D_{13}(1520)$ and the $F_{15}(1680)$ have strong decay branches to $\pi \Delta$ as well as πN . Any search for new resonances that might couple stronger to $\pi \Delta$ than to πN will require a multipole decomposition into partial waves. The $\pi\pi N$ polarization observables have considerable sensitivity to $\pi \Delta$ partial wave components, as illustrated using the $D_{13}(1520)$ as an example in Figure 7, where the P_z^0 (“E”) and P_z^S (“G”) beam-target polarization observables are plotted against $\Theta_{\pi^+}^*$ and $\Theta_{\pi^-}^*$. Measurements of these asymmetries will be instrumental in constraining partial wave analyses.

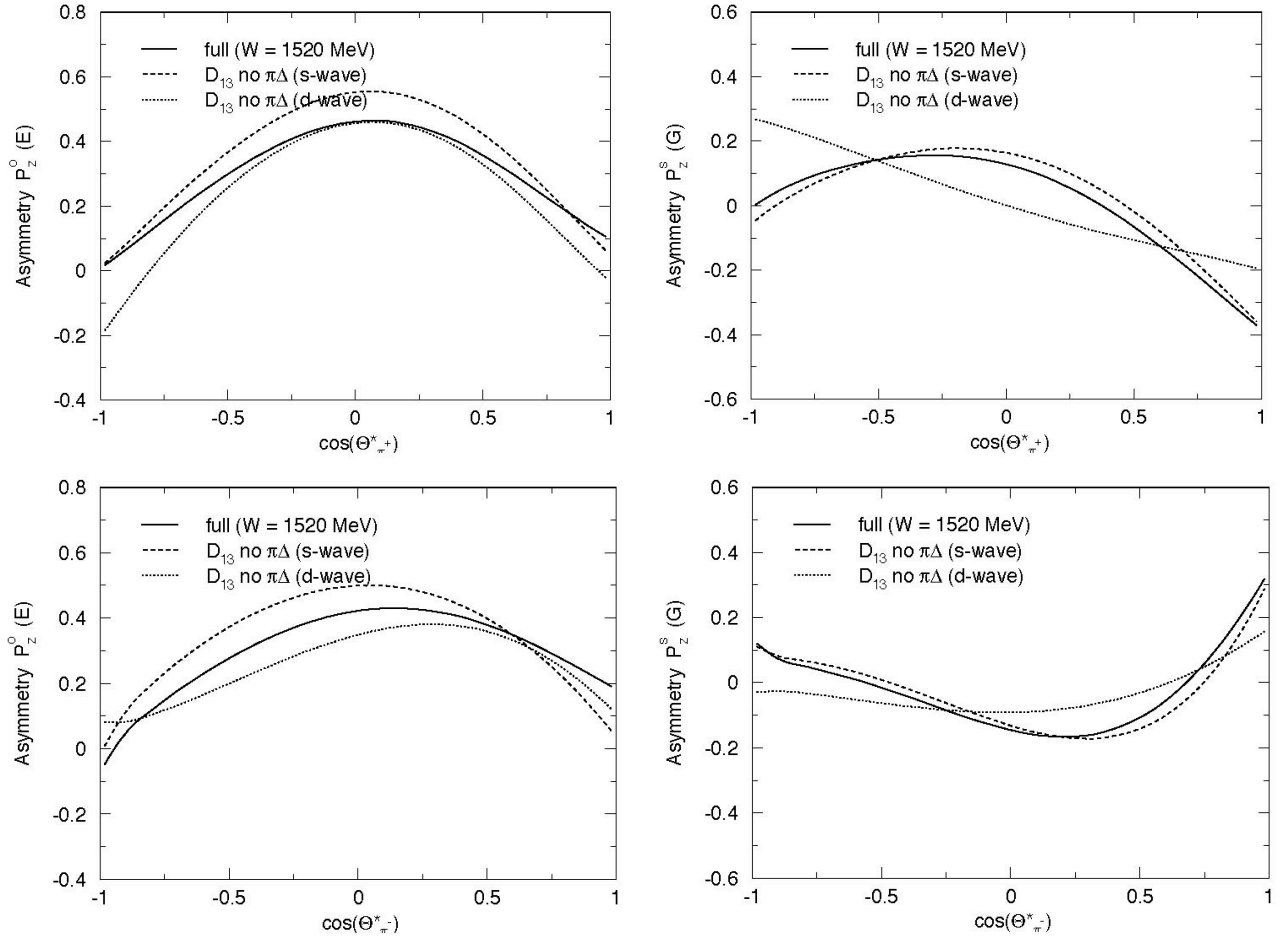


Figure 7. The P_z^0 (“E”) and P_z^S (“G”) beam-target polarization observables at $W = 1520$ MeV. The dashed and dotted curves result from eliminating the s and d-wave multipoles in $D_{13}(1520) \rightarrow \pi\Delta$ decay^[24].

1.1 Proposed Measurement of Polarization Observables

The two spin states of the photon and of the nucleon lead to four helicity amplitudes that determine single-pseudoscalar ($J^\pi = 0^-$) meson production from the neutron (and another four from the proton). Since these are complex, there are eight quantities to be determined for each target isospin by measuring different observables. The use of a common phase to reduce this number to seven leads to discrete ambiguities, so that eight distinct quantities are required and these must be carefully chosen ^[16]. In addition to the cross section (σ_0) as measured with unpolarized photons, there are three single-spin asymmetries accessed by polarizing the beam (Σ), the target (T), or the recoiling baryon (P), as well as three sets of double-polarization asymmetries corresponding to the beam-target (BT), target-recoil (TR) and beam-recoil (BR) combinations. The conventional particle physics nomenclature is given in Table 1. A *complete* data set that eliminates discrete ambiguities requires a minimum of eight observables: the cross section (σ_0), the single-spin asymmetries (Σ, T, P) and four double-polarization asymmetries, at

Table 1. Polarization observables in pseudoscalar meson photo-production. The entries in brackets denote observables that appear in other locations in the table.

Photon beam		Target			Recoil			Target + Recoil			
					x'	y'	z'	x'	x'	y'	z'
		x	y	z				x	z	x	z
unpolarized γ	σ_0		T			P		$T_{x'}$	$-L_{x'}$	$T_{z'}$	$L_{z'}$
linearly P_γ	Σ	H	$(-P)$	$-G$	$O_{x'}$	$(-T)$	$O_{z'}$	$(-L_{z'})$	$(T_{z'})$	$(-L_{x'})$	$(-T_{x'})$
circular P_γ		F		$-E$	$-C_{x'}$		$C_{z'}$				

least one involving recoil polarization. While this is a minimum, a larger number of different observables is highly desirable to mitigate the effects of systematic uncertainties in a PWA. For single-pseudoscalar meson production, triple-polarization data do not yield uniquely new matrix elements but nonetheless provide additional determinations of other observables.

Table 2. Pseudoscalar meson reactions and observables that will be measured in the proposed experiment.

<i>reaction</i>	<i>observable</i>
$\gamma + n(p) \rightarrow \pi^- p(p)$	σ_0, Σ, E, G
$\gamma + n(p) \rightarrow \pi^+ \pi^- n(p)$	$\sigma_0, I^c(\Sigma), I^s, I^p, P_z,$ $P_z^o(E), P_z^s(G), P_z^c$
$\gamma + n(p) \rightarrow K^0 \Lambda(p)$	σ_0, Σ, E, G $O_{x'}, O_{z'}, C_{x'}, C_{z'}, P, T=(-O_{y'})$ $L_{x'}, L_{z'}, T_{x'}, T_{z'}$
$\gamma + n(p) \rightarrow K^0 \Sigma^0(p)$	$\sigma_0, \Sigma, P, E, G$
$\gamma + n(p) \rightarrow K^+ \Sigma^-(p)$	σ_0, Σ, E, G

The proposed experiment will focus on reactions with tagged circularly- and linearly- polarized photons and a longitudinally polarized deuterium target. The pseudoscalar meson channels that will be studied are listed in Table 2. In the case of kaon production, the angular distributions in the weak hyperon decays will be used to determine recoil polarization.

The use of polarized beams, polarized target and analysis of recoil hyperon polarization provides a unique opportunity to perform **a complete experiment for the $\gamma + n \rightarrow K^0 \Lambda$ channel for which the amplitude in fact can be over-determined** by the large suite of observables. Circular polarized beams will be used to measure the E beam-target asymmetry and the $C_{x'}$ and $C_{z'}$ beam-recoil asymmetries (in-plane recoil components); linearly polarized photon beams will be used to measure the single-spin beam asymmetry, Σ , the G beam-target asymmetry, the $O_{x'}$ and $O_{z'}$ beam-recoil (in-plane component) asymmetries and the single-spin target asymmetry, T , as a beam-recoil observable; combining all beam polarization states will provide measurements of the Λ recoil single-spin asymmetry, P , and the target-recoil observables $L_{x'}$ and $L_{z'}$ (in-plane components). Finally, triple beam-target-recoil measurements with linearly polarized photons will access the transverse-Target-Recoil asymmetries $T_{x'}$ and $T_{z'}$.

When the proposed data are combined with similar experiments on the proton (*eg.* the H-Butanol experiment E02-112 which will measure B-T and T-R asymmetries for KY channels, together with data from the CLAS-*g1* and *-g8* run groups which will provide $\gamma+p$ B-R asymmetries), the two will yield a complete determination of the $A_{\mathbf{K}\Lambda}^{(0)}$ and $A_{\mathbf{K}\Lambda}^{(1)}$ isospin $\frac{1}{2}$ amplitudes (eqn. 1). This will be the first opportunity to confront models of pseudoscalar meson production from the nucleon with the maximal experimental constraint. (In principle, this would also be possible for the $K^0 \Sigma^0$ and $K^+ \Sigma^-$ channels, however the significantly smaller analyzing power in the Σ decays leads to impractical running time requirements.)

The observables of Table 2 can be extracted from an analysis of decay angular distributions. When the beam and target are polarized, the cross section for single-pseudoscalar meson production takes the form,

$$\frac{d\sigma}{d\Omega}(\theta, \phi; E_\gamma) = \frac{d\sigma_o}{d\Omega}(\theta; E_\gamma) \cdot \left\{ \begin{aligned} &1 + P_\gamma^L \cdot \left[\Sigma(\theta; E_\gamma) + \frac{1}{\sqrt{2}} P_D^T \cdot T_{20}^L(\theta; E_\gamma) \right] \cdot \cos 2\phi \\ &+ P_\gamma^L \cdot P_D^V \cdot G(\theta; E_\gamma) \cdot \sin 2\phi \\ &- P_\gamma^C \cdot P_D^V \cdot E(\theta; E_\gamma) + \frac{1}{\sqrt{2}} P_D^T \cdot T_{20}^0(\theta; E_\gamma) \end{aligned} \right\}. \quad (2.1)$$

Here, P_D^V is the vector polarization of the deuteron along the beam axis, P_D^T is the deuteron tensor polarization, P_γ^C and P_γ^L are the circular and linear photon polarizations, respectively, and ϕ is the angle between the linear photon polarization and the reaction plane. Two additional Tensor asymmetries appear here, although calculations suggest that their contribution is quite small except at very forward angles.

With polarized beams and an analysis of recoil hyperon polarization, the cross sections are given by,

$$\frac{d\sigma}{d\Omega}(\theta, \phi; E_\gamma) = \frac{d\sigma_o}{d\Omega}(\theta; E_\gamma) \cdot \left\{ \begin{aligned} &1 + P_\gamma^L \cdot \left[\Sigma(\theta; E_\gamma) - P_r^y \cdot T(\theta; E_\gamma) \right] \cdot \cos 2\phi \\ &- P_\gamma^L \cdot \left[P_r^x \cdot O_{x'}(\theta; E_\gamma) + P_r^z \cdot O_{z'}(\theta; E_\gamma) \right] \cdot \sin 2\phi \\ &- P_\gamma^C \cdot \left[P_r^x \cdot C_{x'}(\theta; E_\gamma) + P_r^z \cdot C_{z'}(\theta; E_\gamma) \right] \\ &+ P_r^y \cdot P(\theta; E_\gamma) \end{aligned} \right\}. \quad (2.2)$$

Similarly, the dependence on target and recoil polarization is given by,

$$\frac{d\sigma}{d\Omega}(\theta, \phi; E_\gamma) = \frac{d\sigma_o}{d\Omega}(\theta; E_\gamma) \cdot \left\{ \begin{aligned} &1 - P_D^V \cdot [P_r^x \cdot L_{x'}(\theta; E_\gamma) - P_r^z \cdot L_{z'}(\theta; E_\gamma)] \\ &+ P_r^y \cdot P(\theta; E_\gamma) \\ &+ P_\gamma^L \cdot P_D^V \cdot [P_r^x \cdot T_{z'}(\theta; E_\gamma) - P_r^z \cdot T_{x'}(\theta; E_\gamma)] \cdot \sin(2\phi) \end{aligned} \right\} . \quad (2.3)$$

The $T_{x'}$ and $T_{z'}$ terms in eqn (2.3) are Transverse-Target-Recoil asymmetries which can be measured as a Beam-Target-Recoil triple polarization asymmetry using a longitudinally polarized target. The coefficients of each of the terms in eqn (2.1-2.3) can be varied to deduce all of the observables.

The amplitudes for double-pion photo-production are more complex. Their determination requires single-, double- and even triple-polarization observables because a much larger number of kinematic variables is needed to define the reaction^[23]. With polarized beams and longitudinal target polarization, the cross section takes the form,

$$\frac{d\sigma}{d\Omega} = \frac{d\sigma_o}{d\Omega} \cdot \left\{ \begin{aligned} &1 + P_\gamma^L \cdot [I^c + P_D^V \cdot P_z^c] \cdot \cos 2\beta \\ &+ P_\gamma^L \cdot [I^s + P_D^V \cdot P_z^s] \cdot \sin 2\beta \\ &+ P_\gamma^C \cdot [I^o + P_D^V \cdot P_z^o] + P_D^V \cdot P_z \end{aligned} \right\} .$$

Here, we use the nomenclature of ref. [23] and have dropped the explicit dependence on reaction angles, since there are too many of them. The angle between the electric vector of a linearly polarized photon and the plane defined by the beam direction and the nucleon recoil is β . The I^c observable is the analog of the beam asymmetry, Σ , in eqn (2.1). The P_z^s and P_z^o asymmetries are the 2π analogs of the G and E observables of eqn (2.1). These are shown in the calculations of Figure 6 and Figure 7. In $\pi\pi N$ there is even a non-vanishing circularly polarized beam asymmetry (I^o) whenever the two pions and the recoil nucleon are not in the same plane. In all, seven $\pi\pi N$ polarization observables will be determined from the proposed experiment. While the combination of these measurements on the neutron and the corresponding proton experiment

(E06-013) will still fall short of determining 2π production, they do have the potential of providing significant new constraints and may reveal new states that couple strongly to $\pi\pi N$.

The proposed experiment will tag circularly polarized photons, produced by the bremsstrahlung of longitudinally polarized electrons, as well as linearly polarized photons from coherent bremsstrahlung in diamond crystals. A frozen-spin deuterium target is required and there are two possible choices: a deuterated version of the FROST Butanol target which is under development at JLab and a polarized HD target which has been developed at Brookhaven. Details of the FROST target have been reported at several PAC meetings and should be familiar to the reader. The HD target is new to the JLab community. Its characteristics are summarized in the Appendix to this proposal. We have carried out detailed simulations of this experiment for both targets and conclude that a substantial reduction in running time is possible with the use of polarized HD. These comparisons are summarized in the Section 2, *Monte Carlo Simulations*.

We anticipate running with an HD target having $P_V(D) = 40\%$. A vector polarization of 40% implies an accompanying tensor polarization, $P_T(D)$, of about 12% (see Appendix A). Although T.-S.H. Lee and B. Juliá-Díaz of this collaboration have begun preparations to model $D(\gamma, K)Y$ reactions, at present no predictions are available. However, calculations are available for the $D(\gamma, \pi)NN$ channel^[27]. There, the tensor observables T_{20}^L and T_{20}^0 of eqn (2.1) become appreciable only at very forward angles, $\cos(\theta_{cm}) > 0.9$, and are found to be less than about 0.05 throughout the angular range of this experiment. The factor of 4 smaller tensor polarization, compared to vector, makes these contribution essentially unobservable. Nonetheless, we will have two cross-checks on possible small contaminations of the nucleon target asymmetries (either BT or TR) by deuteron tensor observables, which we illustrate with eqn (2.1).

- Rotating the deuteron spin direction flips the vector polarization ($N_+ - N_-$) but leaves the tensor polarization ($N_+ + N_- - 2N_0$) unchanged. This comparison allows a direct extraction of the T_{20}^0 observable of eqn (2.1).

- In addition, as discussed below, approximately 13% of the run time request will utilize an $\vec{H}D$ target with high H polarization but no vector D and, hence, no tensor D polarization. The comparison of asymmetries from runs with two different values of $P_T(D)$ separates the T_{20}^L of eqn (2.1) from the beam asymmetry, Σ .

1.2 Extraction of *neutron* amplitudes

We next discuss the general problem of extracting neutron information from deuteron reactions. In the extraction of *neutron* amplitudes from deuterium reactions, complementary empirical and theoretical approaches will be pursued.

1.2.1 Empirical Analysis: We focus on identifying reactions which can be completely determined, for example,

$$\gamma + D \equiv \gamma + n + (p) \rightarrow K^0 + \Lambda + (p) \rightarrow \pi^+ \pi^- + \pi^- p + (p) .$$

The detection of three charged pions and a proton in the CLAS determines the momentum of the unobserved proton. Two kinematic restrictions can be used to select reactions for which the undetected proton was essentially a *spectator*.

(a) Co-planarity: In the absence of the proton in deuterium, the $\gamma + n \rightarrow \text{meson} + \text{Baryon}$ reaction would be 2-body and confined to a plane, so that the azimuthal angle (ϕ) between the baryon and the $\langle \gamma\text{--meson} \rangle$ plane would be 180° . A target proton participating in the reaction will kick the baryon out of this plane and shift this angle away from 180° . Typically, we require that ϕ be within $\pm 30^\circ$ of the coplanar condition.

(b) Spectator momentum: A requirement that the deduced momentum of the unobserved proton be small emphasizes *quasi-free* neutron reactions. However, the detected kinematics for the final state particles ($p\pi^+2\pi^-$ in the above example) might be distorted by final-state interactions, thus not coming from the elementary reactions on the neutron. The thresholds for such effects can be estimated using the model by J.-M. Laget ^[28] on hyperon photoproduction from the deuteron which describes quasifree kaon production as well as kaon and hyperon rescattering. Applied to $\gamma d \rightarrow pK^0\Lambda$ and $\gamma d \rightarrow pK^+\Sigma^-$ the dominant graphs are shown in Figure 8, with k being the outgoing kaon momentum and p_1, p_2 the outgoing baryon momenta. In graph (I)

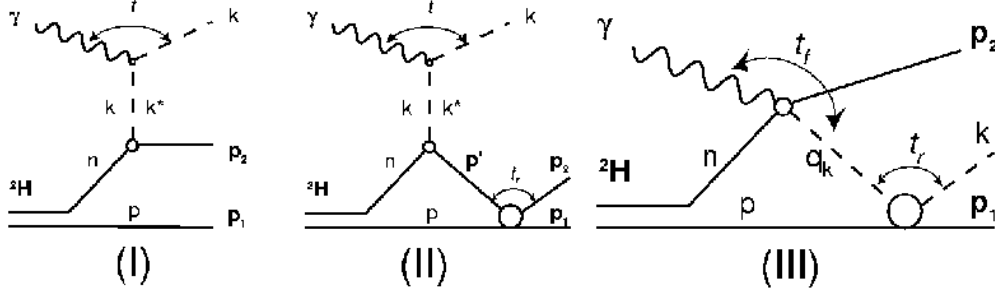


Figure 8. Dominant graphs in KY production on the neutron according to Laget's model^[28] : proton as spectator particle (I), hyperon rescattering (II), kaon rescattering (III).

the production of KY on the neutron is mediated via t -channel exchange of K or K^* . The rescattering contributions, depicted in graph (II) for the hyperon–nucleon and in graph (III) for the kaon–nucleon rescattering vertex, dominate at high proton momenta. The contributions for both rescattering processes are maximal for on-shell propagators in the loop, *i.e.* when the spectator momentum in the loop vanishes; or in other words, when both nucleons in the deuteron are at rest and the hyperon or kaon is produced on one nucleon and rescatters off the other nucleon, which then obtains its recoil momentum \mathbf{p}_1 . In this model, the rescattering amplitudes only depend on low-momentum components of the deuteron wave function and on-shell matrix elements, and thus can be calculated readily. Laget has shown that the contributions of graphs (II) and (III) are quite small for small spectator momenta \mathbf{p}_1 , with $p_1 \leq 0.2$ GeV; there, quasifree production -- with the proton as a spectator -- dominates.

Quasifree production is directly related to the elementary reaction when corrected for the momentum distribution $\rho(\mathbf{p}_1)$ of the spectator and the moving target nucleon:

$$\frac{d^5\sigma}{d\mathbf{p}_1 d\Omega_{p_1} d\Omega_k} = \left(1 + \frac{p_1}{E_1} \cos\theta_{p_1}\right) \rho(\mathbf{p}_1) \frac{d^2\sigma}{d\Omega_k}(\gamma n \rightarrow KY) \quad . \quad (3)$$

In the simulations described in the following sections, we have investigated the use of both coplanarity requirements and low missing proton momentum cuts. The two are largely complementary. We prefer coplanarity cuts since angles can be measured quite accurately. The construction of a small missing momentum usually involved the subtraction of much larger numbers. The associated uncertainties in defining such cuts increase the difficulty of correcting

for their efficiency. However, while deduced “ $\gamma + n$ ” cross sections will be dependent upon the efficiency of such kinematic cuts, asymmetry ratios will be much less sensitive to the choice of ϕ or p_s .

Since a vector-polarized deuteron contains a polarized bound proton, beam-target and target-recoil asymmetries can also be measured simultaneously for the corresponding proton reactions. For example, the proton reaction conjugate to the above neutron reaction is,

$$\gamma + D \equiv \gamma + p + (n) \rightarrow K^+ + \Lambda + (n) \rightarrow K^+ + \pi^- p + (n) ,$$

and asymmetries measured with the same kinematic cuts used in the extraction of “ $\gamma + n$ ” observables can be compared with results from photo-production on polarized hydrogen.

Although the discussion here has used the $K\Lambda$ channel as an example, these empirical methods apply to all of the pseudoscalar meson channels of Table 2.

1.2.2 Theoretical analysis: In addition to kinematical restrictions aimed at emphasizing *quasi-free* neutrons, a complementary theoretical approach is also under development as a joint project with T.-S. H. Lee, T. Sato and A. Matsuyama, together with S. Hoblit and A. Sandorfi. The basic calculation can be illustrated in terms of π -production from deuterium, although it will be applicable to the full range of pseudoscalar mesons. The calculation will proceed in stages through the full spectrum of nucleon resonances. We sketch here the first stage, starting with the $P_{33} \Delta(1232)$ which is presently under study.

The $D(\gamma, \pi NN)$ reactions are determined by the initial nucleon pion photo-production process and the final πNN interactions. A Hamiltonian model developed by Lee and Matsuyama, which successfully describes $NN \rightarrow \pi NN$ reactions up to $E_{\text{lab}} = 1 \text{ GeV}$ ^[29 - 30], will be applied for πNN interactions. This will be combined with the well-tested Sato-Lee model for pion photoproduction from the nucleon ^[31]. The amplitude for $D(\gamma, \pi NN)$ can be written as,

$$T(E) = \mathbf{T}^{\text{scat}}(E) + \mathbf{T}^{\text{int}}(E) , \quad \text{where} \quad \mathbf{T}^{\text{scat}} = \langle \Psi_{\pi NN}^{(-)} | [\mathbf{t}_{\pi N, \gamma p} + \mathbf{t}_{\pi N, \gamma n}] | \Phi_d \rangle .$$

The Sato-Lee model is used for the $t_{\pi N, \gamma p}$ and $t_{\pi N, \gamma n}$ amplitudes. The leading contributions to T^{scat} are impulse (for Fermi motion), NN interaction and pion rescattering, as illustrated in the figure below. In a complete calculation, higher order multiple-scattering effects will be included

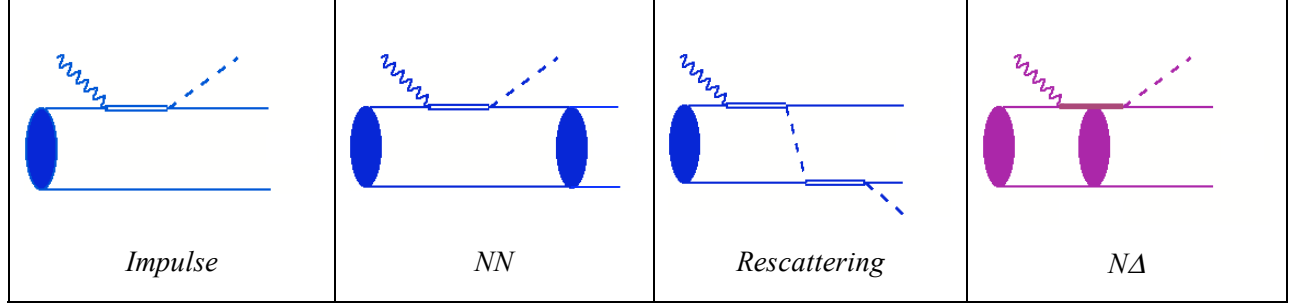


Figure 9. The major components in a calculation of $\gamma D \rightarrow \pi NN$.

by generating the full scattering wave function $\Psi_{\pi NN}^{(-)}$ from solutions of the Faddeev equations for the πNN system. Ongoing work on this project has shown that such higher order effects are weak in the Δ region and can be neglected. These will be included as needed when dealing with higher energy regions of N^* production.

The $T^{int}(E)$ term contains the $N\Delta$ interactions. These are calculated by solving the coupled-channel equations,

$$X_{\alpha, \beta}(E) = [V + Z(E)]_{\alpha, \beta} + \sum_{\gamma} [V + Z(E)]_{\alpha, \gamma} G_{\gamma}(E) X_{\gamma, \beta}(E) ,$$

where the indices $\alpha, \beta, \gamma = NN, N\Delta$ and $G_{\gamma}(E)$ is the propagator including a dynamically generated Δ width. V is the meson-exchange interaction potential describing all possible transitions between NN and $N\Delta$ states, and $Z(E)$ is the one-particle exchange term which contains πNN unitarity cuts. The *interaction* amplitude is then calculate with $X_{\alpha, \beta}(E)$ as,

$$T^{int}(E) = \langle \pi NN | \sum_{B, B' = N, \Delta} [h_{\pi N, B} G_{NB}(E) X_{NB, NB'} G_{NB'}(E) g_{B, \gamma N}] | \Phi_d \rangle ,$$

where $\mathbf{h}_{\pi N, B}$ and $\mathbf{g}_{B, \gamma N}$ describe the $B \rightarrow \pi N$ and γN transitions with $B = N, \Delta$.

The parameters needed in the evaluation of these equations have been determined from extensive studies of πN and NN scattering and from $\gamma p \rightarrow \pi N$ reactions. The current effort is aimed at identifying observables and kinematic regions in which the effects due to T^{int} are weak so that the theoretical predictions are most sensitive to the elementary amplitudes $\mathbf{t}_{\pi N, \gamma p}$ and $\mathbf{t}_{\pi N, \gamma n}$ of T^{scat} . The proton amplitude, $\mathbf{t}_{\pi N, \gamma p}$, will first be fixed to the Sato-Lee model values and then the neutron amplitudes, $\mathbf{t}_{\pi N, \gamma n}$, will be varied to fit kinematically complete $D(\gamma, \pi^- p)p$ and $D(\gamma, \pi^0 n)p$ data on cross sections and polarization observables. The proton amplitudes will then be varied to overcome possible deficiencies in the Sato-Lee model. Once the elementary amplitudes are fixed in this way, the analysis will be repeated for the observables and kinematic regions for which T^{int} is important to ensure self-consistency.

Lee, Sato and Matsuyama have been working on this project for periods spanning two years, concentrating first on the delta region. This initial work has been carried out in collaboration with S. Hoblit and A. Sandorfi who are restructuring their code for the theoretical calculation so that (a) it can be used in Monte Carlo simulations of detector acceptances and (b) it can be efficiently run as part of a fitting procedure in which the parameters determining the Sato-Lee nucleon multipoles are adjusted to bring the Deuteron predictions as close as possible (with minimum chi-squared) to a set of cross sections and polarization observables. In this way, the input *free-neutron* multipoles can be determined and, more importantly, the underlying coupling constants and off-shell form factors that are the quantities of physical interest.

In the past few years, the Sato-Lee model has been extended to the higher mass N^* region. A dynamical coupled-channel model^[32] for πN , ηN , ωN , $\pi\pi N$, and KY production has been developed. This model is currently the core element of several projects of the newly formed *Excited Baryon Analysis Center (EBAC)* at JLab (with Lee serving as the Lead Investigator).

The $\gamma N \rightarrow K\Lambda$ and $K\Sigma$ channels are currently under intense study at EBAC. The first step has been the development of a dynamical coupled-channel calculation that describes the γN , πN and $K\Lambda$ channels and their interactions^[15, 33]. The calculation assumes a chiral constituent quark model^[34] to describe all known resonances with a minimum number of adjustable parameters, thereby enabling a search for new resonances within the dynamical model with far fewer

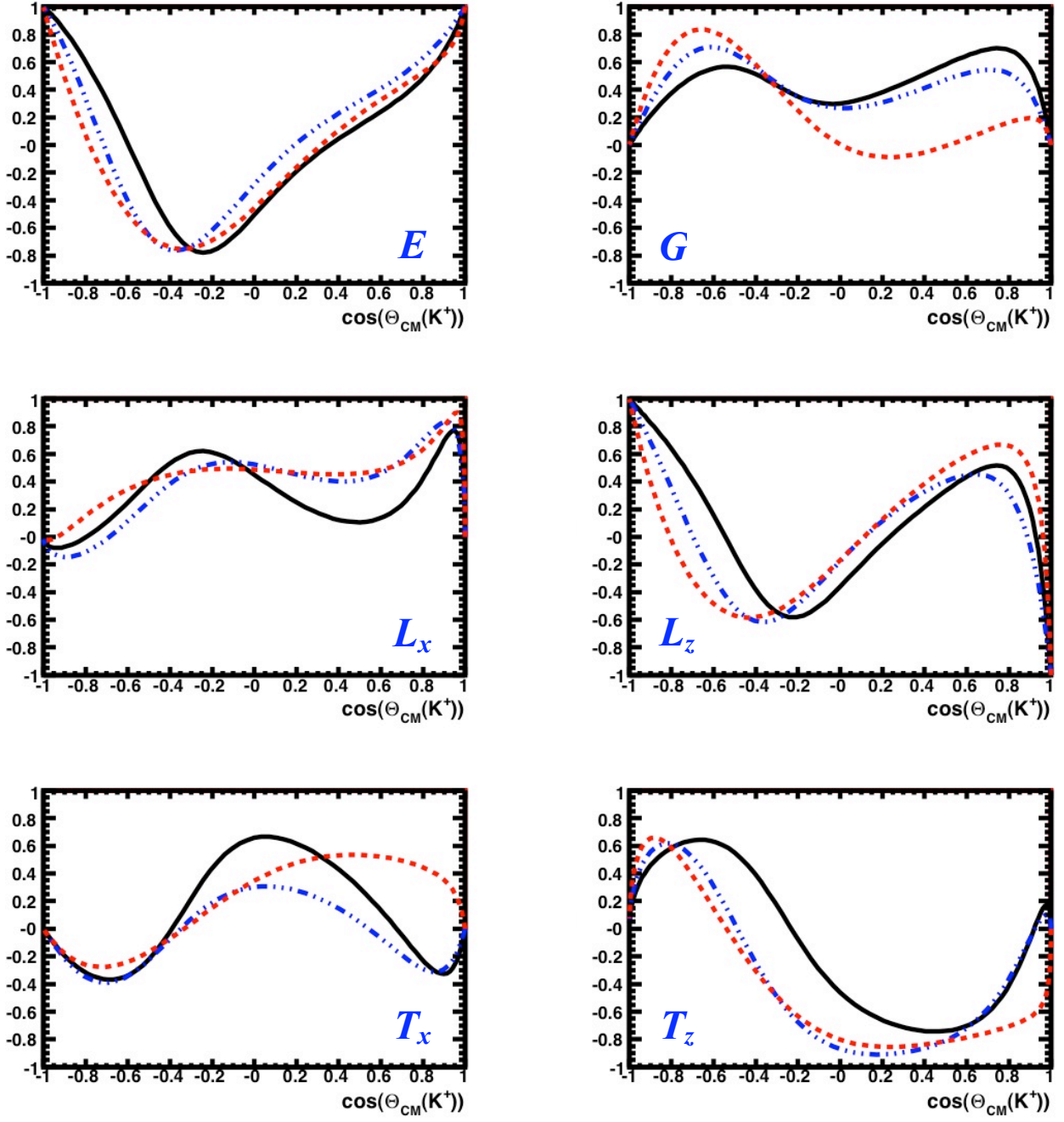


Figure 10. Predictions for the Beam-Target (E , G) and Target-Recoil (L_x , L_z , T_x , T_z) asymmetries in the $\gamma p \rightarrow K^+ \Lambda$ reaction at $E_\gamma = 1.55$ GeV ($W = 1.95$ GeV), which will be measured in this experiment. The solid black curves are the $M2$ solution from the calculation in ref. [15]; blue dot-dashed curves show the effect of turning off the channel coupling to πN ; red dashed curves result from turning off the effects of the pion cloud.

parameters than isobar models. First results on the $\gamma p \rightarrow K^+ \Lambda$ reaction have been published ^[15], with model parameters adjusted in a fit to the recent ELSA ^[7], CLAS ^[17, 35] and LEPS^[18] data. Predictions for the Beam-Target (E , G) and Target-Recoil (L_x , L_z , T_x , T_z) asymmetries at one of the beam energies which will be measured in this experiment are shown in Figure 10. The importance of multi-step $\gamma N \rightarrow \pi N \rightarrow KY$ processes is illustrated by the blue dot-dashed curves which show the effects of turning off the channel coupling and reverting to *tree-level* processes. Meson *cloud* effects, where baryon resonances are excited by a pion that is photo-produced via non-resonant mechanisms, also play an important role. Turning off such *cloud* terms results in the red dashed curves in Figure 10. Fitting such a model to a full suit of polarization observables will clearly access the underlying physics defining the dynamical structure of the nucleon.

The extension of this γN - πN -KY dynamical model to neutron targets is now under development. By 2008, the parameters for describing the production on the proton target are expected to be well determined from analysis of approved CLAS experiments. We thus expect that the model can be used to determine the amplitudes on the neutron by analyzing the data from the proposed experiment with a polarized deuteron target. The initial and final state interactions can be handled by using the same method sketched above, with appropriate extensions of the πNN calculations to include additional channels.

This is a complex, joint theoretical and experimental effort. As large a number of observables as possible is key to the convergence of the *free-neutron* amplitudes that form the input to these model calculations. While high accuracy data is always valuable, a survey of a large number of polarization observables is preferable to high accuracy on a more limited set.

The use of these calculations in detector simulations will allow direct comparisons with results from the empirically motivated *co-planarity* restrictions. They will also provide predictions for bound protons in deuterium and the *bound-p/free-p* ratio of asymmetries, which can be compared with values obtained from empirical cuts.

1.3 Polarized proton data runs

While most of the requested beam time will use an $\mathbf{H} \cdot \vec{\mathbf{D}}$ target with $P_D^V \sim 40\%$, 13% of the time is reserved for running with an $\vec{\mathbf{H}} \cdot \mathbf{D}$ target with $P_H \sim 75\%$ but no deuteron polarization.

The combination of the higher H polarization and a much larger CLAS acceptance from having to detect fewer particles in the final state allows for measurements on hydrogen in a very modest running time. The H and D nuclei are in a stoichiometric ratio of 1:1 in HD and a direct comparison of the observables from polarized H and polarized D with common systematic uncertainties will address three important questions:

- The availability of proton asymmetries, such as for the $\gamma p \rightarrow K^+ \Lambda$ and $K^+ \Sigma^0$ reactions, from free polarized protons in \vec{H} and from bound polarized protons in \vec{D} will allow a direct evaluation of the effectiveness of empirical coplanarity and missing-spectator momentum cuts. These same cuts, applied to the model under development at the EBAC will provide an important additional test of the new model when compared to *bound-p/free-p* data.

- The availability of a second data set with a different tensor polarization, $P_D^T=0$ for these polarized H runs, permits an evaluation of the deuteron tensor observables and corrections to the neutron asymmetries for these components, if needed.

- In a PWA, the relative normalization of polarization data must be varied by amounts consistent with the associated systematic errors of the data set. The presence of different systematic uncertainties associated with each observable can easily dilute their impact. The proposed $\vec{H} \cdot \vec{D}$ running will provide a parallel set of B - T (E , G) and, for KY channels, T - R observables (L_x , L_z , T_x , T_z) on the free proton ³, which are all locked together with systematic uncertainties that will be largely in common with the neutron asymmetries from the $H \cdot \vec{D}$ runs. When augmented by B - R data from the CLAS gI and $g8$ run groups, this will provide the tightest possible determination of the total isospin amplitudes, $A_{K\Lambda}$, of eqn (1).

While B - T and B - R asymmetries for $\gamma+p$ reactions will soon be available from FROST experiments, common systematics are crucial and these three important constraints cannot be investigated effectively without the additional $\vec{H} \cdot \vec{D}$ measurements. Fortunately, the time required for them is very modest.

³ The S , P and B - R observables will not be extracted from these polarized-H runs because of the difficulty in subtracting the contributions from bound protons in deuterium.

2 Monte Carlo Simulations

We have simulated the experiment for each of the channels in Table 2. The $\gamma N \rightarrow KY$ reactions determine the running plan, since their cross sections are small and their reconstruction requires the detection of multiple charge particles, 4 for $K^0\Lambda$ or $K^0\Sigma$ and 3 for $K^+\Sigma^-$, so that their acceptance is the smallest. Accordingly, we begin by discussing their simulation.

The experiment requires linearly and circularly polarized and tagged photon beams, which are readily available in Hall-B, and accurate reconstruction of hyperon decay angular distributions, for which the CLAS is well suited. The experiment also requires a polarized target and we have carried out detailed simulations for two candidates, an HD target which has been developed at BNL (see Appendix A) and a deuterated-butanol version of the FROST target now under construction at JLab. The results of these simulations are discussed below.

2.1 Studies of KY Channels

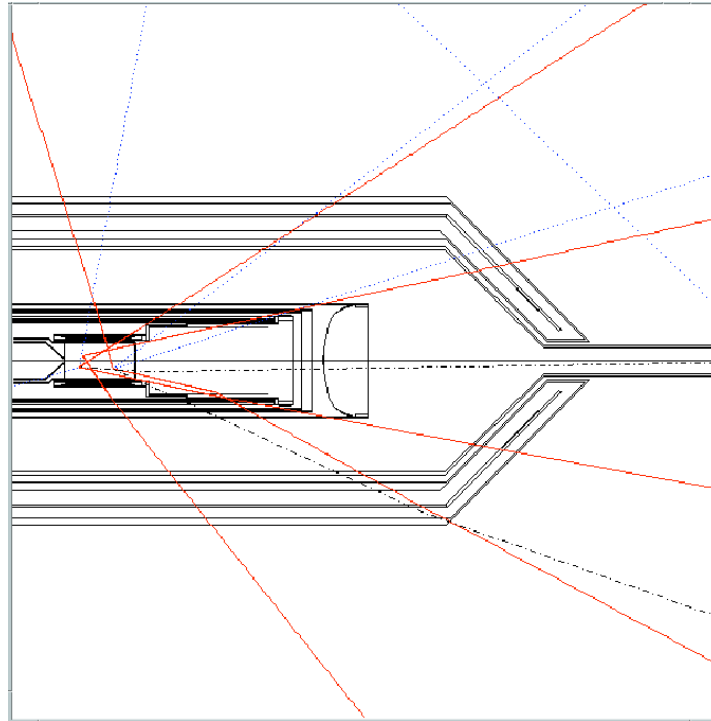


Figure 11. Sample Monte Carlo event produced in the HD target and propagated through the CLAS detector. Here an incident photon generates an electromagnetic shower in the target volume. Charged particle tracks are shown in red.

The following three hyperon production processes are considered,

$$\gamma n(p_s) \rightarrow K^0 \Lambda(p_s), \quad \gamma n(p_s) \rightarrow K^0 \Sigma^0(p_s), \quad \gamma n(p_s) \rightarrow K^+ \Sigma^-(p_s),$$

identified via the decays $K_s^0 \rightarrow \pi^+ \pi^-$, $\Lambda \rightarrow p \pi^-$, $\Sigma^0 \rightarrow \Lambda \gamma$, $\Sigma^- \rightarrow n \pi^-$. All particles except the spectator proton (p_s) and the soft photon from the Σ^0 decay have to be detected in the CLAS in order to exclusively identify the reactions.

The acceptance calculation is based on the implementation of the Mart-Bennhold model as KAONMAID^[22] which is used as input for Monte Carlo tracking through a GEANT3^[36] representation of the CLAS detector, including the HD target within the BNL cryostat (cf. Figure 11). NMR coils and a solenoidal holding field of 0.9 T were included as well. Charged particles are identified through reconstructed tracks in the drift chamber system (DC) and time information from the start counter (ST) and time-of-flight counters (SC). We have assumed that the torus field is set to 40 % of its maximum value. The comparatively low field allows for high efficiency in the detection of π^- and positively charged particles with good resolution. We have considered both signs for the torus field, $I = +1500\text{A}$ with positive particles swept outwards and $I = -1500\text{A}$ with negative particles swept outward. Neutrons are identified as clusters in the electromagnetic calorimeters (EC) with an efficiency of 20-50%, as shown in Figure 12, or in the Time-of-flight counters (SC) with lower efficiency. Clusters in the EC from neutrals are separated from charged ones by checking for extrapolated tracks in the neighborhood of the

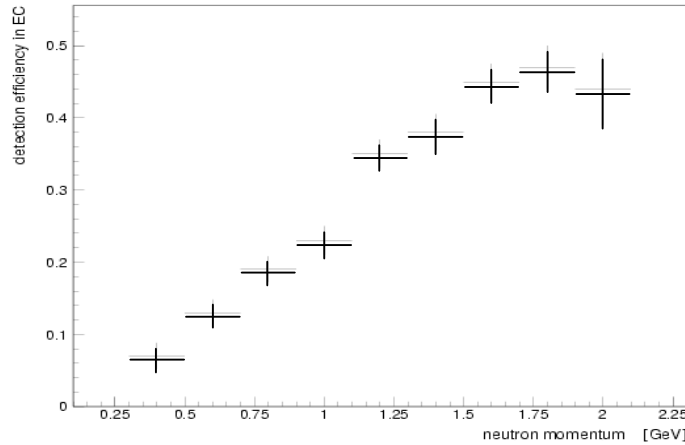


Figure 12: Efficiency of neutron detection in the CLAS forward calorimeter (EC).

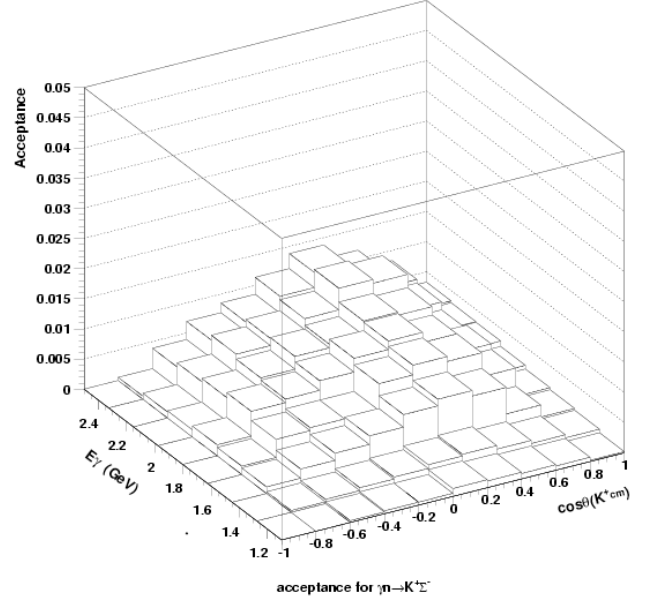
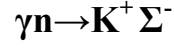
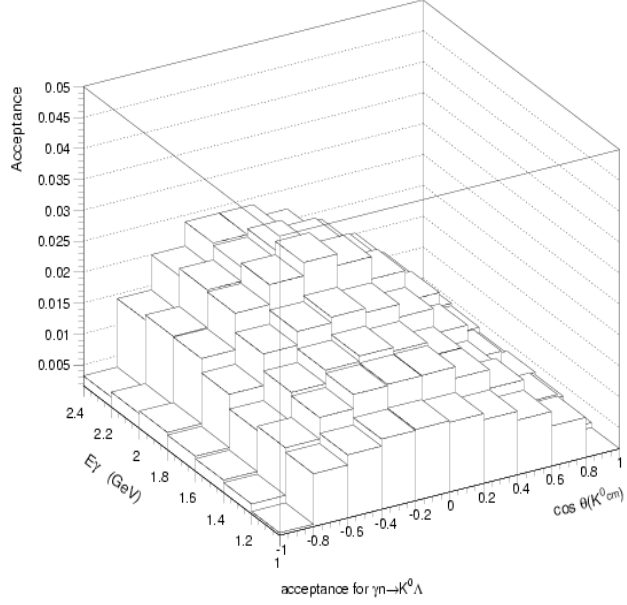
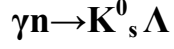


Figure 13. Acceptance for hyperon photo-production from neutrons with a torus setting of $I = +1500A$. This analysis requires the detection of all final state particles in these reaction, it does not require the detection of the spectator proton.

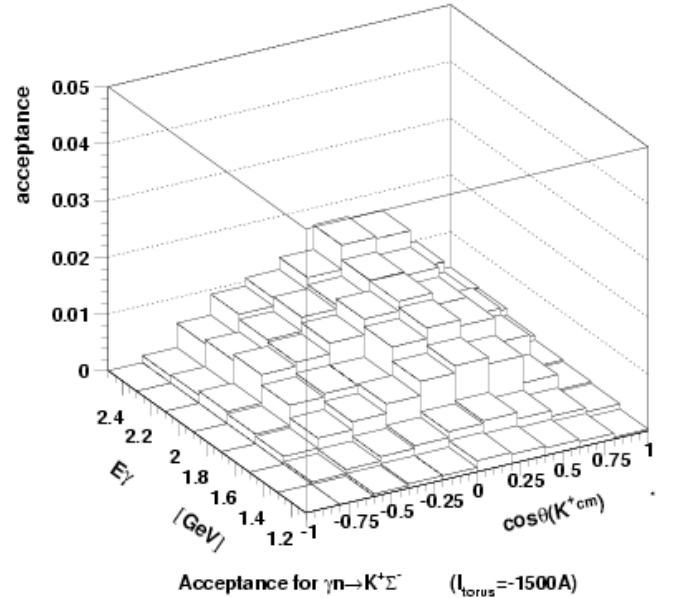
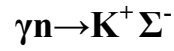
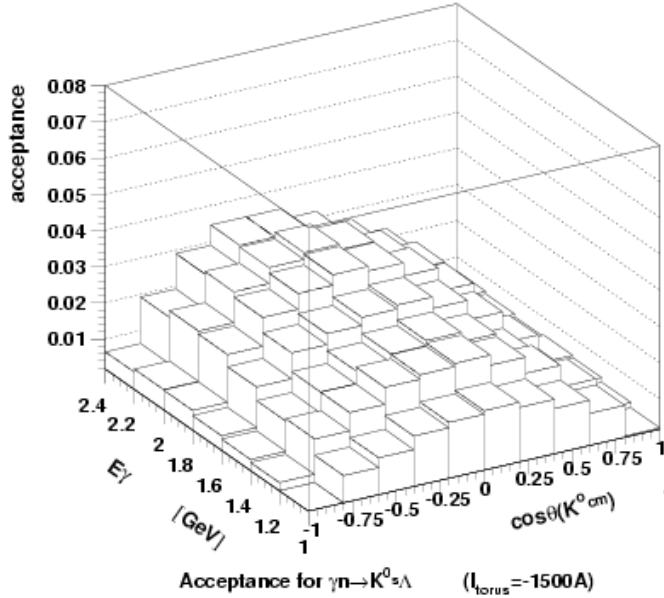
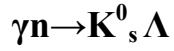


Figure 14. Acceptance for hyperon photo-production from neutrons with a torus setting of $I = -1500A$. This analysis requires the detection of all final state particles in these reaction, it does not require the detection of the spectator proton.

cluster. The slight efficiency drop at higher neutron momenta is caused by cuts in the EC timing information to separate neutrons from photons ($\beta_{EC} < 0.95$). While the time-of-flight scintillators are used as well to identify neutrons, they do not contribute strongly to the reconstructed yield since the efficiency is of order 5—7 %. The results of our simulation are consistent with the experimentally determined neutron efficiency^[37]. The net CLAS acceptance for the $I = +1500A$ and $I = -1500A$ settings of the torus are shown in Figure 13 and Figure 14. The acceptance with $I = -1500A$ is higher and will be used for polarized D measurements.

2.2 Backgrounds

Several studies have been performed to estimate the background from electromagnetic and hadronic reactions. 10^8 beam photons were generated with start times mimicking the CEBAF beam structure⁴ and following the energy spectrum of incoherent bremsstrahlung between 10 MeV and 1.7 GeV.

The photons are produced in a cross sectional disc of 2.6 mm diameter, which is the diameter of the standard Hall-B bremsstrahlung collimator, located 5.8 m from the radiator. The half-angle is then $1.3/5800 = 0.22$ mrad (which is quite close to the characteristic angle of m_e/E_e). The target is located at the center of CLAS, which is 16 m downstream of the collimator. The image of the collimator on the target is 10 mm diameter. (The standard HD targets in use at BNL are 25 mm diameter. Due to the small beam spot available in Hall-B, the diameter of HD targets for this experiment can be reduced to somewhere between 10-15 mm, which has a variety of technical advantages, as discussed in Appendix A.)

Interactions of photons with beamline foils, HD target material, etc., resulted in about 180k events with hits in any of the 24 start counter paddles producing ADC and TDC digitizations⁵. The predominantly electromagnetic background, largely pair production, caused a high rate in

⁴ We produced the photons within a 20 nsec time interval in 150 psec bunches separated by 2.004 nsec.

⁵ Energy deposited in the 2.2mm thick counter was required to be larger than 0.4 MeV; minimum ionizing particles release ca. 0.49 MeV in the paddles.

the forward “nose” of the start counter, however the simulated data do not show any noticeable contamination of the drift chambers: 45137 events had track segments in the drift chambers, most of them from particles backscattered from the downstream shielding. Only 3372 events had two or more tracks and could have triggered the data readout. The rate in the time-of-flight counters, 120k events, was of the order of the observed rate from cosmics. Note that the rate in the start counter was more than 60 times higher for a simulation without the 0.9 T holding field of the HD cryostat, as most reaction products were low energetic particles. With HD, the accidental rate in coincidence with out of time tagger buckets was about equal to the true rate. These results are summarized in Table 3.

An equivalent set of beam photons was used to estimate the background that would be present with a deuterated-butanol target using the FROST target (including a solenoidal holding field of 0.4 T). The resulting rate was $4.6 \cdot 10^6$ events with hits in the start counter, $3.0 \cdot 10^6$ events

Table 3. Event rates from HD and from deuterated-butanol target simulations.

	HD	C₄D₉OD
<i>N_γ photons on tgt</i>	10⁸	10⁸
<i>start-counter (ST) hits</i>	180 K	4600 K
<i># TOF counters (SC)</i>	120 K	3000 K
<i>drift chamber (DC) tracks</i>	45 K	1100 K
<i># 2-track triggers</i>	3.4 K	80 K
<i>true/accidentals</i>	1/1	1/20

with hits in the time-of-flight counters, and $1.1 \cdot 10^6$ events with track segments in the drift chambers, of which about 80k events had two or more tracks. Due to the substantially higher rates with Butanol, the accidental rate from out of time tagger buckets was about 20 times the true rate. These results are summarized in the last column of Table 3.

The results reflect roughly the relative electromagnetic rate between HD and butanol target though a pure Z^2 scaling would give a 33 times higher rate on deuterated butanol. Additional material like target walls (CTFE), aluminum cooling wires in the HD target cell, or the $^3\text{He}/^4\text{He}$

bath around the FROST target as well as hadronic interactions lowered the ratio to factors of about 20 to 25.

2.3 Sample analyses

Data for many hadronic processes will be taken simultaneously. In most cases not all final state particles can be detected and the missing mass technique can only be used with limitations because of (a) Fermi motion of the target nucleons and (b) limited kinetic energy of spectator particles. Additionally, due to limitations in detector resolution, misidentification of reconstructed particles typically causes more difficulties with reactions on deuterium than hydrogen. However, combinations of several cuts in the analysis usually allows for a good separation of specific channels.

The goal of the following sample analyses was to reproduce the polarization input parameters given by the Mart-Bennhold model. For the simulation of $\gamma d \rightarrow p K^0 \Lambda$, two sets of 250,000 events in $\Delta E_\gamma = 100$ MeV were generated, one following the angular distribution for positive and the other for negative helicity. Compared to $K^0 \Lambda$ production, the cross sections for $K^0 \Sigma^0$ and $K^+ \Sigma^-$ production are roughly in the ratio of 1:1 and 1:5, respectively. Thus, corresponding sets with the same statistics were generated for $\gamma d \rightarrow p K^0 \Sigma^0$ and sets of 50,000 events for $\gamma d \rightarrow p K^+ \Sigma^-$. Each set was used twice in the simulation: once for aligned beam and target spins, once for opposite spin directions. Additionally, background reactions were simulated in accordance with their estimated cross section ratios⁶ following eq. (3) for elementary reactions on both protons and neutrons, using the Paris potential to describe the momentum distribution of the spectator. The simulated background reactions include: $\gamma d \rightarrow p_s p \pi^+ 2\pi^- \pi^0$, $p_s n 2\pi^+ 2\pi^-$, $n_s p 2\pi^+ 2\pi^-$, $p_s n \pi^+ \pi^-$, $p_s n \pi^+ \pi^- \pi^0$, $n_s K^+ \Lambda \pi^0$, $n_s K^+ \Sigma^0$, $n_s n 2\pi^+ \pi^-$, $n_s p \pi^+ \pi^-$, $n_s p \pi^+ \pi^- \pi^0$. Additionally, events produced on the target cell walls⁷ and aluminum wires are simulated with larger Fermi momenta.

⁶ The ratios were estimated from the compilation in Landolt-Brönstein, Vol. I/8.

⁷ Cell walls are made of 0.065 g/cm² CTFE ('Kel-F') consists of carbon, fluorine and chlorine in the ratio of C:F:Cl=2:3:1 with net density of 2.12 g/cm³ (see Appendix A).

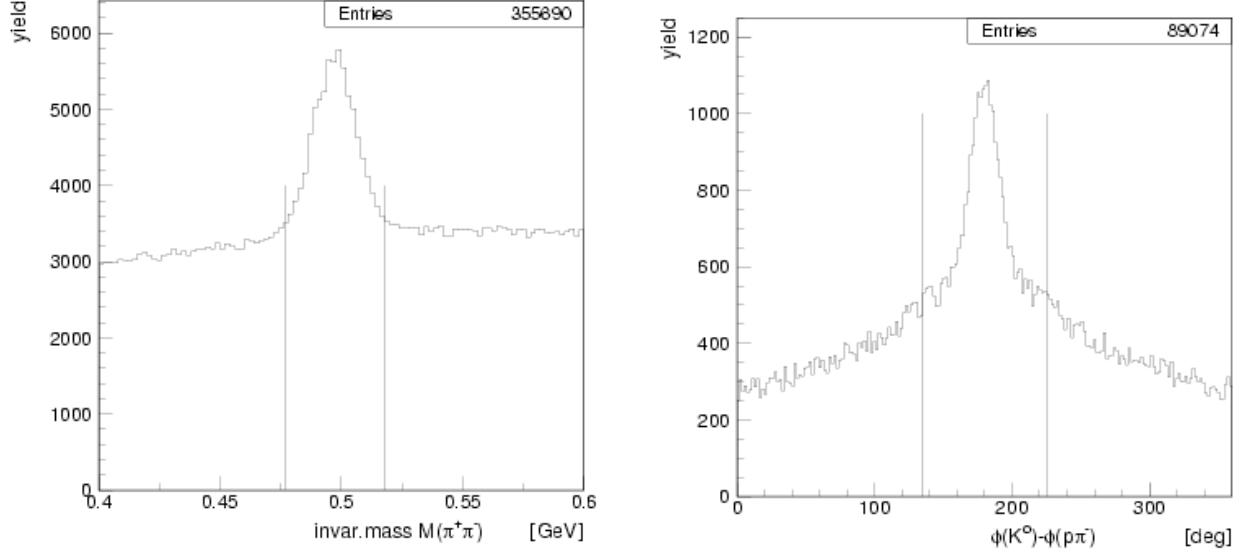


Figure 15: Reactions on an HD target: Invariant mass distribution of $\pi^+\pi^-$ with cut on M_{K^0} (left); relative azimuthal angle of the meson (K^0) and baryon system ($p\pi^-$) with a loose cut on coplanarity (right).

The reactions $\gamma n \rightarrow K^0 \Lambda$ and $\gamma n \rightarrow K^0 \Sigma^0$ are identified by the detection of all charged final-state particles except the spectator proton, i.e. $p \pi^+ 2\pi^-$. With all four particles detected, the invariant mass is formed with the π^+ and the π^- whose invariant mass with the π^+ is closest to m_{K^0} . As shown in Figure 15, a tight cut is placed on the reconstructed K^0 mass, identified via the decay $K^0_S \rightarrow \pi^+\pi^-$, and subsequently a coplanarity cut is placed on the meson ($\pi^+\pi^-$) and baryon ($p\pi^-$) systems of $\Delta\phi \in 180^\circ \pm 45^\circ$. This results in well separated distributions in a Dalitz plot of the missing mass squared of all identified particles, $MM^2(\gamma d \rightarrow (\pi^+\pi^-)(p\pi^-)X)$, versus the missing mass squared of $MM^2(\gamma n \rightarrow K^0 X)$, assuming the neutron is at rest. As shown in Figure 16, the Λ signal in $MM^2(\gamma n \rightarrow K^0 X)$, the lower-left peak, is directly correlated with the proton mass squared in $MM^2(\gamma d \rightarrow \pi^+\pi^-p\pi^-X)$, though the Λ peak is broadened. The projection in $MM^2(\gamma n \rightarrow K^0 X)$ after a cut on the proton mass, $0.83 < MM^2(\gamma d \rightarrow \pi^+\pi^-p\pi^-X) < 0.92 \text{ GeV}^2$, shows a strong Λ signal above an almost smooth background; only at high mass squared the tail from the Σ^0 signal distorts the symmetric shape – the contamination, however, is small. The Σ^0 signal itself, upper-right peak, is comparatively broad but well separated, with $MM^2(\gamma d \rightarrow \pi^+\pi^-p\pi^-X)$ larger than the proton mass due to the missing soft photon from the decay $\Sigma^0 \rightarrow \Lambda\gamma$.

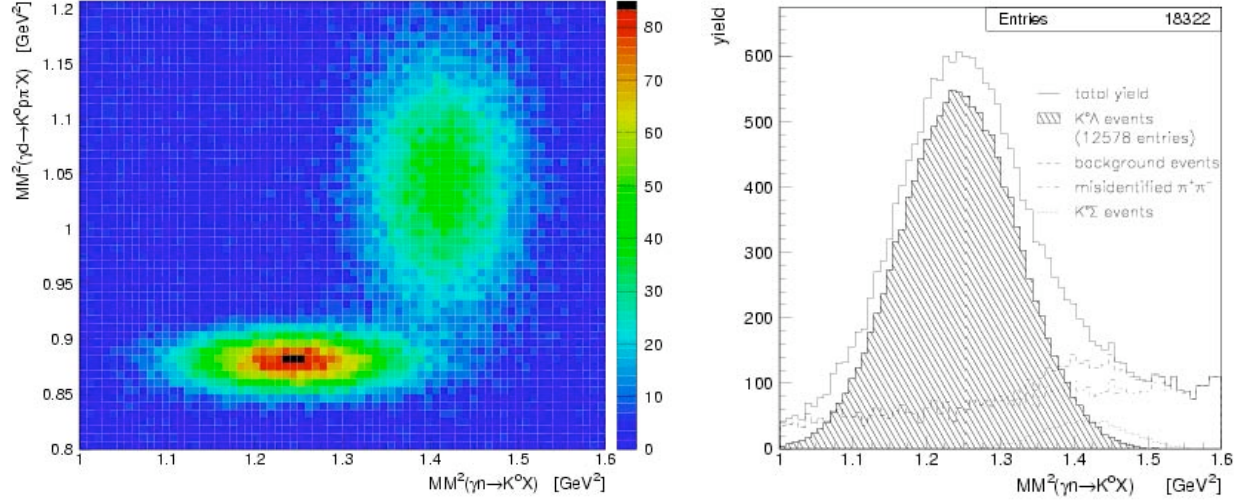


Figure 16: Reactions on an HD target: Dalitz plot of $MM^2(\gamma d \rightarrow K^0 \pi^+ p X)$ vs. $MM^2(\gamma n \rightarrow K^0 X)$ after cut on the invariant mass of $\pi^+ \pi^-$ and a coplanarity cut, cf. Fig. 8. On the right, the projection of the Dalitz plot after a cut in $MM^2(\gamma d \rightarrow K^0 \pi^+ p X)$ around the missing (spectator) proton.

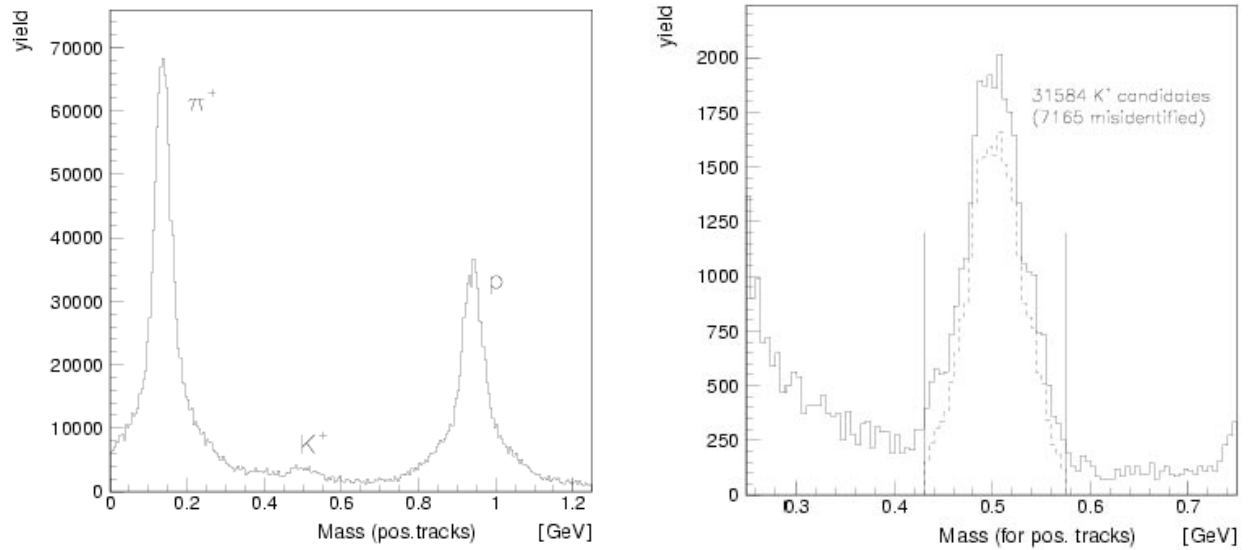


Figure 17: Reactions on an HD target: Mass spectrum without kinematic requirements (left) and after requiring a π^- and a neutral cluster in the direction of the missing momentum of the π^- and a charged particle (right). A subsequent cut in reconstructed mass, as indicated in the right panel, provides a clean selection for the K^+ events (dashed histogram).

The analysis of $\gamma n \rightarrow K^+ \Sigma^-$ is based on the detection of $K^+ \pi^- n$. Particle identification is based on the mass calculation from the reconstructed momentum, track-length, and time of flight ($m=p/\beta\gamma$). The requirement of a π^- and a neutral cluster in the direction of the missing momentum

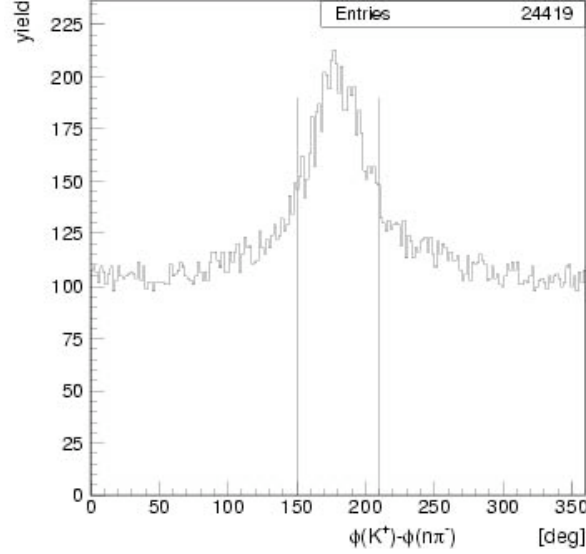


Figure 18. Reactions on an HD target: Coplanarity cut on the azimuthal angle between the K^+ and the baryon system ($n\pi^-$)

of the π^- and a charged particle provides a clear K^+ signal above the tail of the π^+ yield, as shown in Figure 17. However, most of the K^+ events appear not to be correlated with $n\pi^-$ from Σ^- decay, as shown in the azimuthal $\phi(K^+) - \phi(\pi^- n)$ distribution of Figure 18. The background is mainly from K^+ events on a proton, where the recoil neutron is detected in CLAS or a photon shower in the EC is misidentified as a neutron. The subsequent coplanarity cut on the K^+ and the baryon system ($n\pi^+$) provides an excellent means to remove the large background contribution. The resulting Dalitz plot is shown in Figure 19. The dominant Σ^- signal in $MM^2(\gamma n \rightarrow K^+ X)$, calculated under the assumption of a neutron at rest, is directly correlated with the proton mass squared in $MM^2(\gamma d \rightarrow K^+ (n\pi^-) X)$. The background does not show strong structures, only enhancements from misidentified π^+ at unphysical low mass squared and from some $K^+ p$ events around the Λ and Σ^0 mass but at higher mass squared in $MM^2(\gamma d \rightarrow K^+ \pi^- n X)$ than the nucleon. A projection in $MM^2(\gamma n \rightarrow K^+ X)$, after a cut on the proton mass in the other projection, $0.83 < MM^2(\gamma d \rightarrow K^+ \pi^- n X) < 0.92 \text{ GeV}^2$, results in a well separated Σ^- signal above a smooth background, as shown in the right panel of Figure 19.

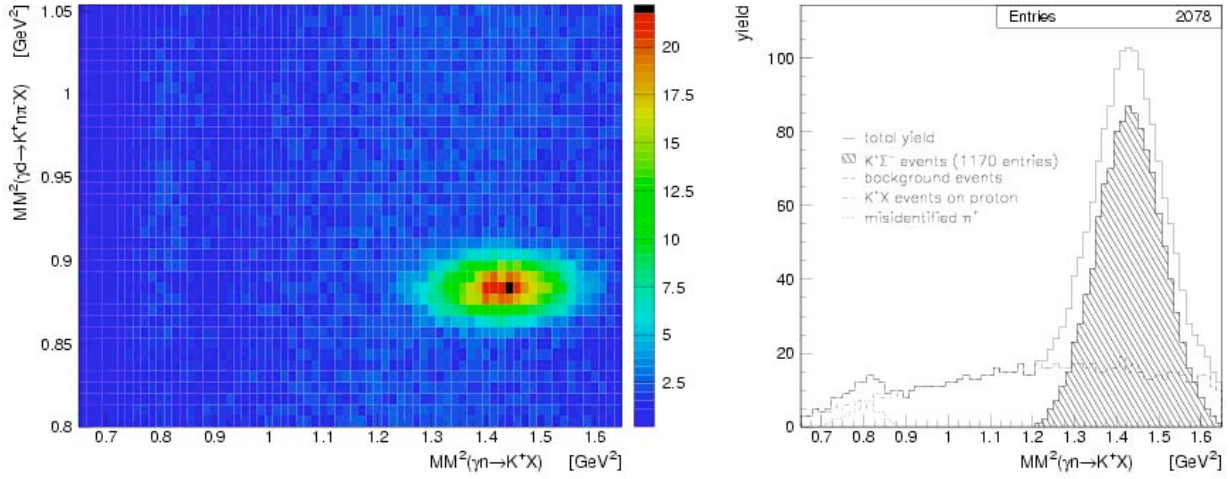


Figure 19: Reactions on an HD target: Dalitz plot of $MM^2(\gamma d \rightarrow K^+ \pi^- nX)$ vs. $MM^2(\gamma n \rightarrow K^+ X)$ after identification of K^+ and a coplanarity cut (left); projection on $MM^2(\gamma n \rightarrow K^+ X)$ for $0.83 < MM^2(\gamma d \rightarrow K^+ \pi^- nX) < 0.92 \text{ GeV}^2$ with identified background distributions.

The same generated events were passed through the GEANT3 representation of the CLAS detector including the design geometry of the FROST target. Additionally, events were generated on carbon and oxygen in order to account for contributions from bound nucleons in deuterated butanol (C_4D_9OD) in their relative cross section ratio⁸ as well as on helium and CTFE ($^3\text{He}/^4\text{He}$ bath and target walls). The contribution of reactions on bound nucleons, generated as unpolarized distributions with corresponding Fermi momenta (CERNLIB routine `genbod`), is much larger than that of the reactions of interest. Figure 20 (analogous to Figure 16 for the HD target) shows the Λ signal above a large background. The same cuts were used to extract the yield shown in the right panel.

With FROST, the situation is much worse for the $K^+ \Sigma^-$ channel where a slight enhancement at proton mass squared and Σ^- mass squared can be seen in the Dalitz plot in Figure 21, but applying the same cut on the proton mass, $0.83 < MM^2(\gamma d \rightarrow K^+ \pi^- nX) < 0.92 \text{ GeV}^2$, does not provide a projection that allows separation of the Σ^- signal. The situation for the $K^0 \Sigma^0$ channel is similar.

⁸ Photon cross sections for constituents $\sigma_D : \sigma_C : \sigma_O \sim 38\text{mb} : 330\text{mb} : 560\text{mb}$ for $E_\gamma \sim 1 \text{ GeV}$ were weighted by the number of elements giving a ratio of the deuteron contribution to the remaining nuclei of 1:5.

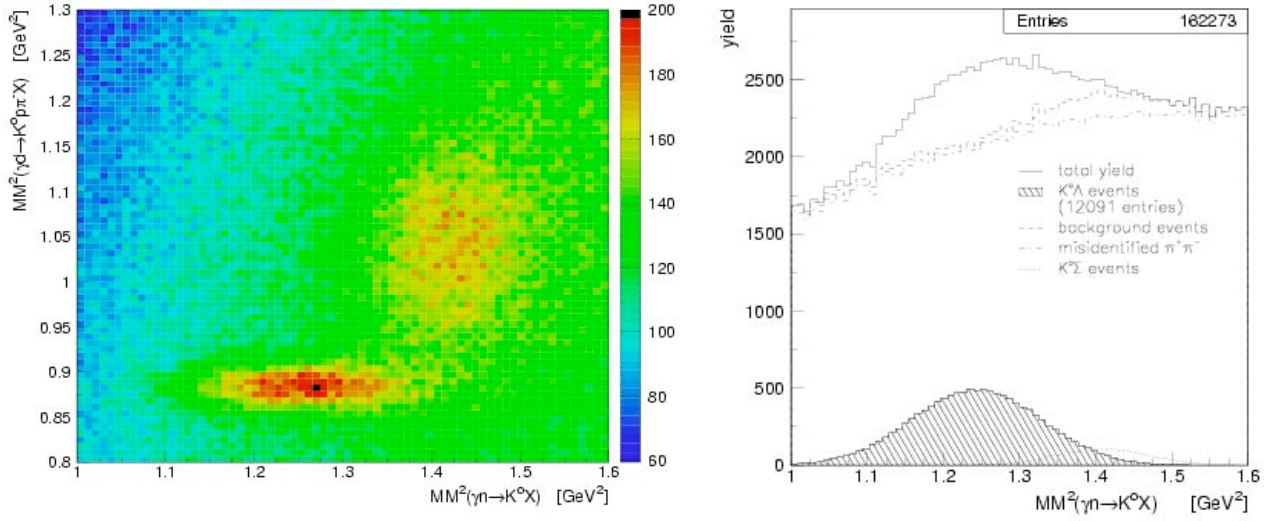


Figure 20: Reactions on a deuterated butanol (FROST) target: Dalitz plot of $MM^2(\gamma d \rightarrow K^0 \pi^+ p X)$ vs. $MM^2(\gamma n \rightarrow K^0 X)$ after cut on the invariant mass of $\pi^+ \pi^-$ and a coplanarity cut (left). On the right the projection of the Dalitz plot after a cut in $MM^2(\gamma d \rightarrow K^0 \pi^+ p X)$ around the missing (spectator) proton. Note the suppressed zero used for the scale in the left panel.

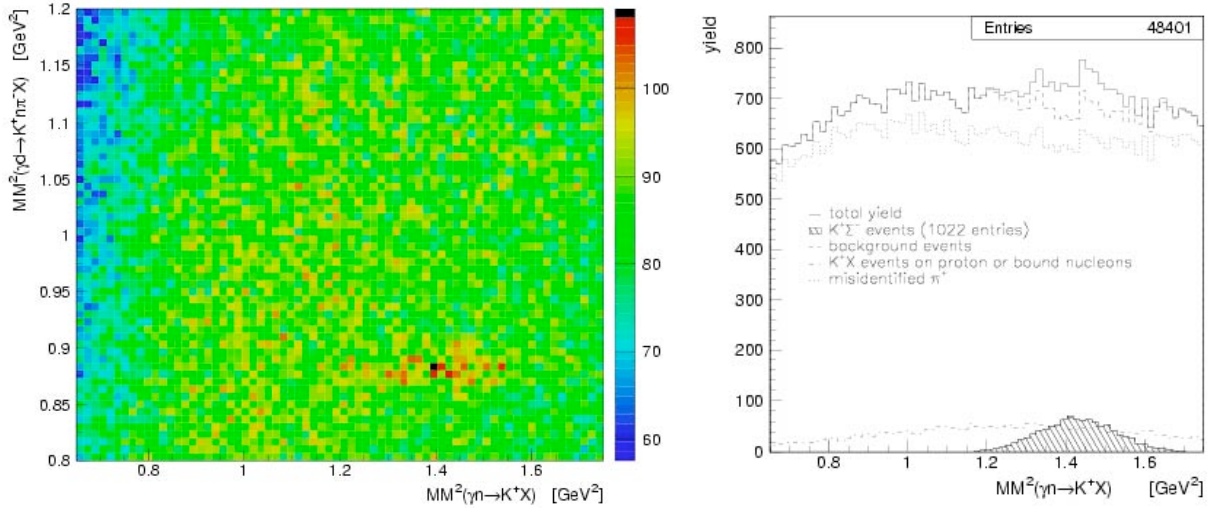


Figure 21: Reactions on a deuterated butanol (FROST target): Dalitz plot of $MM^2(\gamma d \rightarrow K^+ \pi^- n X)$ vs. $MM^2(\gamma n \rightarrow K^+ X)$ after identification of a K^+ and a coplanarity cut (left); projection on $MM^2(\gamma n \rightarrow K^+ X)$ for $MM^2(\gamma d \rightarrow K^+ \pi^- n X) < 0.92 \text{ GeV}^2$ with identified background distributions. Note the suppressed zero used for the scale in the left panel.

A tighter cut on the K^0 signal in the invariant mass distribution $M(\pi^+ \pi^-)$, with a subsequently tighter coplanarity cut, as shown in Figure 22, enhances considerably the signal to background

ratio as shown in Figure 23. However, the $K^0\Sigma^0$ yield is severely reduced. The $K^0\Lambda$ yield is only reduced by 30% and allows for an analysis of this channel, although the subtraction of the large background, using a polynomial background fit or sideband subtraction, results in large uncertainties.

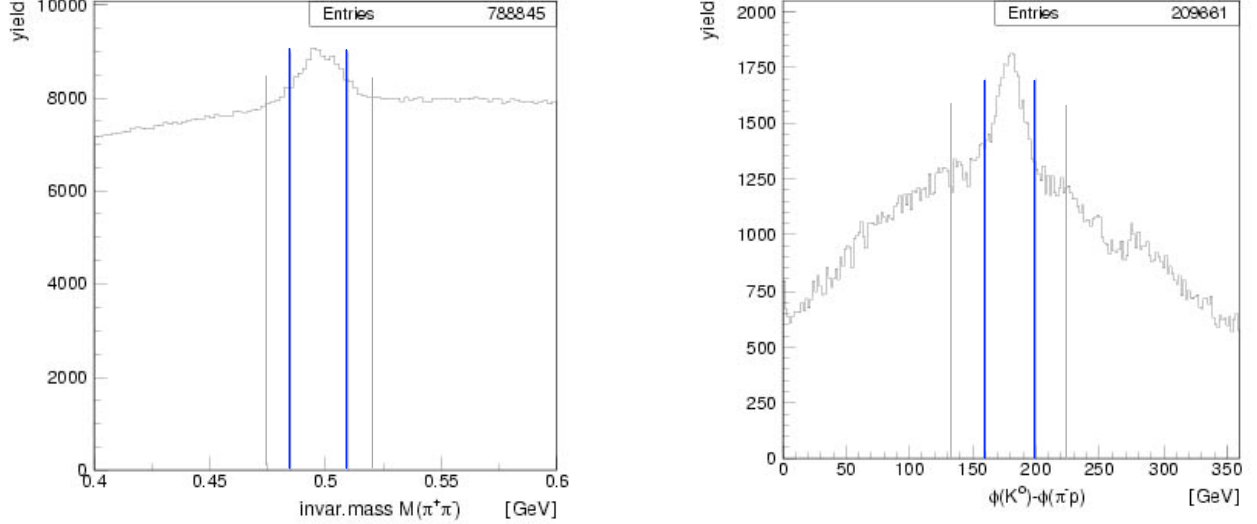


Figure 22: Reactions on a deuterated butanol (FROST) target: Invariant mass distribution of $\pi^+\pi^-$ with cut on m_{K^0} (left); relative azimuthal angle of the meson (K^0) and baryon system ($p\pi^-$) with cut on coplanarity (right). The cuts indicated in grey are the same as those with HD (Figure 15) and were used to generate the distributions of Figure 20 and Figure 21. The tighter cuts indicated in blue were used to generate the plots in Figure 23.

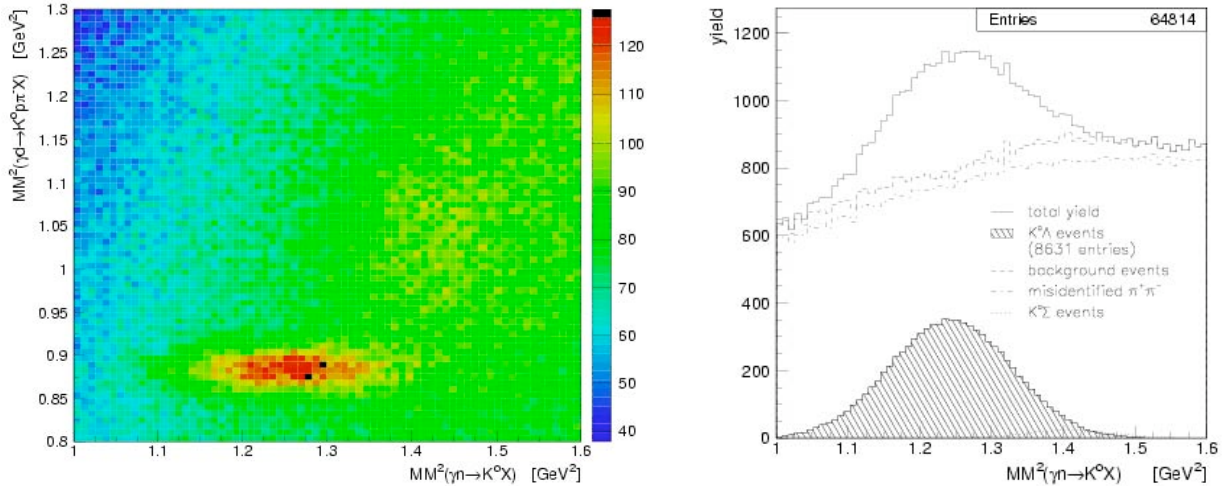


Figure 23: Reactions on a deuterated butanol (FROST) target: Dalitz plot of $MM^2(\gamma d \rightarrow K^0 \pi p X)$ vs. $MM^2(\gamma n \rightarrow K^0 X)$ (left) after the cuts shown in Fig. 14. On the right the projection of the Dalitz plot after a cut in $MM^2(\gamma d \rightarrow K^0 \pi p X)$ around the missing (spectator) proton. Note the suppressed zero used for the scale in the left panel.

The excellent reaction identification provided by the HD target allows for a reliable reconstruction of angular distributions and polarization observables. With the additional measurement of the Λ recoil polarization, the experiment provides an almost complete range of double polarization observables through the three sets beam-target, target-recoil and beam-recoil (Table 2). In total, the cross section and 13 polarization asymmetries will be measured (out of a total of σ and 15 polarization asymmetries) for the $\gamma n(p) \rightarrow K^0 \Lambda(p)$ reaction. (Only the F and H asymmetries which require a transversely polarized target would remain unmeasured.) Projected results are plotted for three different beam energies that span the energy range of the proposed measurements in Figure 24 through Figure 29. Projected errors for each energy bin are tabulated below in the section on *Count Rate Estimates* (see Table 5). The CLAS acceptance is somewhat higher with -1500A in the torus and that has been assumed for these reactions.

The single-spin beam asymmetry (Σ or S) and the beam-target double-polarization asymmetries (E and G) for the $\gamma n(p) \rightarrow K^0 \Sigma^0(p)$ and $\gamma n(p) \rightarrow K^+ \Sigma^-(p)$ reactions are plotted in

Figure 30 and Figure 31. Because of the lower analyzing power in Σ^0 decay ($\alpha_{\Sigma^0} = -\alpha_{\Lambda}/3$), only the single-spin recoil asymmetry (P) can be extracted in the $K^0 \Sigma^0$ channel. The analyzing power in Σ^- decay is quite small ($\alpha_{\Sigma^-} \approx -\alpha_{\Lambda}/10$) and no recoil asymmetries will be available.

For the polarized H running, a setting of +1500A in the CLAS torus provides a larger acceptance for the $\gamma p \rightarrow K^+ \Lambda \rightarrow K^+ p \pi^-$ channel, with two positively charged particles swept outward, as shown in Figure 32. The acceptance with either field polarity is much larger than the γ +D channels since, for γ +p $\rightarrow K^+ \Lambda$, the detection of two charged particles is sufficient to identify the final state. At $I = +1500A$, this is best accomplished by detecting a K^+ and a proton. (At $I = -1500A$, the best channel identification comes from the detection of a π^- and either a K^+ or a proton.) The much larger acceptance, combined with the higher H polarization, leads to comparatively small uncertainties in the asymmetries in only 13% of the running time. Polarized-H data collected at $I = +1500A$ will provide the B-T and T-R asymmetries for γ +p. (The S, P and B-R asymmetries will not be extracted due to the difficulty in subtracting the contributions from bound protons in deuterium.) The projected uncertainties for $\gamma p \rightarrow K^+ \Lambda$ are shown in Figure 33. The uncertainties on the $\gamma p \rightarrow K^+ \Sigma^0$ observables are shown in Figure 34.

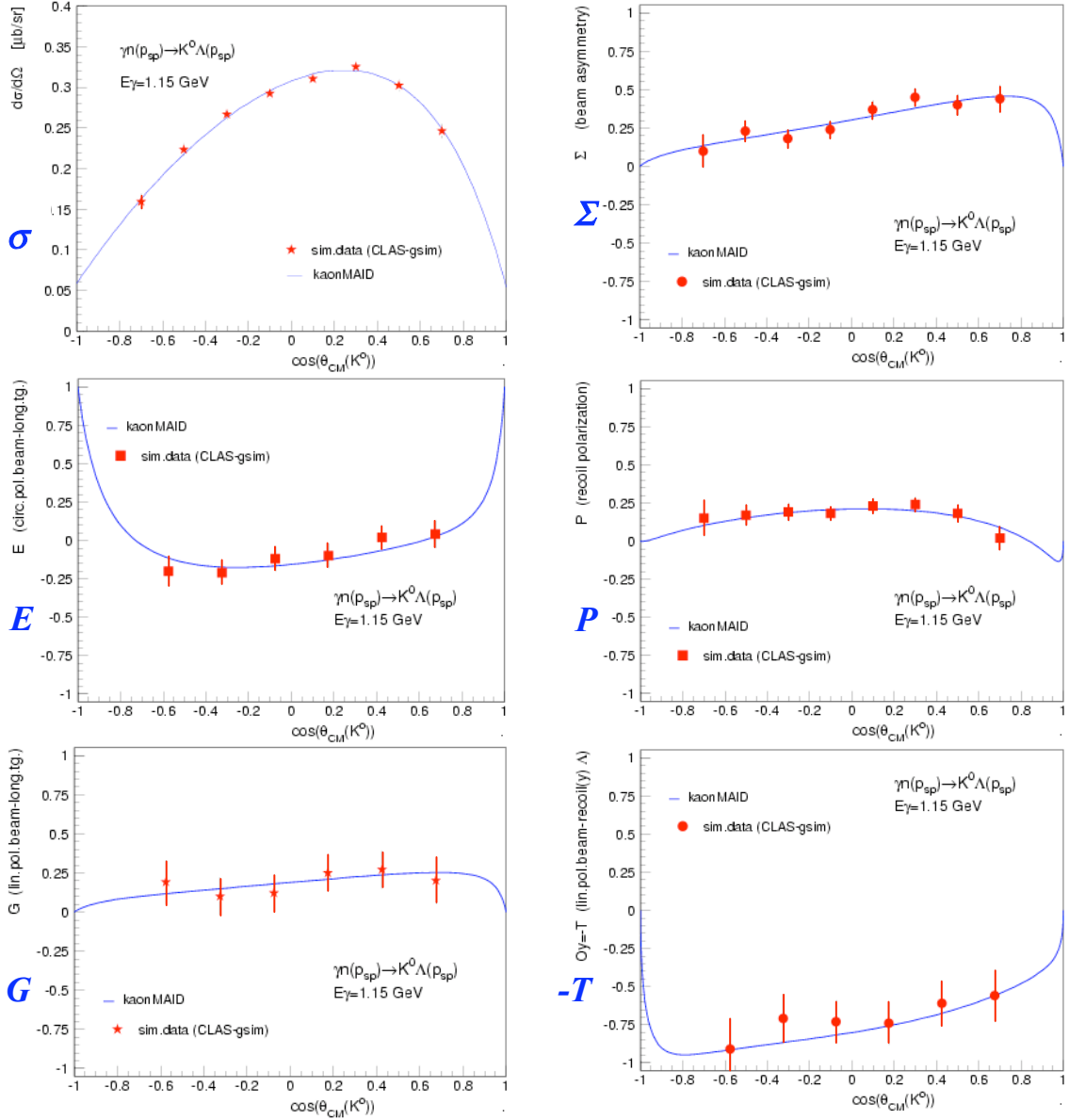


Figure 24. Projected cross sections and beam-target double-polarization asymmetries (E, G), left panels, and single-spin asymmetries (Σ, P, T), right panels, for the $\gamma n(p) \rightarrow K^0 \Lambda(p)$ reaction at $E_\gamma = 1.15$ GeV ($W = 1.745$ GeV).

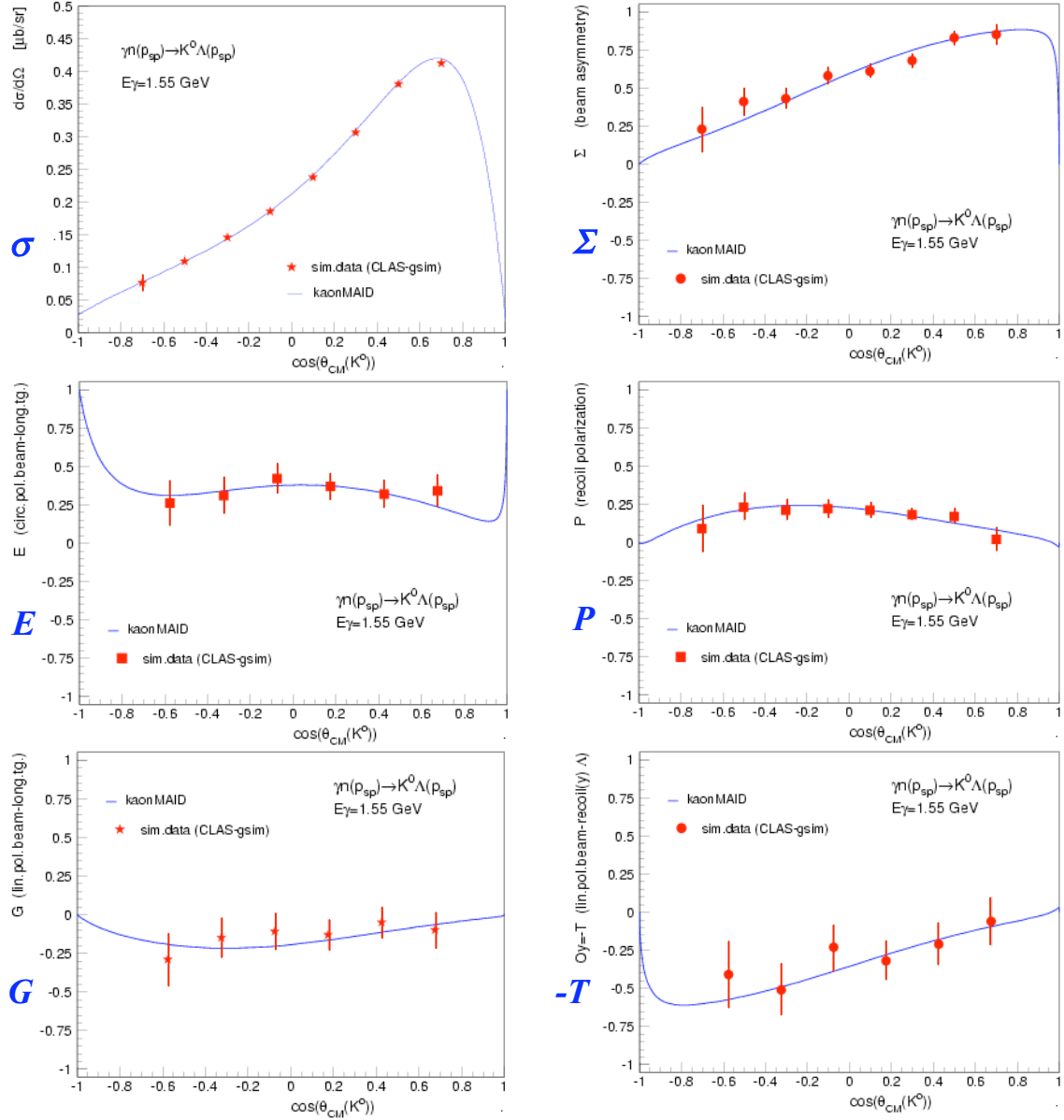


Figure 25. Projected cross sections and beam-target double-polarization asymmetries (E, G), left panels, and single-spin asymmetries (Σ , P, T), right panels, for the $\gamma n(p) \rightarrow K^0 \Lambda(p)$ reaction at $E_\gamma = 1.55$ GeV ($W = 1.948$ GeV).

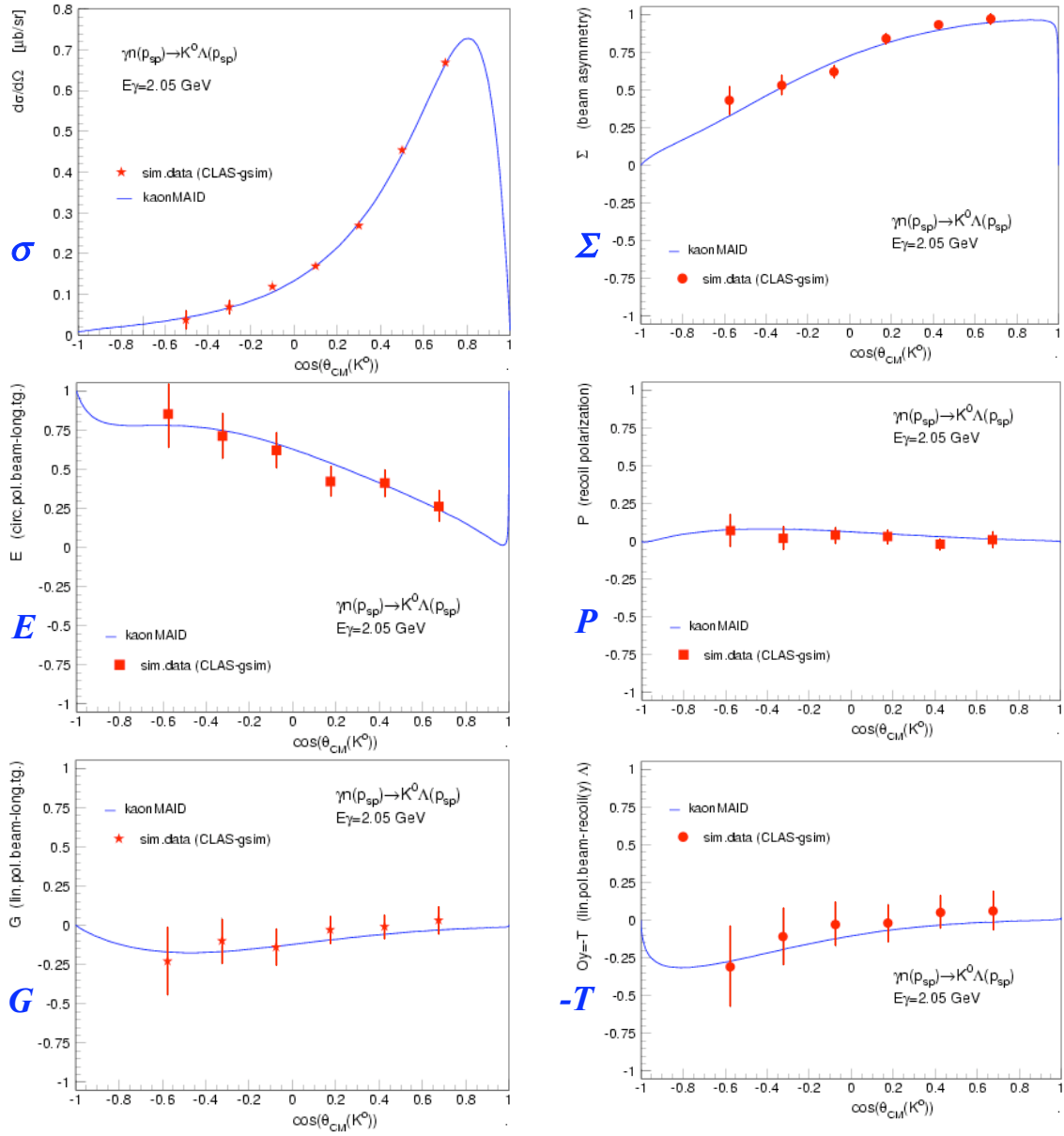


Figure 26. Projected cross sections and beam-target double-polarization asymmetries (E, G), left panels, and single-spin asymmetries (Σ, P, T), right panels, for the $\gamma n(p) \rightarrow K^0 \Lambda(p)$ reaction at $E_\gamma = 2.05$ GeV ($W = 2.176$ GeV).

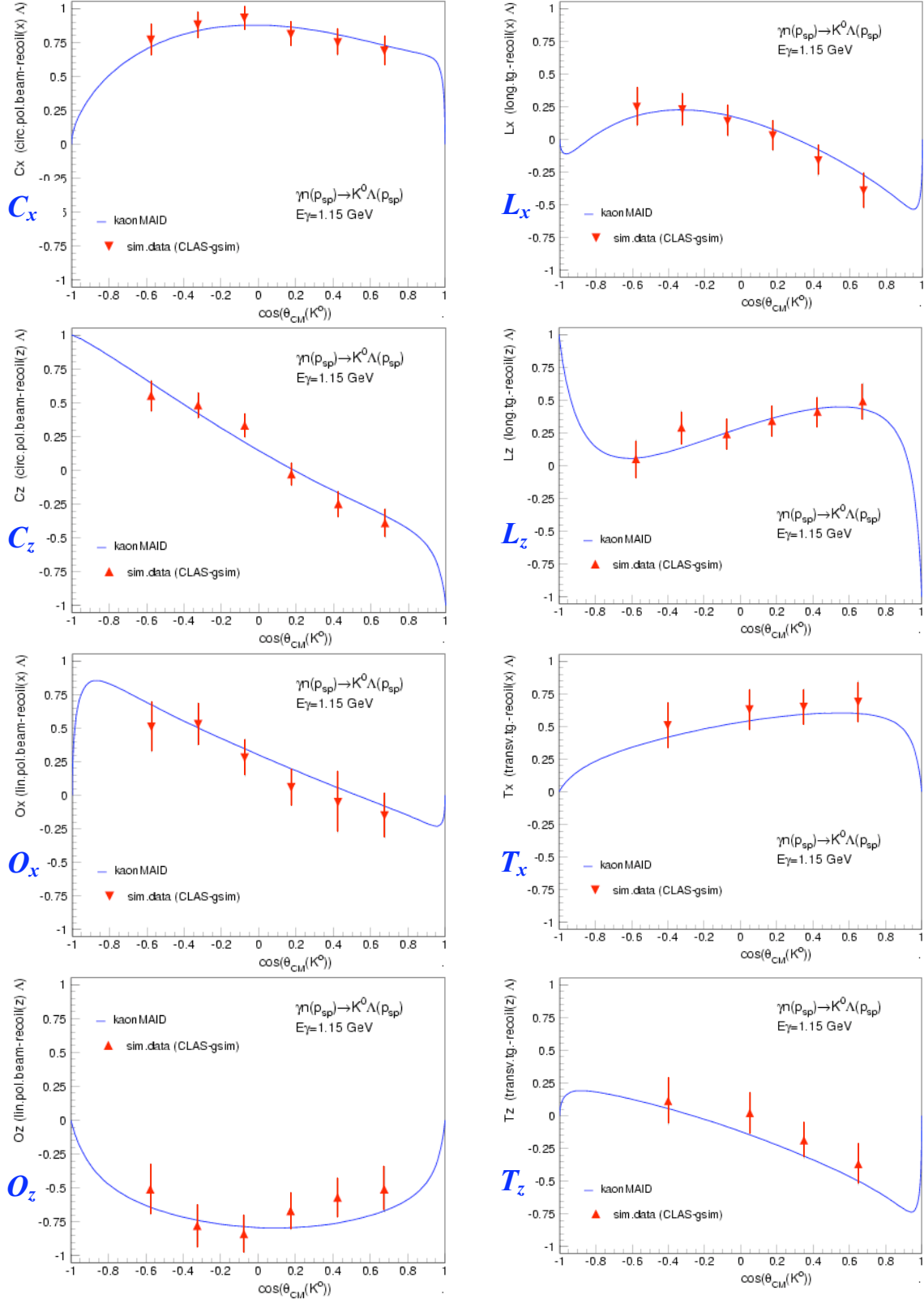


Figure 27. Projected double-polarization asymmetries for beam-recoil (C_x , C_z , O_x , O_z), left panels, and target-recoil (L_x , L_z , T_x , T_z), right panels, at $E_\gamma = 1.15$ GeV ($W = 1.745$ GeV) for $\gamma n(p) \rightarrow K^0 \Lambda(p)$.

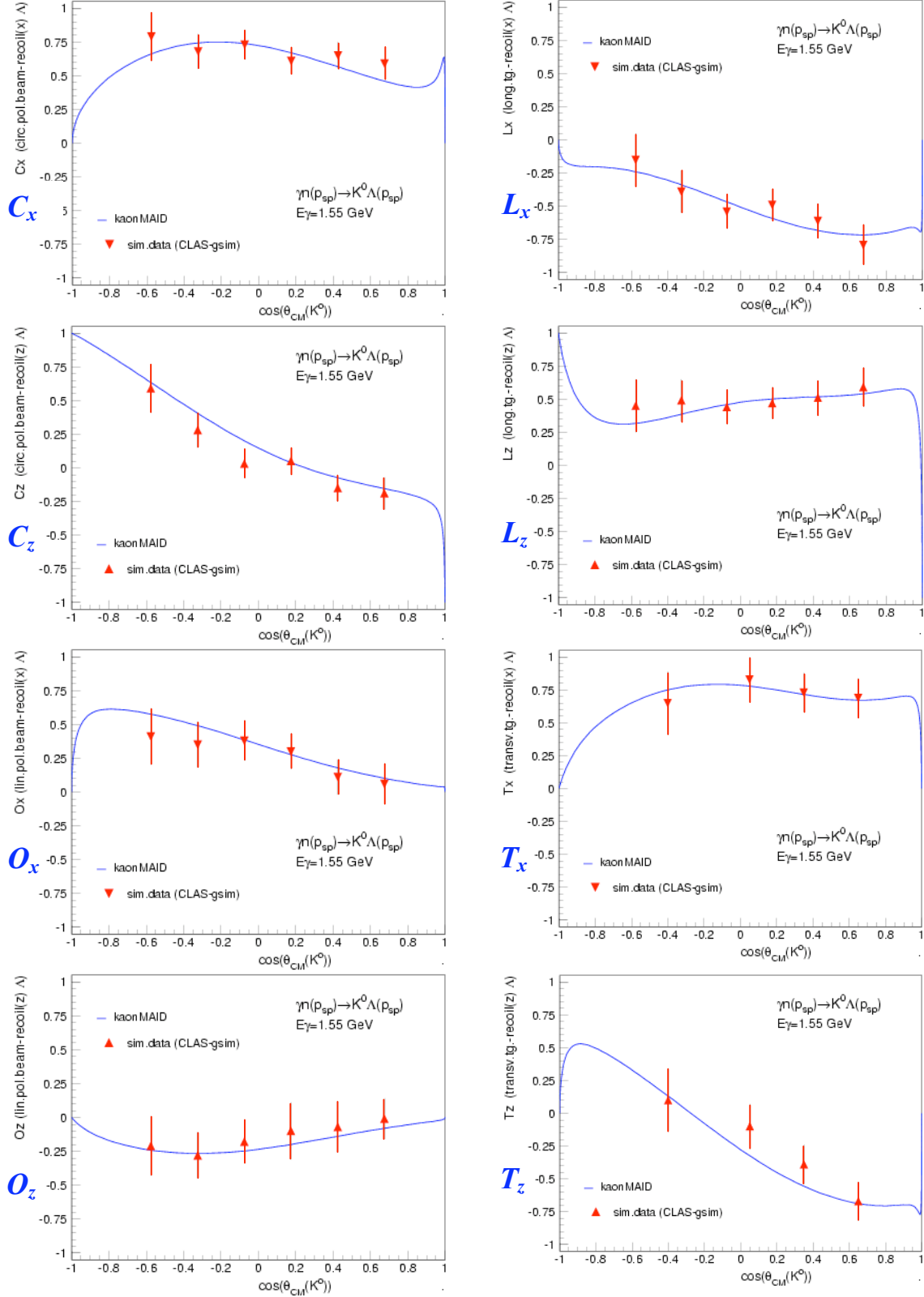


Figure 28. Projected double-polarization asymmetries for beam-recoil (C_x , C_z , O_x , O_z), left panels, and target-recoil (L_x , L_z , T_x , T_z), right panels, at $E_\gamma = 1.55$ GeV ($W = 1.948$ GeV) for $\gamma n(p) \rightarrow K^0 \Lambda(p)$.

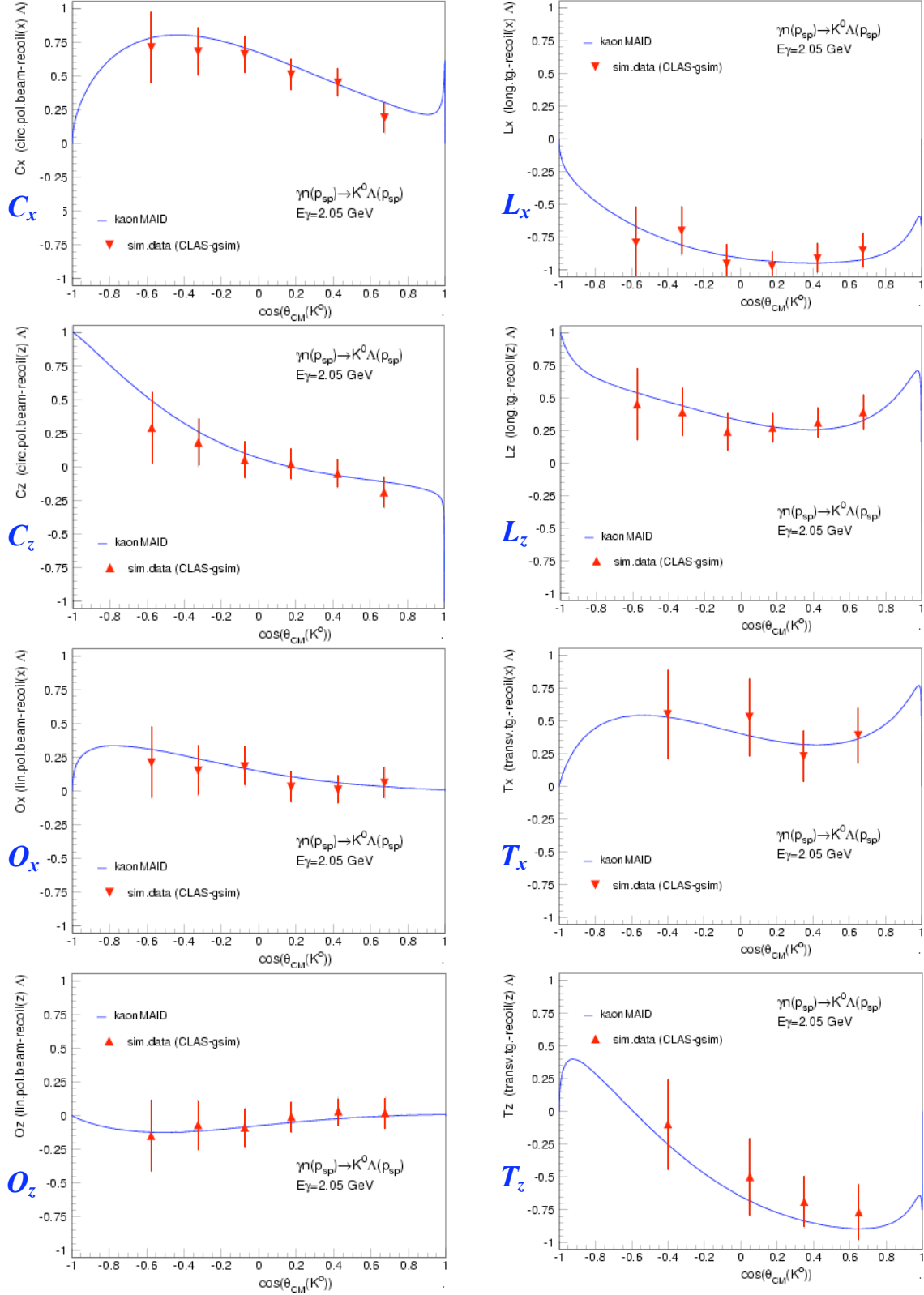


Figure 29. Projected double-polarization asymmetries for beam-recoil (C_x , C_z , O_x , O_z), left panels, and target-recoil (L_x , L_z , T_x , T_z), right panels, at $E_\gamma = 2.05$ GeV ($W = 2.176$ GeV) for $\gamma n(p) \rightarrow K^0 \Lambda(p)$.

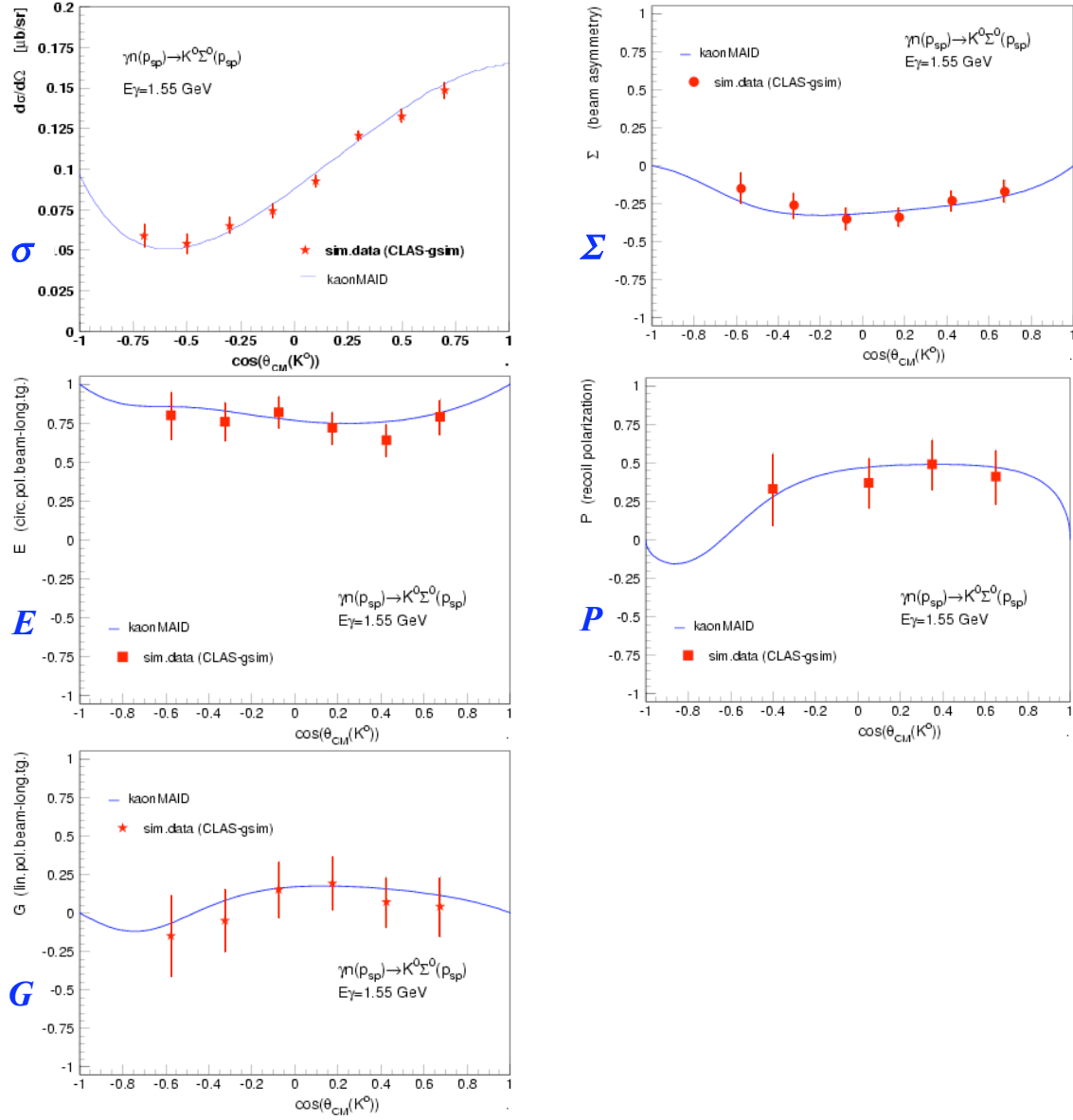


Figure 30. Projected cross sections and beam-target double-polarization asymmetries (E, G), left panels, and single-spin asymmetries (Σ, P), right panels, for the $\gamma n(p) \rightarrow K^0 \Sigma^0(p)$ reaction at $E_\gamma = 1.55$ GeV ($W = 1.948$ GeV).

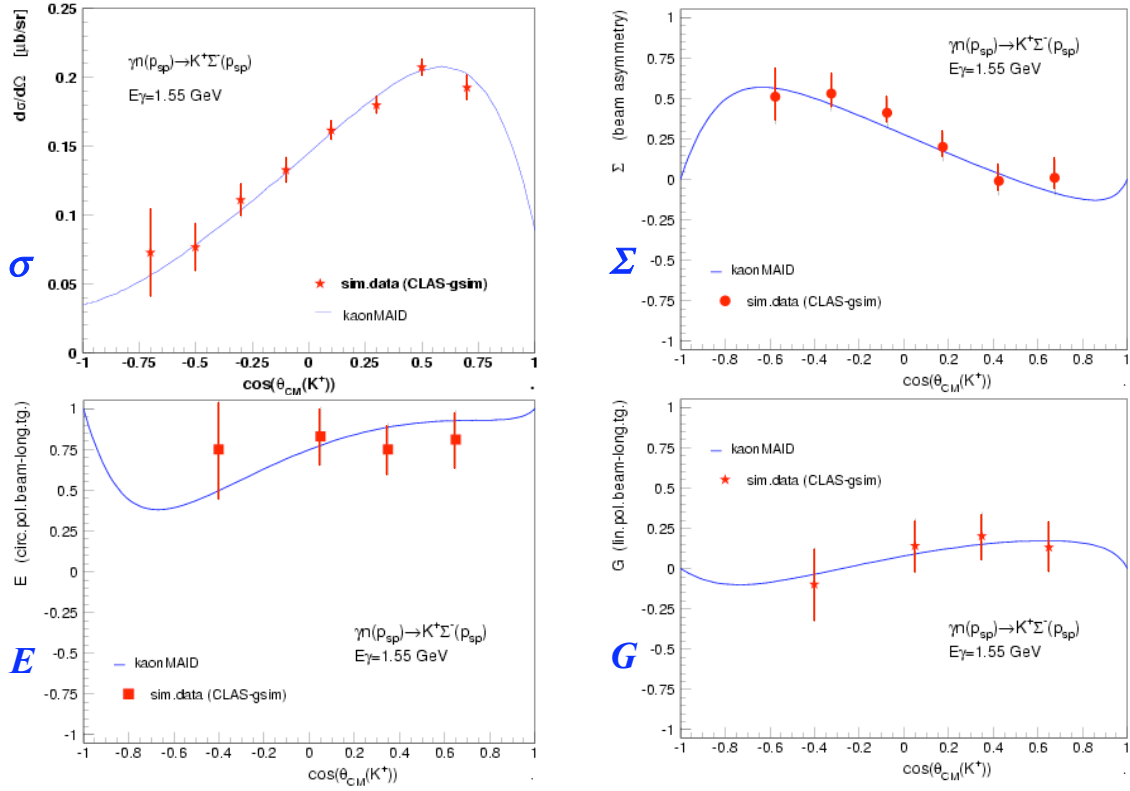


Figure 31. Projected cross sections and beam asymmetries (Σ), top panels, and beam-target double-polarization asymmetries (E , G), bottom panels, for the $\gamma n(p) \rightarrow K^+ \Sigma^-(p)$ reaction at $E_\gamma = 1.55$ GeV ($W = 1.948$ GeV).

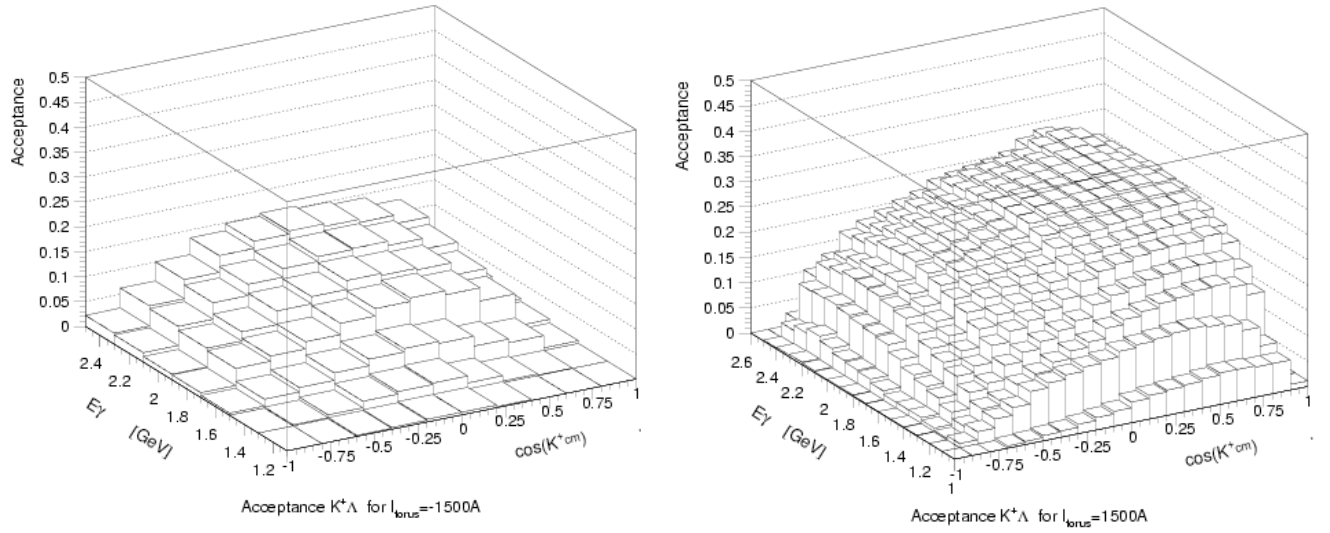


Figure 32. Acceptance for $\gamma p \rightarrow K^+ \Lambda$ with Torus currents of -1500 A (left) and +1500 A (right).

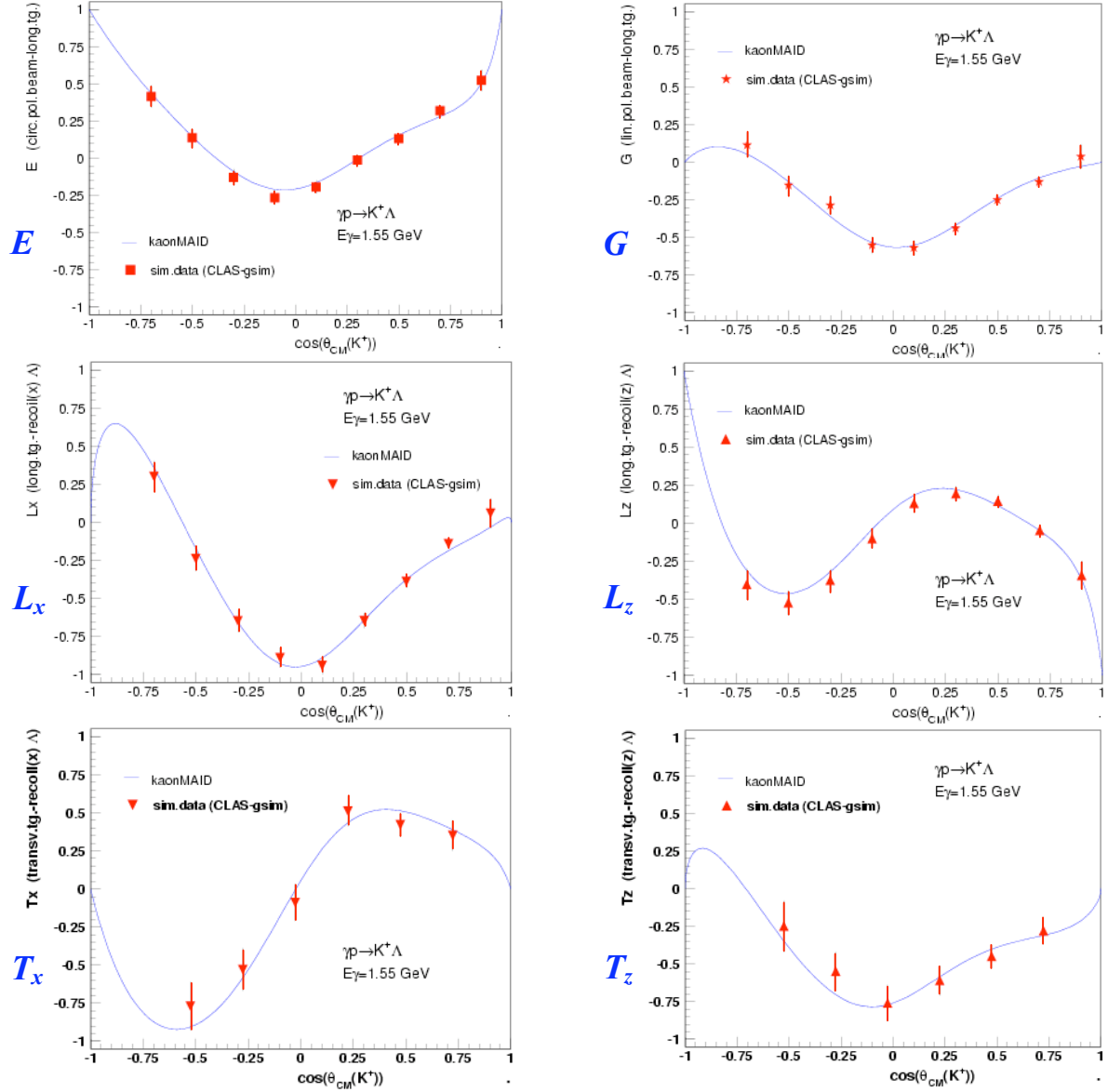


Figure 33. Double-polarization asymmetries for beam-target (E , G), top panels, and target-recoil (L_x , L_z , T_x , T_z), middle and bottom panels, at $E_\gamma = 1.55$ GeV ($W = 1.948$ GeV) for $\gamma p \rightarrow K^+ \Lambda$.

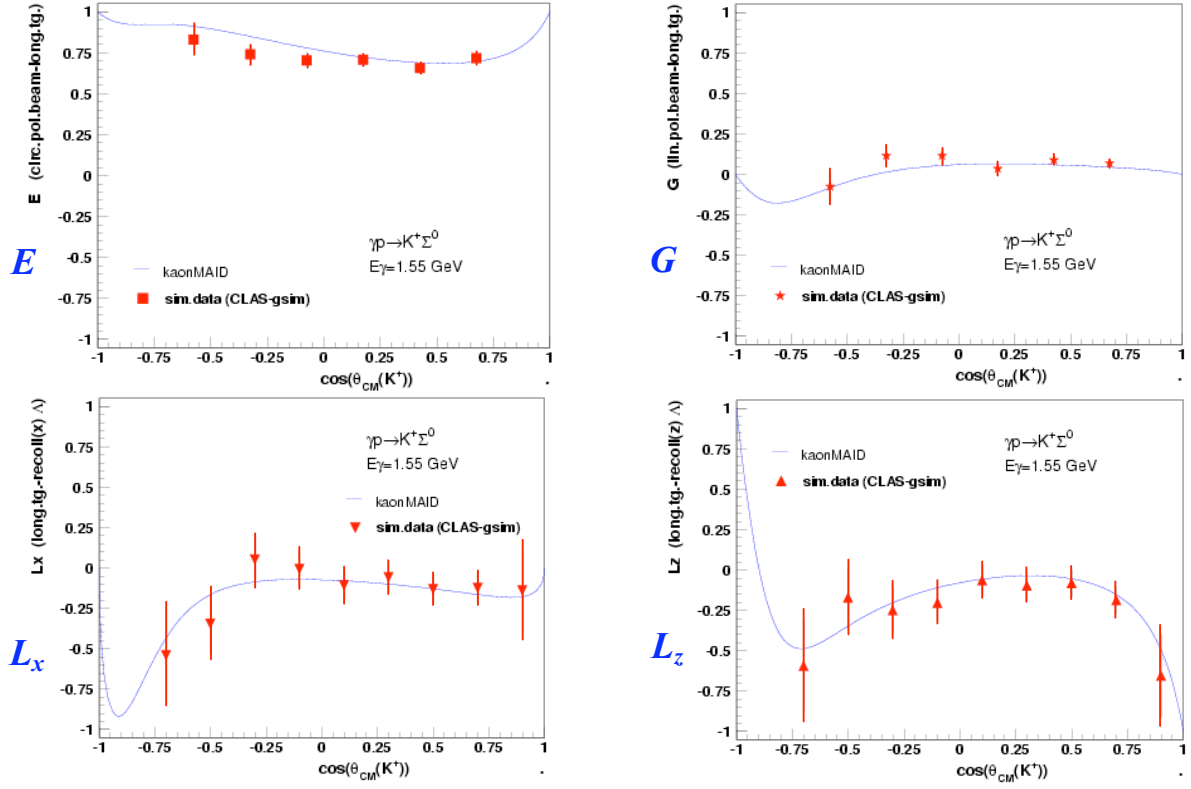


Figure 34. Double-polarization asymmetries for beam-target (E , G), top panels, and target-recoil (L_x , L_z , T_x , T_z), middle and bottom panels, at $E_\gamma = 1.55$ GeV ($W = 1.948$ GeV) for the $\gamma p \rightarrow K^+ \Sigma^0$ reaction.

3 Experimental Parameters

3.1 Target Parameters

We now develop a run plan around the HD frozen-spin target. (Time estimates for a Butanol target are given at the end of this section.) The target cell, filled with 3g of solid HD and 16% aluminum cooling wires (by weight), has a length of 5.0 cm and radius of 1.26 cm. The density of the target material is $\rho = 0.147 \text{ g/cm}^3$. Based on the experience at LEGS and modest improvements described in Appendix A, we anticipate a vector polarization of deuterium of $P_v(D) \sim 40\%$.

A vector polarization of 40% implies an accompanying tensor polarization, $P_T(D)$, of about 12%. Rotating the deuteron spin direction flips the vector polarization ($N_+ - N_-$) but leaves the tensor polarization ($N_{++} + N_{--} - 2N_{00}$) unchanged. We will rotate the deuteron spin direction once per beam energy. In addition, approximately 13% of the running time request will utilize an $\vec{H}\vec{D}$ target with $\sim 75\%$ H polarization but no vector D and, hence, no tensor D polarization. The higher H polarization and the larger acceptance for $\gamma+p$ reactions provides very reasonable uncertainties on asymmetries in this modest running time (Figure 33 and Figure 34). A comparison of deuterium data sets with two different values of $P_T(D)$ will allow us to place limits on the small deuteron tensor observables and apply corrections to the neutron asymmetries, if necessary.

In addition to providing the necessary check on deuteron tensor components, the polarized H runs will allow tests of empirical coplanarity and missing-spectator momentum cuts by comparing *bound-p/free-p* data collected under nearly identical conditions. The largely common systematics that come from using the same target and detector for the \vec{H} and \vec{D} runs will provide data that are locked together and this will provide the most stringent determination of the isospin amplitudes, $A_{K\Lambda}$.

In order to account for the background produced on the aluminum wires inside the target cell (2050 wires of $50\mu\text{m}$ diameter) and the cell walls, we will position an “empty” target cell containing only cooling wires $\sim 5\text{cm}$ downstream of the HD target and separate its contribution by vertex reconstruction. This directly measures the total contribution from unpolarizable

nucleons. The in-beam cryostat will be modified to fit into the CLAS detector. A detailed description of the HD target can be found in Appendix A.

3.2 Photon Beam Parameters

In order to extract double polarization observables involving polarized target and polarized beam, we propose to perform the measurement in separate periods:

- During one run period we will employ circularly polarized photons produced by bremsstrahlung from longitudinally polarized electrons on an amorphous radiator. The polarization is given approximately⁹ by

$$P_{circ} = P_{el} \frac{4x - x^2}{4 - 4x + 3x^2} ,$$

where $x(=E_\gamma/E_0)$ is the ratio of photon energy (E_γ) and electron energy (E_0), and P_{el} is the degree of longitudinal polarization of the incident electrons. The degree of polarization rises with x to $0.996 \cdot P_{el}$ at $x=0.95$. Since $P_{circ}/P_{el} < 60\%$ for $x < 0.5$, it is most efficient to trigger on high energy photons, i.e. the upper part of the tagging hodoscope. CEBAF delivers routinely electron beams with 75—85% longitudinal polarization, depending on beam energy and polarization requirements by the other Halls.

We will use an existing collimator with full aperture 2.6 mm -- positioned 5.8 m from the radiator and 16 m from the target -- to reduce the angular spread, resulting in a beam spot on target of about 10 mm. The collimation reduces the photon flux on the target to 34% for $E_0=1.7$ GeV and to 47% for $E_0=2.6$ GeV.

Photon flux considerations have to account for limits in the tagging rate, accidentals and data acquisition rate. The latter is addressed below in Section 3.4 – Count Rate Estimates. The Hall-B

⁹ A more precise calculation requires angular integration over the collimation aperture.

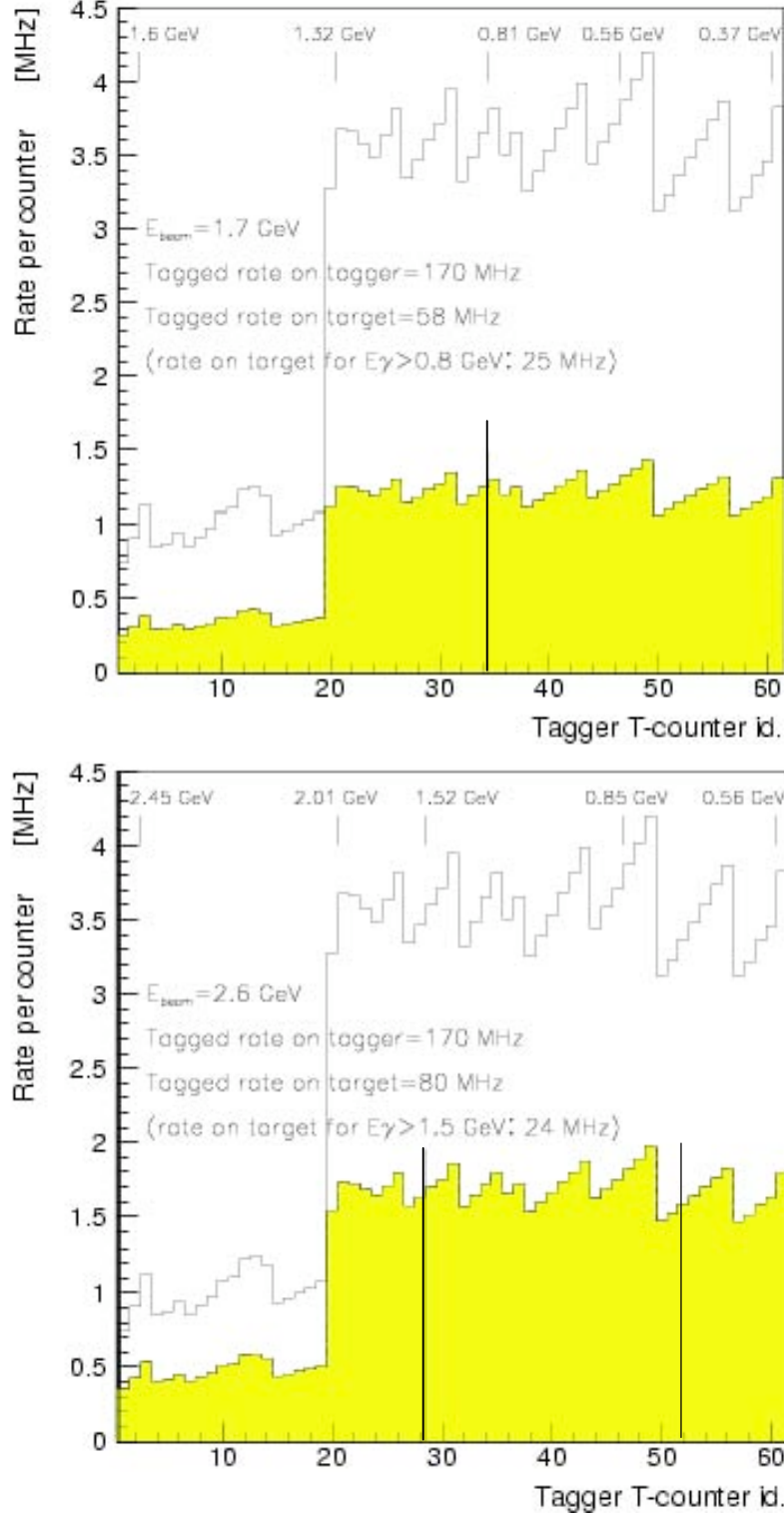


Figure 35. Expected rate on the Hall-B tagger for incoherent bremsstrahlung at $E_0=1.7$ GeV (top) and $E_0=2.6$ GeV (bottom). The filled histogram shows the collimated rate on target. Only data from counters for $E_\gamma > 0.7$ GeV will be used in this experiment. The second vertical line in the lower plot indicates the extended photon energy range for $E_0=2.6$ GeV.

tagger consists of 61 T-counters and 384 E-counters.¹⁰ For a total rate of ~ 170 MHz across the full tagger ($E_\gamma \approx 21-95\%$ of E_0), determined by limiting the count rate in the individual T-counters to about 4 MHz, we have simulated the collimated photon flux on target as shown in Figure 35.

For $E_0=1.7$ GeV and photons tagged between 0.7 GeV and 1.63 GeV (upper 62% of the Hall-B tagging hodoscope) the collimated photon flux is 30 MHz for 87 MHz tagging rate in this energy range with ca. 73% of events having more than one tagged photon from the same or neighboring beam bucket. In the $1.1 < E_\gamma < 1.6$ GeV range used for KY production, the flux on target is 14 MHz.

For $E_0=2.6$ GeV and $1.63 < E_\gamma < 2.47$ GeV (upper 43% of the tagger) the collimated photon flux amounts to 21 MHz for 44 MHz tagging rate with ca. 66% of events having more than one tagged photon from the same or neighboring beam bucket. In order to increase our statistics for photon energies between 0.7 GeV and 1.6 GeV we will use data from both runs for $E_0=1.7$ and 2.6 GeV, the latter with reduced circular polarization.

- During another run period we will use linearly polarized photons produced by coherent bremsstrahlung on a thin diamond crystal. Coherent bremsstrahlung has been successfully employed at Jefferson Lab during the CLAS-g8 run period. The degree of linear polarization for a small photon energy range in the coherent peak depends heavily on the collimation aperture and on the fractional photon energy $x=E_\gamma/E_0$. During CLAS-g8 we achieved ca. 92% polarization at $x=0.3$ and collimation to $\frac{2}{3}$ of a characteristic angle ($\theta_{\text{char}}=m_e c^2/E_0$) using a 50 μm thick diamond and an instrumented collimator with an aperture of 2.0mm. The polarization falls off with increasing photon energy and yields, reaching about 70% at $x=0.5$. The polarization of the collimated beam is fairly constant over a 180-200 MeV energy range near the coherent edge. Due to strong collimation, the photon flux on the target originates largely from an energy range of about 150-200 MeV below the coherent edge and is limited by the high count rate on T-counters in the coherent peak. As shown in Figure 36, for a total tagged rate of 80 MHz, the collimated photon flux on target is about 25 MHz, about 70% of which originates from the

¹⁰ The smaller, partly overlapping scintillators (E-counters) are used to provide a good energy resolution (ca. 0.1% per channel for 767 channels including overlaps), thicker scintillators (T-counters) provide a good timing information ($\sigma \sim 150-180$ psec). The rate limitations for T-counters is about 10-12 MHz (benchmark) and 4-5 MHz for smooth running conditions.

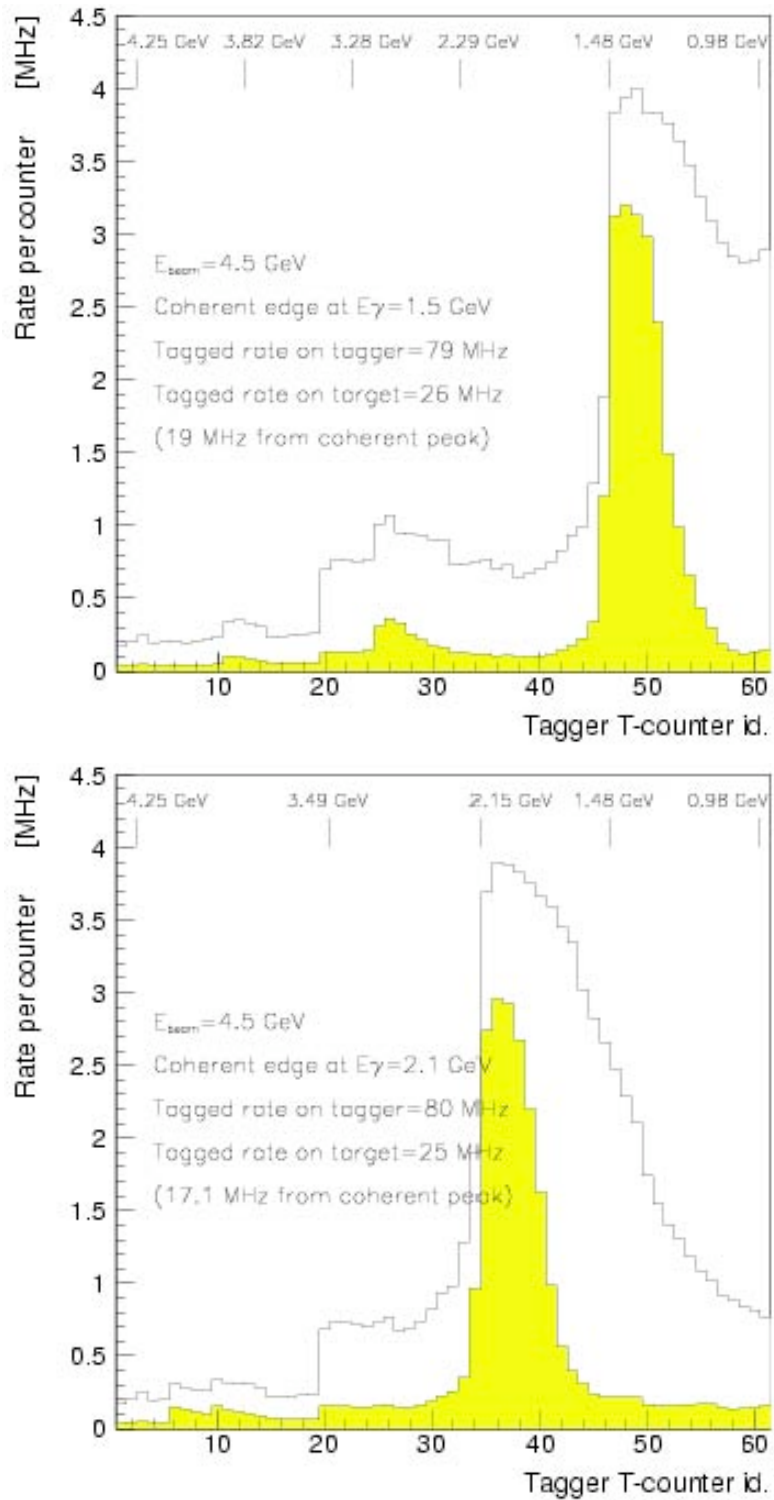


Figure 36. Expected rate on the Hall-B tagger for coherent bremsstrahlung with coherent peak at $E_{\text{coh}} = 1.5$ GeV (left) and $E_{\text{coh}} = 2.1$ GeV (right). The filled histogram shows the rate on target, which is dominated by the rate from the coherent peak -- due to tight collimation.

coherent peak. The maximum T-counter rate under these conditions is about 4 MHz and peaks near the coherent edge.

3.3 Trigger

The trigger for this experiment shall require the detection of at least two charged particles in the CLAS detector. This condition allows for an unambiguous identification of the reaction $\gamma d \rightarrow \pi^+ p$ (p_s). For $\pi^+ \pi^- n$ and $K^+ \Sigma^-$ ($\Sigma^- \rightarrow \pi^- n$), the two charged particles trigger data collection and an off-line coincidence with a neutron is required. For $K^0 \Lambda$ and $K^0 \Sigma^0$, any of the two charged pions from the decay $K_s^0 \rightarrow \pi^+ \pi^-$ and the two charged decay particles from $\Lambda \rightarrow p \pi^-$ can trigger the event, but all four must be present for off-line reconstruction. The detection of the Λ decay particles will provide a measurement of its recoil polarization. Note that the tagger will not be used in the trigger; hits in the tagger hodoscope will be reported by pipeline TDCs. This trigger configuration will not overload the data acquisition system; the expected trigger rate will be below 4 kHz. (An additional one-prong trigger including the Level-2 track segment finder will be prescaled to allow for studies on trigger efficiencies.) As the background simulations have shown, rates in the CLAS detector components will be low with HD (Table 3).

In contrast, a run on deuterated butanol would be severely limited by background rates in drift chambers, start and time-of-flight counters, and in order to keep the d.a.q. rate below 10kHz would require a reduction in the photon flux by a factor of 5-8.

3.4 Count Rate Estimates

We will perform the analyses of pseudoscalar meson photo-production from neutrons over a large energy and angular range in order to determine the energy dependent strengths of various partial waves and to discriminate between various solutions of partial wave and pole fits. The accuracy for single and double polarization observables should be better than about ± 0.15 , at least in the energy range around resonant structures. The strength of the proposed experiment is the large range of different observables that will be measured simultaneously – thus with common systematic uncertainties. Such a survey is more effective in constraining partial wave

analyses than a few observables measured with great accuracy, although the latter are of course also desirable.

The energy range covered with circularly polarized photons produced from polarized electron beams at $E_0=1.7$ GeV and 2.6 GeV is $0.7 \text{ GeV} < E_\gamma < 2.5 \text{ GeV}$, which corresponds to hadronic masses in the γn system of $1.48 \text{ GeV} < W < 2.36 \text{ GeV}$. With eight settings of the coherent peak, the energy range from $0.7 \text{ GeV} < E_\gamma < 2.3 \text{ GeV}$ will be covered with linearly polarized photons.

The count rate estimates for pion as well as kaon production are based on the acceptance calculations determined via Monte Carlo simulations, on the photon flux considerations of Section 3.2, *Photon Beam Parameters*, and on the target density \times length of 0.735 g/cm^2 (with $A_{HD} = 3.024 \text{ g/mol}$). Since the cross sections and the CLAS acceptance for the hyperon production channels are rather small, the beam time request is largely based on sufficient rate in these channels. For the hyperon production channels, we propose to measure the observables in coarse segmentations in E_γ and $\cos\theta_K^*$. The angular range that can be covered in this experiment is limited by the acceptance of CLAS. We propose to collect data in 14 bins in E_γ from 1.1 to 2.5 GeV ($\Delta E_\gamma = 100 \text{ MeV}$) and 6 bins in angle, $-0.7 < \cos(\theta_K^*) < 0.8$ ($\Delta \cos\theta_K^* = 0.25$). For some polarization observables we can obtain finer binning of the production angle with $\Delta \cos\theta_K^* = 0.2$. The acceptance for $K^+\Sigma^-$ below $E_\gamma \sim 1.3 \text{ GeV}$ is too low to measure this reaction at the lowest energies.

The cross sections for the considered hyperon reactions from the neutron are not known. In the absence of data, model predictions for the neutron cross sections cannot be expected to be reliable and in fact vary over an order of magnitude, even for different versions of the same model (see Figure 1). Accordingly, we have assumed that the neutron cross sections are of the same order as similar reactions on the proton. The published differential cross sections for $\gamma p \rightarrow K^+\Lambda$, $K^+\Sigma^0$, $K^0\Sigma^+$ [38,39] are used for detailed error estimates on a bin-by-bin basis, as summarized in Table 5 and Table 6.

A rough estimate for the production rate into 4π from the 5.0cm long HD target is given by

$$N_{\text{evts}} = \sigma \Phi_\gamma \rho_{\text{tg}} l_{\text{tg}} N_A / A_{HD} \approx 3.5 \text{ events/sec for } 1.1 < E_\gamma < 1.6 \text{ GeV}$$

and a photon flux Φ_γ (on target) of 14 MHz in this energy range (as discussed in Section 3.2). Here we use the averaged cross section for $\gamma p \rightarrow K^+ \Lambda$ of $\sigma \approx 1.8 \mu\text{b}^{[8]}$ at center-of-mass energies (W) between 1.7 GeV and 1.9 GeV (cf. Figure 1).

The production rate for the $E_c = 2.6$ GeV run is expected to be slightly less,

$$N_{\text{evts}} = \sigma \Phi_\gamma \rho_{\text{tg}} l_{\text{tg}} N_A / A_{HD} \approx 2.7 \text{ events/sec in } 1.6 < E_\gamma < 2.5 \text{ GeV}$$

for $\Phi_\gamma = 21$ MHz on target in this energy range (Section 3.2). We expect a similar production rate for $K^0 \Sigma^0$ and one fifth of the rate for $\gamma n \rightarrow K^+ \Sigma^-$ based on the cross section ratios in $\gamma p \rightarrow KY$.

For data taken with coherent bremsstrahlung and a collimated photon flux Φ_γ of 16 to 25 MHz in the 200 MeV energy interval of the coherent peak, the expected production rate is about 1.5 to 5 events/sec for both $K^0 \Lambda$ and $K^0 \Sigma^0$ for $E_{\text{coh}} = 2.3$ GeV and $E_{\text{coh}} = 1.3$ GeV, respectively.

Taking into account the low acceptance of CLAS for the considered hyperon reactions (Figure 14), we expect $K^0 \Lambda$ rates of 600 to 900 detected events in each energy bin per day during the runs with circularly polarized photons and 1200 to 2400 detected events in each energy bin per day using linearly polarized photons. Expected detection rates for $K^0 \Sigma^0$ will be about 300 to 800 events/day in each energy bin for circularly polarized and linearly polarized photons. The rate drops to 100 and 350 events/days at 2.2 GeV. The expected $K^+ \Sigma^-$ yield is about 50 to 150 events/day for circular polarized beam and 100 to 420 events/day with linear polarization. A bin-by-bin breakdown of expected statistical errors is given in Table 5 and Table 6 for the run time request discussed in the next section.

Asymmetries for single- and double-polarization observables in pseudoscalar-meson production can be written as,

$$A^{ik} = \frac{f_i f_k}{P_i P_k} \frac{N_+ - N_-}{N_+ + N_-}, \text{ with statistical uncertainty } \delta A^{ik} \cong \frac{f_i f_k}{P_i P_k} \frac{1}{\sqrt{N_+ + N_-}}, \quad (4)$$

where P_i, P_k are either the degree of photon beam polarization, or the self-analyzing power of the recoiling hyperon (α), or the target polarization; the weighting factors (f_i, f_k) account for the additional azimuthal binning required to extract observables involving plane polarized photons ($f_{i,k} = \pi/2$, or decay distributions to extract components of the recoil polarization ($f_{i,k} = 2$); otherwise $f_{i,k} = 1$. The meaning of N_+ and N_- is obvious for single polarization observables, and

$N_+=N^{++}+N^-$, $N_-=N^{+-}+N^{+}$ for double polarization observables in pseudoscalar production, i.e. sums over parallel or antiparallel/perpendicular spin orientations. Note that N^{++} and N^- provide different polarization information for double pion production.

For asymmetry ratios, the statistical error is dominated by the uncertainty on subtracting the yields and can be approximated by the expression in eqn. (4) for large N_- and N_+ . The proposed accuracy of ± 0.15 in single and double-polarization neutron observables requires a large number of events per bin for observables that involve the polarized target. This is summarized in Table 4. Since the analyzing powers for Σ^0 and Σ^- decay¹¹ are much smaller than for Λ , observables involving the recoil polarization will not be measured for $K^0\Sigma^0$ and $K^+\Sigma^-$. Moreover, the required yields of $K^0\Lambda$ events for T_x and T_z , which can be measured with longitudinally polarized target via triple polarization, are about a factor of 4 higher than for L_x and L_z , and will only be extracted with a coarser angular binning, as indicated in Table 5. They nonetheless provide additional constraints on the $K\Lambda$ amplitude and allow cross-checks for systematic variations between observables, via the nonlinear algebraic relations between polarization asymmetries.

Table 4: Required number of events (N_++N_-) per bin in order to achieve an accuracy of ± 0.1 and ± 0.15 for the listed polarization observables in $K^0\Lambda$, with $P_{tgt} = 40\%$, $P_\gamma^{circ} \approx 55-79\%$ or $P_\gamma^{lin} \approx 75-90\%$, and $\alpha_\Lambda=0.64$.

δA	E	Σ	G	P	L_x, L_z	C_x, C_z	$O_x, O_y, -T, O_z$
± 0.1	1000-2100	320-460	5200-7400	1000	6100	1600-3300	3200-4500
± 0.15	450-950	140-200	2300-3300	450	2700	700-1470	1420-2000

¹¹ $\alpha_\Lambda=0.642$, $\alpha_{\Sigma^-}=-0.068$, and $\alpha_{\Sigma^0}=-\alpha_\Lambda/3$ when averaged over the spin orientation of the decay photon.

Table 5. Detailed calculation of the expected accuracy for the requested beam time for $K^0\Lambda$. The number in parentheses denotes the number of angular bins. The entries for the expected accuracy are averaged over all but the most backward angular bin.

E_γ	δE	$\delta \Sigma$	δG	δP	$\delta C_{x'}, \delta C_{z'}$	$\delta L_{x'}, \delta L_{z'}$	$\delta T_{x'}, \delta T_{z'}$	$\delta O_{x'}, \delta O_{z'}$	$\delta O_{y'} (\delta T)$
1.1-1.2	0.08 (6)	0.07 (8)	0.13 (6)	0.06 (8)	0.10 (6)	0.13 (6)	0.16 (4)	0.16 (6)	0.15 (6)
1.2-1.3	0.08 (6)	0.07 (8)	0.13 (6)	0.06 (8)	0.10 (6)	0.12 (6)	0.15 (4)	0.15 (6)	0.15 (6)
1.3-1.4	0.07 (6)	0.05 (8)	0.11 (6)	0.05 (8)	0.09 (6)	0.12 (6)	0.15 (4)	0.15 (6)	0.15 (6)
1.4-1.5	0.07 (6)	0.05 (8)	0.11 (6)	0.05 (8)	0.10 (6)	0.12 (6)	0.15 (4)	0.15 (6)	0.15 (6)
1.5-1.6	0.08 (6)	0.06 (8)	0.11 (6)	0.05 (8)	0.11 (6)	0.13 (6)	0.15 (4)	0.15 (6)	0.15 (6)
1.6-1.7	0.11 (6)	0.06 (8)	0.11 (6)	0.07 (8)	0.14 (6)	0.15 (6)	0.17 (4)	0.15 (6)	0.14 (6)
1.7-1.8	0.10 (6)	0.05 (8)	0.11 (6)	0.06 (8)	0.14 (6)	0.15 (6)	0.17 (4)	0.15 (6)	0.14 (6)
1.8-1.9	0.10 (6)	0.05 (8)	0.11 (6)	0.07 (8)	0.14 (6)	0.14 (6)	0.18 (4)	0.15 (6)	0.15 (6)
1.9-2.0	0.11 (6)	0.05 (8)	0.11 (6)	0.06 (8)	0.13 (6)	0.15 (6)	0.19 (4)	0.15 (6)	0.15 (6)
2.0-2.1	0.11 (6)	0.06 (8)	0.12 (6)	0.06 (8)	0.14 (6)	0.16 (6)	0.23 (4)	0.16 (6)	0.15 (6)
2.2-2.3	0.12 (6)	0.06 (8)	0.12 (6)	0.07 (8)	0.14 (6)	0.16 (6)	0.24 (4)	0.16 (6)	0.15 (6)
2.3-2.47	0.12 (6)	--	--	0.11 (8)	0.15 (6)	0.25 (6)	0.36 (4)	--	--

Table 6. Detailed calculation of the expected accuracy for the requested beam time for $K^0\Sigma^0$ and $K^+\Sigma^-$. The number in parentheses denotes the number of angular bins. The entries for the expected accuracy are averaged over all but the most backward angular bin.

E_γ -bin	$K^0\Sigma^0$: δE	$K^0\Sigma^0$: $\delta \Sigma$	$K^0\Sigma^0$: δG	$K^0\Sigma^0$: δP	$K^+\Sigma^-$: δE	$K^+\Sigma^-$: $\delta \Sigma$	$K^+\Sigma^-$: δG
1.1-1.2	0.15 (4)	0.13 (6)	0.22 (4)	0.27 (4)	0.32 (4)	0.21 (4)	0.40 (4)
1.2-1.3	0.16 (6)	0.11 (6)	0.19 (4)	0.23 (4)	0.24 (4)	0.17 (4)	0.35 (4)
1.3-1.4	0.12 (6)	0.09 (6)	0.18 (4)	0.17 (4)	0.18 (4)	0.17 (6)	0.24 (4)
1.4-1.5	0.11 (6)	0.08 (6)	0.17 (6)	0.17 (4)	0.17 (4)	0.16 (6)	0.24 (4)
1.5-1.6	0.10 (6)	0.08 (6)	0.17 (6)	0.17 (4)	0.16 (4)	0.12 (6)	0.18 (4)
1.6-1.7	0.15 (4)	0.10 (6)	0.18 (4)	0.22 (4)	0.17 (4)	0.12 (6)	0.17 (4)
1.7-1.8	0.14 (4)	0.10 (6)	0.17 (4)	0.21 (4)	0.16 (4)	0.11 (6)	0.16 (4)
1.8-1.9	0.19 (4)	0.11 (6)	0.18 (4)	0.27 (4)	0.15 (4)	0.11 (6)	0.15 (4)
1.9-2.0	0.19 (4)	0.10 (6)	0.17 (4)	0.28 (4)	0.14 (4)	0.10 (6)	0.14 (4)
2.0-2.1	0.20 (4)	0.11 (6)	0.18 (4)	0.29 (4)	0.15 (4)	0.10 (6)	0.14 (4)
2.1-2.2	0.21 (4)	0.12 (6)	0.21 (4)	0.29 (4)	0.14 (4)	0.10 (6)	0.14 (4)
2.2-2.3	0.23 (4)	0.14 (6)	0.22 (4)	0.30 (4)	0.14 (4)	0.10 (6)	0.14 (4)
2.3-2.47	0.22 (4)	--	--	0.34 (4)	0.12 (4)	--	--

Due to the smaller cross sections, a coarse angular binning must be used with the $K^+\Sigma^-$ asymmetries (Table 6). Nonetheless, the asymmetries provide a useful cross-check. Note that, just as in $\gamma N \rightarrow \pi N$ where measurements of three charge channels determine the three isospin amplitudes which then determine the forth charge channel, eqn 1 in Section 1, here measurements of $K^0\Sigma^0$ together with $K^+\Sigma^0$ and $K^0\Sigma^+$ from the proton should determine the three $A_{K\Sigma}$ amplitudes, from which $K^+\Sigma^-$ can be calculated. Since the $K\Sigma$ amplitude will not be over-determined in the foreseeable future, $K^+\Sigma^-$ asymmetries can provide constraints on models, even when the errors are far from negligible.

Since in developing the $\gamma+n$ reaction rate estimates we have assumed equal photo-production cross sections from neutrons and protons, the production rates during the polarized hydrogen runs are the same as in the discussion above. However, due to an almost order of magnitude larger acceptance for $\gamma+p$ reactions (Figure 32-right-panel vs Figure 14-left-panel) and nearly a factor of two higher polarization in $\vec{H} \cdot \vec{D}$ vs $H \cdot \vec{D}$ runs, the expected detection rates for polarized hydrogen running are much higher. The polarized hydrogen running must provide asymmetries that can be comparison to the polarized deuterium data in order to evaluate and

Table 7. Expected accuracy for the requested beam time on polarized H for $K^+\Lambda$, $K^+\Sigma^0$, $K^0\Sigma^+$. The number in parentheses denotes the number of angular bins. The entries for the expected accuracy are averaged over all but the most forward and backward angular bin. Entries for $\gamma p \rightarrow K^0\Sigma^+$ are for 200 MeV wide energy bins.

E_γ -bin (GeV)	$K^+\Lambda$: δE	$K^+\Lambda$: δG	$K^+\Lambda$: $\delta L_{x',z'}$	$K^+\Lambda$: $\delta T_{x',z'}$	$K^+\Sigma^0$: δE	$K^+\Sigma^0$: δG	$K^0\Sigma^+$: δE	$K^0\Sigma^+$: δG
1.1-1.2	0.07 (9)	0.07 (9)	0.09 (9)	0.13 (6)	0.12 (6)	0.09 (6)	--	--
1.2-1.3	0.06 (9)	0.07 (9)	0.08 (9)	0.13 (6)	0.08 (6)	0.08 (6)	--	--
1.3-1.4	0.05 (9)	0.06 (9)	0.08 (9)	0.12 (6)	0.07 (6)	0.06 (6)	0.12 (4)	0.11 (4)
1.4-1.5	0.05 (9)	0.06 (9)	0.07 (9)	0.11 (6)	0.06 (6)	0.06 (6)		
1.5-1.6	0.05 (9)	0.06 (9)	0.07 (9)	0.11 (6)	0.05 (6)	0.06 (6)	0.13 (4)	0.12 (4)
1.6-1.7	0.05 (9)	0.06 (9)	0.08 (9)	0.12 (6)	0.05 (6)	0.06 (6)		
1.7-1.8	0.06 (9)	0.07 (9)	0.09 (9)	0.13 (6)	0.05 (6)	0.06 (6)	0.14 (4)	0.15 (4)
1.8-1.9	0.07 (9)	0.08 (9)	0.10 (9)	0.11 (4)	0.06 (6)	0.07 (6)		
1.9-2.0	0.07 (9)	0.08 (9)	0.11 (9)	0.12 (4)	0.06 (6)	0.07 (6)	0.17 (4)	0.19 (4)
2.0-2.1	0.08 (9)	0.10 (9)	0.12 (9)	0.12 (4)	0.06 (6)	0.07 (6)		
2.1-2.2	0.09 (9)	0.11 (9)	0.10 (6)	0.13 (4)	0.06 (6)	0.08 (6)	0.23 (4)	0.24 (4)
2.2-2.3	0.11 (9)	0.12 (9)	0.11 (6)	0.13 (4)	0.07 (6)	0.09 (6)		
2.3-2.47	0.	--	--	--	0.07 (6)	--	--	--

adjust, as needed, the coplanarity cuts in isolating *quasifree*-neutrons. This requires a smaller error on the $\gamma+p$ asymmetries so that the uncertainty on the difference between $\gamma+n$ and $\gamma+p$ asymmetries is meaningful. Since the uncertainty goal for the average $\gamma+n$ asymmetry is ± 0.15 , we require that the uncertainty on the average $\gamma+p$ asymmetry be ± 0.10 so that the error on their difference will be held to about ± 0.18 . A bin-by-bin breakdown of the expected statistical uncertainties on the $\gamma+p$ asymmetries is given in Table 7.

Running with $\vec{H} \cdot \vec{D}$ will also be used to collect neutron data with no D tensor polarization. This can be used to investigate the possible contamination by deuteron tensor observables of those neutron asymmetries that have a similar angular dependence (eg. T_{20}^L vs Σ in eqn 2.1), but are target-polarization independent and not isolated by rotating the deuteron spin direction during the $H \cdot \vec{D}$ runs. Deuteron tensor observables cannot have a rapid energy dependence, so that a consistent signal over several bins would be required before applying any corrections. Target-independent asymmetries (such as Σ) are measured with smaller statistical errors (± 0.05 average for Σ in $\gamma+n \rightarrow K^0 \Lambda$ - Table 5), so that one can tolerate about 8 times less $\vec{H} \cdot \vec{D}$ data before the error on such a corrected $\gamma+n$ asymmetry exceeded the ± 0.15 goal for the $K^0 \Lambda$ channel. (This reduction in running time is compatible with the required accuracy on the $\gamma+p$ asymmetries.) Nonetheless, deuteron tensor observables cannot have a rapid energy dependence, so that a consistent signal over several bins would be required before applying any corrections.

3.5 Beam Time Requirements for KY Channels

The beam time request is determined by the goal of achieving average uncertainties of at least ± 0.15 in the full suite of $K^0 \Lambda$ asymmetries (Table 5) in order to provide an over-determination of the production amplitude. The counting rates for single-pion and double-pion photo-production are significantly higher, due to larger cross sections and the significantly larger acceptances that result from having to detect fewer particles in the final states. Simulations for these channels are described in subsequent sections.

The beam time request for $\vec{H} \cdot \vec{D}$ running is determined by the goal of achieving average uncertainties of at least ± 0.10 in the $K^+ \Lambda$ asymmetries (Table 7) in order to provide meaningful

evaluations of possible corrections to $\gamma+n$ observables. The same data will be used for similar tests of $\pi^+\pi^-n$ and π^-p asymmetries, but the rates in these channels are much higher and the statistical uncertainties are correspondingly smaller.

- Circularly polarized photons from bremsstrahlung of polarized electrons ($P_{el} \approx 80\%$):

We plan to collect data over photon energies between 0.7 GeV and 2.5 GeV ($1.48 < W < 2.35$ GeV). In order to achieve reasonably high degrees of photon polarization we request two different beam energy settings: a lower energy run ($E_0 = 1.7$ GeV) to cover the energy range $0.7 < E_\gamma < 1.6$ GeV and another run at a beam energy of 2.6 GeV to cover the higher energies up to 2.5 GeV. During the higher energy run we will take data for lower energies as well – however with lower photon polarization.

For the hyperon production channels we will cover the energy range $1.1 < E_\gamma < 1.6$ GeV and a $\cos\theta^*_K$ range from -0.7 to 0.8 during the lower energy run. In order to achieve an average accuracy for the three polarization observables E , C_x , and C_z , of about ± 0.15 in 5 E_γ bins and 6 $\cos\theta^*_K$ bins for $\gamma n \rightarrow K^0 \Lambda$ and $K^0 \Sigma^0$, we request **11 days** of data taking at $E_0 = 1.7$ GeV. The average expected accuracy for the observable E in $K^+\Sigma^-$ production for this beam time will be about ± 0.17 for 4 bins in $\cos\theta^*_K$.

During the higher energy run we will cover additionally the energy range $1.6 < E_\gamma < 2.5$ GeV. For the hyperon production channels we will cover the $\cos\theta^*_K$ range from -0.7 to 0.8. In order to achieve an average accuracy for the observables E , C_x , and C_z , of about ± 0.15 in 9 additional bins in E_γ and 6 bins in $\cos\theta^*_K$ for $\gamma n \rightarrow K^0 \Lambda$ and $K^0 \Sigma^0$, we request **14 days** of data taking at $E_0 = 2.6$ GeV. The expected accuracy for the observable E in $K^+\Sigma^-$ production for this beam time will be about ± 0.15 for 4 bins in $\cos\theta^*_K$.

The additional run time request for polarized H is **0+2 days**. Cross sections are smallest at the higher energies so that 2 days are needed at $E_0 = 2.6$ GeV; however, the accompanying higher yields at lower energies result in adequate uncertainties despite the lower beam polarization (45% at 1.15 GeV). Thus, additional running at $E_0 = 1.7$ GeV is not requested. This run allows a test of the effectiveness of coplanarity cuts in extracting *free* neutrons by comparing *free* and *bound* proton targets, as well as providing an estimate of deuteron tensor observables. The additional hydrogen runs will also provide a set of data for both isospin channels with largely common systematics associated with the same target and detector.

Thus, the **total request with circular polarization is $11 + 14 + 2 = 27$ days**. The expected errors in the KY channels are shown in Figure 24 –through- Figure 34 for a sample of energies. A bin-by-bin listing of expected errors is given in Table 5, Table 6 and Table 7.

- Linearly polarized photons from coherent bremsstrahlung:

We propose to use electron beam energies of 3.0, 4.5 and 5.5 GeV to produce photons with linear polarizations above 79% at photon energies below 2.3 GeV. In order to cover the photon energy range between 0.7 and 2.3 GeV, we need 8 settings of the coherent peak.

In order to achieve an average accuracy of better than ± 0.15 for the observables G , O_x , T , O_z , L_x , L_z in $K^0\Lambda$ and an accuracy of $\delta G < \pm 0.2$ in $K^0\Sigma^0$, we request **44 days** of data taking above 1.1 GeV; **6 additional days** are requested to cover the energy range between 0.7 and 1.1 GeV for the pion channels. The expected accuracy corresponds to the error bars shown in Figs. 16 to 18.

The additional running with polarized H to verify the effectiveness of coplanarity cuts, estimate the contributions of deuteron tensor observables and provide polarized hydrogen data with the same systematic uncertainties is 1 day per setting, or **8 days**.

Thus, the **total request with linear polarization is $44 + 6 + 8 = 58$ days**. The expected errors in the KY channels are shown in Figure 24-through- Figure 34 for a sample of energies. A bin-by-bin listing of expected errors is given in Table 5, Table 6 and Table 7.

- Estimated run times with deuterated Butanol:

Our simulations have shown that for data taking on a deuterated-butanol target we would need much longer beam times in order to perform an analysis of $\gamma n \rightarrow K^0\Lambda$ with comparable accuracy. The chief differences are as follows:

- (a) Tighter cuts in the invariant mass distribution $M(\pi^+\pi^-)$ ($\approx 7\%$ loss) and the relative azimuthal angle of the K^0 and $\pi^+\pi^-$ systems ($\approx 25\%$ loss) improve the signal to background ratio to about 3:1 but reduce the $K^0\Lambda$ yield by about 40%, as shown in Figure 23, which translates into doubling of the beam time. Note that the tight cuts reduce the $K^0\Sigma^0$ yield by 70% making an analysis of this channel practically impossible, and the $K^+\Sigma^-$ channel would be out of the question.

(b) The statistical error is dominated by background subtraction to about 80%. The signal to background ratio is quite poor for Kaon reactions due to increased $\pi^+\pi^-$ background under the K^0 signal and misidentified π^+ around the K^+ mass. Thus with butanol, in order to achieve the same accuracy, the numbers of events per bin listed in Table 4 would have to be multiplied by 14-16.

(c) With a polarization of 40% for HD target, compared to 65% for trityl-doped deuterated butanol, measurements on an HD target require a factor of 2.6 more beam time.

(d) Additionally, the photon flux has to be reduced by roughly a factor of 5-8 in order to keep the trigger rate and detector occupancies acceptable (Table 3).

Thus on average, deuterated-butanol running would require increased running times by a factor of $2 \times 15 \times (1/2.6) \times (5-8) = 55$ –to- 90. Approximate times for the different settings are included in the summary table below. Because of these large factors, our running time requests are based on the use of polarized HD.

- Total run time requirement:

The required run time with an HD target is shown in columns 6 and 7 of Table 8 for the 10 required settings. (For comparison, the approximate time needed to achieve comparable accuracy with a deuterated-butanol target is given in the last column.)

Table 8. Summary of Run time requirements with an HD target (columns 6 and 7), together with estimates for the running time required to achieve a comparable accuracy with deuterated-butanol (last column).

Setting	E_0 (GeV)	P_{el}	E_γ (GeV)	P_γ	Requested Beam time with $H\bar{D}$ (-1500 A)	Requested Beam time with $\bar{H}D$ (+1500 A)	Comparable Beam time With C_4D_9OD (-1500A)
Circ.pol	1.7	80%	0.7-1.6	41-79%	11 days	0 days	~600 days
	2.6	80%	1.5-2.47	58-79%	14 days	2 days	~700 days
Lin.pol.	3.0	-	0.7-0.9	89%	3 days	1 day	~110 days
	3.0	-	0.9-1.1	85%	3 days	1 day	~110 days
	4.5	-	1.1-1.3	90%	7 days	1 day	~260 days
	4.5	-	1.3-1.5	87%	7 days	1 day	~260 days
	5.5	-	1.5-1.7	88%	7 days	1 day	~260 days
	5.5	-	1.7-1.9	85%	7 days	1 day	~260 days
	5.5	-	1.9-2.1	82%	8 days	1 day	~285 days
	5.5	-	2.1-2.3	79%	8 days	1 day	~285 days

4 Simulations of $\gamma n \rightarrow \pi^+ \pi^- n$

The $\gamma n(p) \rightarrow \pi^+ \pi^- n(p)$ channel will be identified by tracking the two charged pions in the CLAS drift chambers and detecting the neutron in the forward electromagnetic calorimeter (EC) or the plastic scintillation counters (SC). Cross sections for this reaction are about 30 times larger than the KY channels, which define the running plan.

Events were generated with a code implementing the model calculation of A. Fix and H. Arenhövel^[24]. As an example, cross sections for $W = 1700$ MeV are shown in the left panel of Figure 37. An intermediate Δ^+ appears as a prominent peak in the invariant mass. Momentum-dependent neutron efficiencies were taken from CLAS Note 2001-006. The combined CLAS acceptance and net efficiency is shown in the right panel of Figure 37.

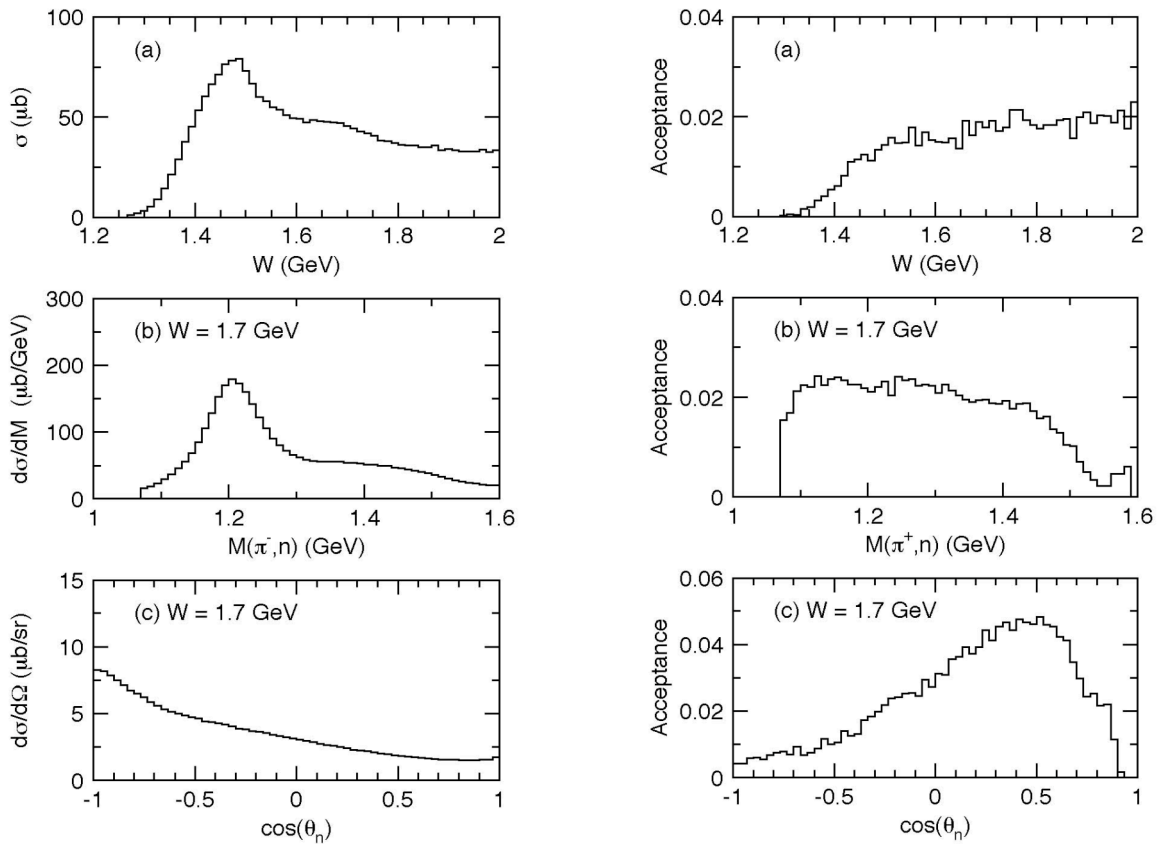


Figure 37. Cross sections for $\gamma n \rightarrow \pi^+ \pi^- n$ calculated from the model of [24] for $W = 1700$ MeV – left panel; product of CLAS acceptance and efficiency – right panel.

Fermi motion for the neutron has been simulated using a spectral function for the deuteron which was fitted to $D(e, e'p)$. With a $\pi^+ \pi^-$ and n detected in CLAS, the distributions of missing mass squared, calculated for the $\gamma n \rightarrow \pi^+ \pi^- n$ reaction are shown in panels (a) and (c) of Figure 38. Fermi motion of the neutron in deuterium has been included in (a). This is very similar to the

result without Fermi broadening in (c), mainly because of the poor neutron momentum resolution. An example of the separation from background events is shown in the right panels of Figure 38. There, $\gamma n \rightarrow \pi^0 \pi^+ \pi^- n$ events were generated and π^+ , π^- and n detected in CLAS. Fermi motion broadens the spectrum in panel (b), but the contribution of the tail of this peak in the region of zero is quite small, allowing an extraction of the $\pi^+ \pi^- n$ channel of interest.

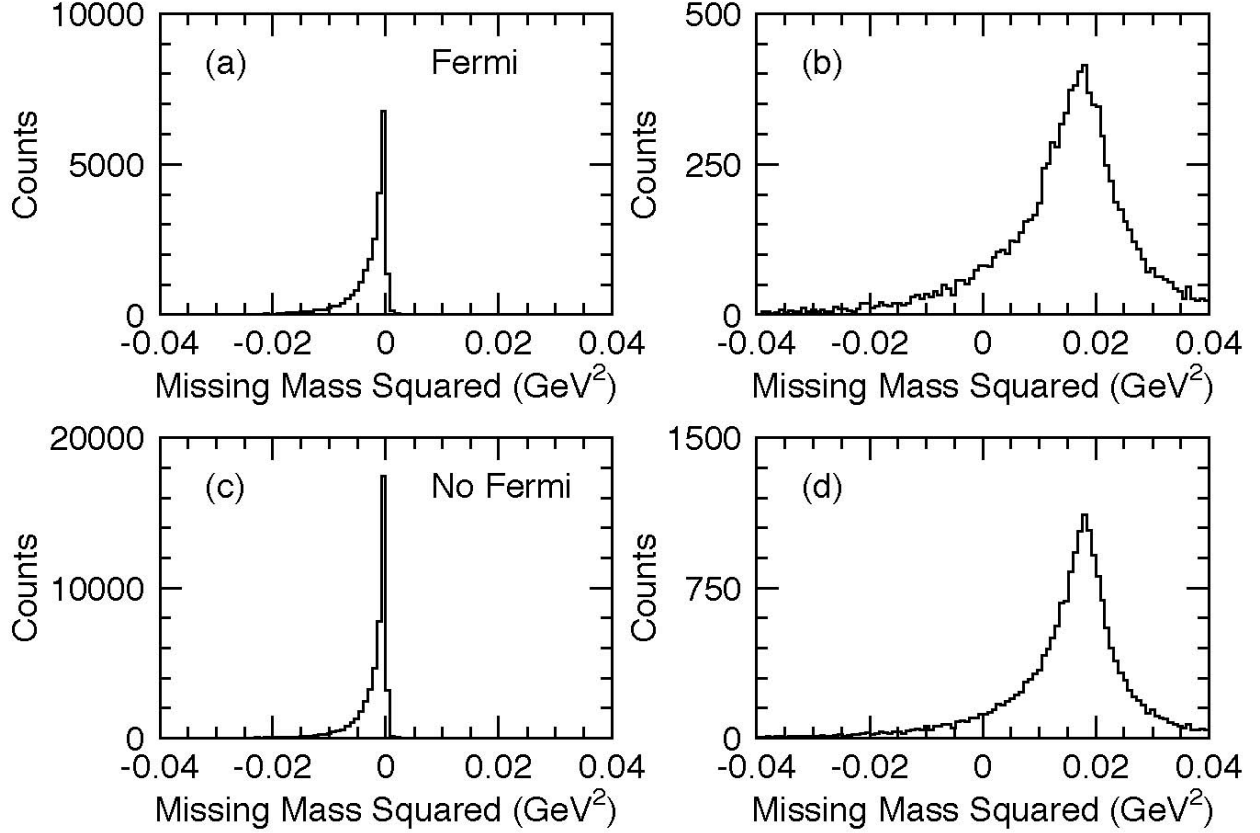


Figure 38. The missing mass $MM^2(X)$ constructed following $\pi^+ \pi^-$ and n detection in the CLAS for the reaction $\gamma n \rightarrow \pi^+ \pi^- n$ (left panels) and for $\gamma n \rightarrow \pi^0 \pi^+ \pi^- n$ (right panels). Fermi motion of the neutron in deuterium has been included in the top two panels.

Assuming the running periods summarized in Table 8 and the efficiencies shown in the right hand panels of Figure 37 for reconstructing $\pi^+ \pi^- n$ events in the CLAS, the estimated uncertainties in beam-target polarization asymmetries are shown in Figure 39 for 50 MeV E_γ bins (~ 28 MeV W bins) centered on $W = 1520$ MeV (left panels) and $W = 1700$ MeV (right panels). Two asymmetries are shown here, P_z^o and P_z^s , which are the 2π analogs of the E and G asymmetries of single-meson production. The errors are clearly sufficient to add a significant new constraint on the s and d-wave components in $D_{13}(1520) \rightarrow \pi\Delta$ and to impact the debate on the relative sign of the $F_{15}(1680) \rightarrow \pi\Delta$ amplitude. Comparable quality data will also be obtained throughout the energy range above $W = 1.6$ GeV with $E_\gamma = 50$ MeV binning, and also with somewhat increased uncertainties for $W < 1.6$ GeV.

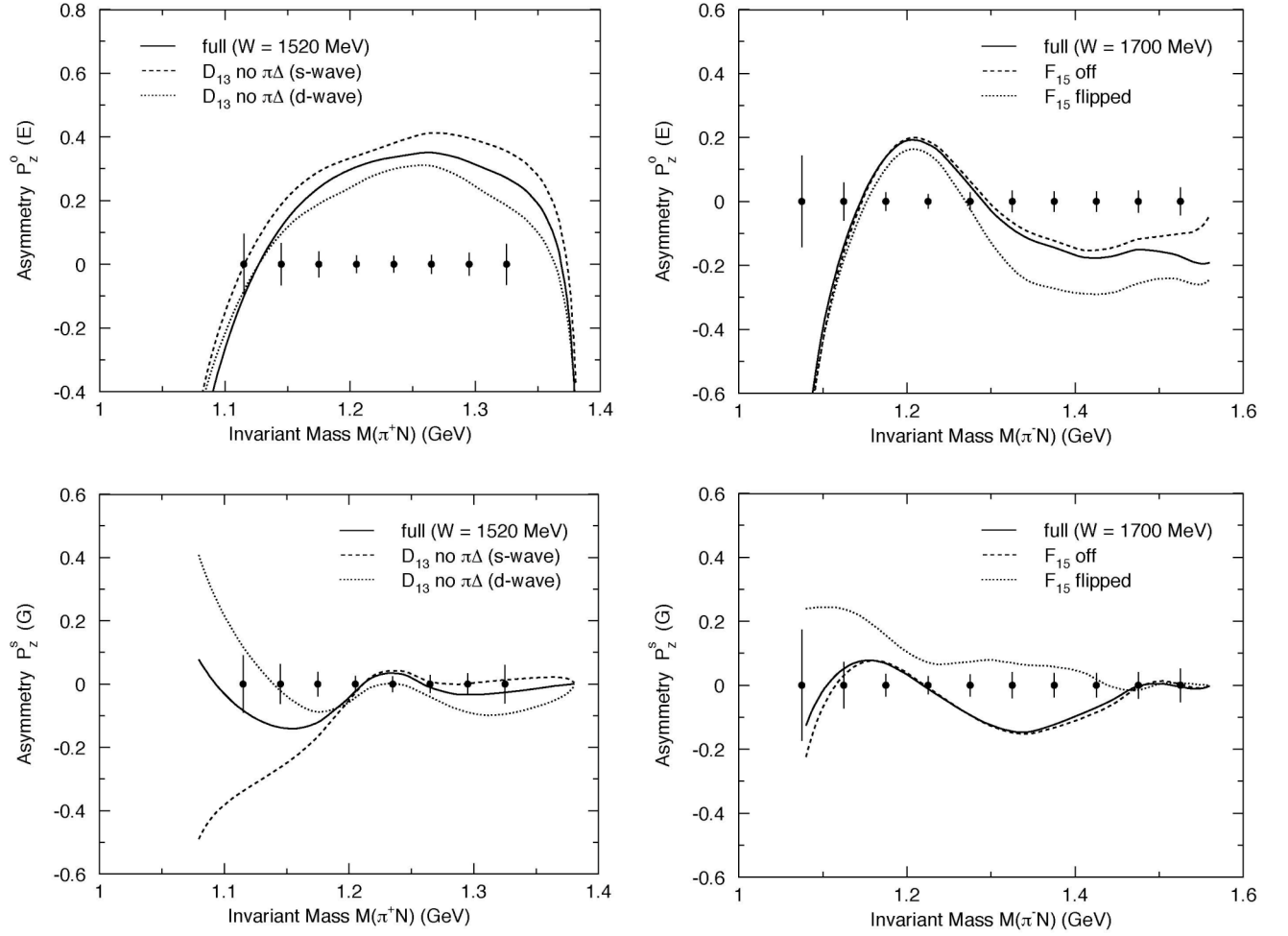


Figure 39. Simulated uncertainties for the “E” and “G” beam-target polarization observables at $W=1520$ MeV (left panels) and at $W=1700$ MeV (right panels). The calculations in the left panel include different $D_{13}(1520) \rightarrow \pi\Delta$ multipole components. The dotted curves in the right panels reflect an alternate choice for the debated sign of the $F_{15}(1680) \rightarrow \pi\Delta$ amplitude.

5 Simulations of $\gamma n \rightarrow \pi^- p$

The $\gamma n (p) \rightarrow \pi^- p (p)$ channel will be identified by tracking the charged pion and the proton in the CLAS drift chambers. Events were distributed in CLAS using the SAID PWA solution as a generator. The simulated acceptance with a torus setting of $I = -1500\text{A}$ is shown in Figure 40 for photon energies up to 1.6 GeV and in Figure 41 for beam energies from 1.6 to 2.5 GeV.

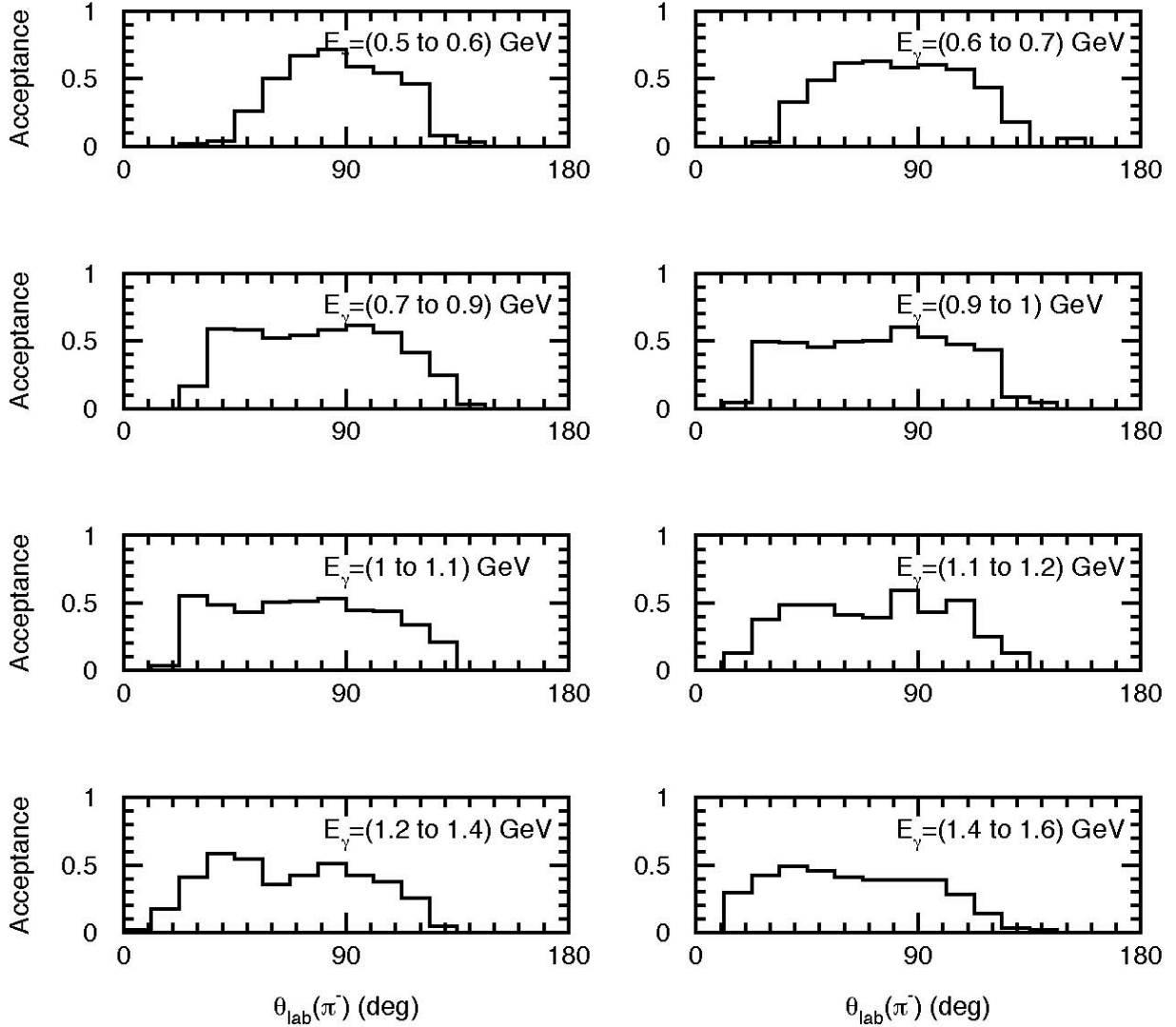


Figure 40. Acceptance for the $\gamma n \rightarrow \pi^- p$ channel for $I = -1500\text{A}$ and beam energies from 0.5 to 1.6 GeV.

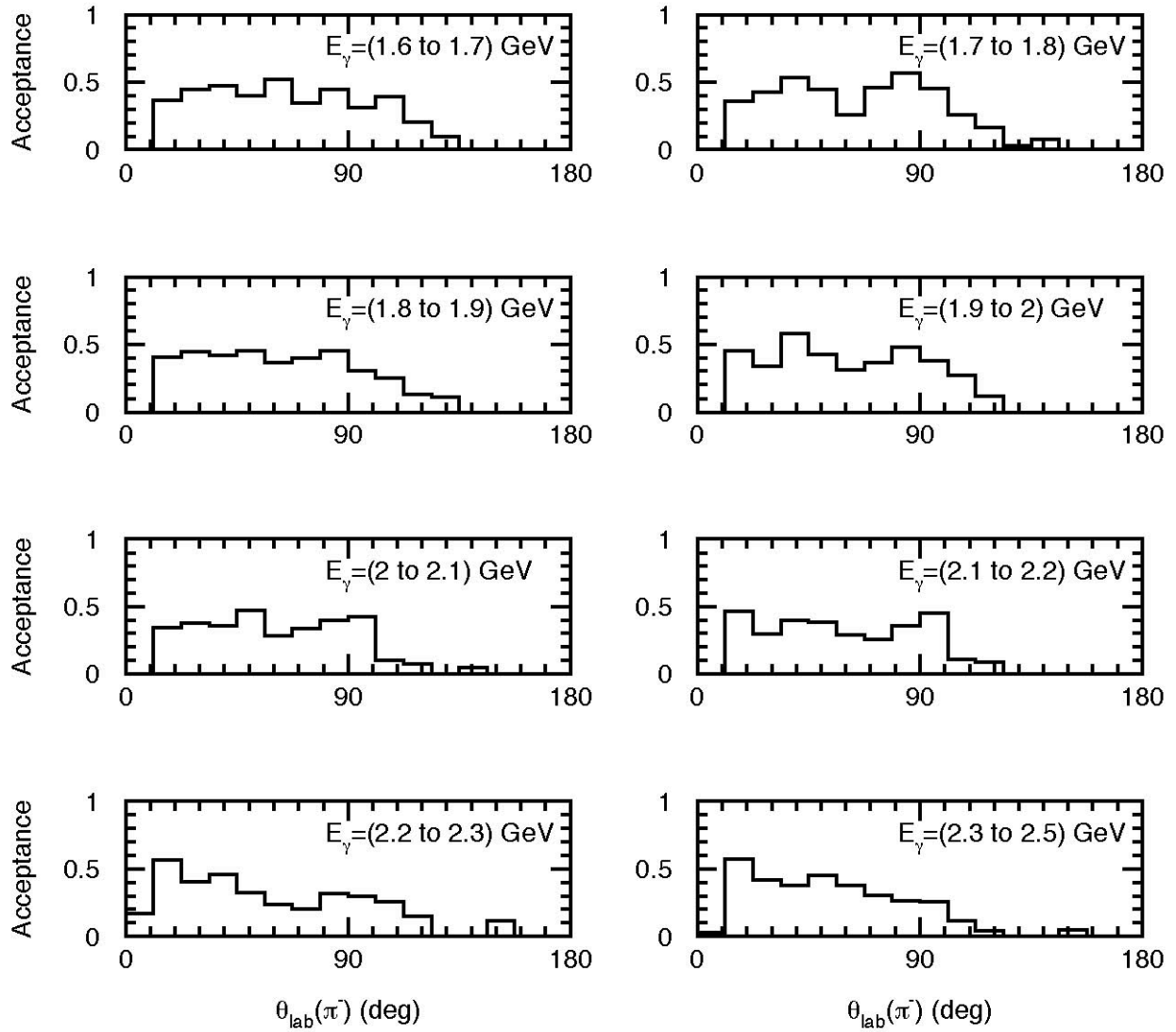


Figure 41. Acceptance for the $\gamma \rightarrow \pi^- p$ channel for $I = -1500\text{A}$ and beam energies from 1.6 to 2.5 GeV.

The acceptance is quite large and the data can be binned as finely as 20 MeV if necessary. Assuming the run plan outlined in Table 8, the projected errors in 20 MeV bins centered on $E_\gamma = 0.8, 1.2, 1.6$ and 2.0 GeV are plotted in Figure 42. Such data will remove the ambiguities evident here (Figure 2) and have a very significant impact on the π -production amplitude.

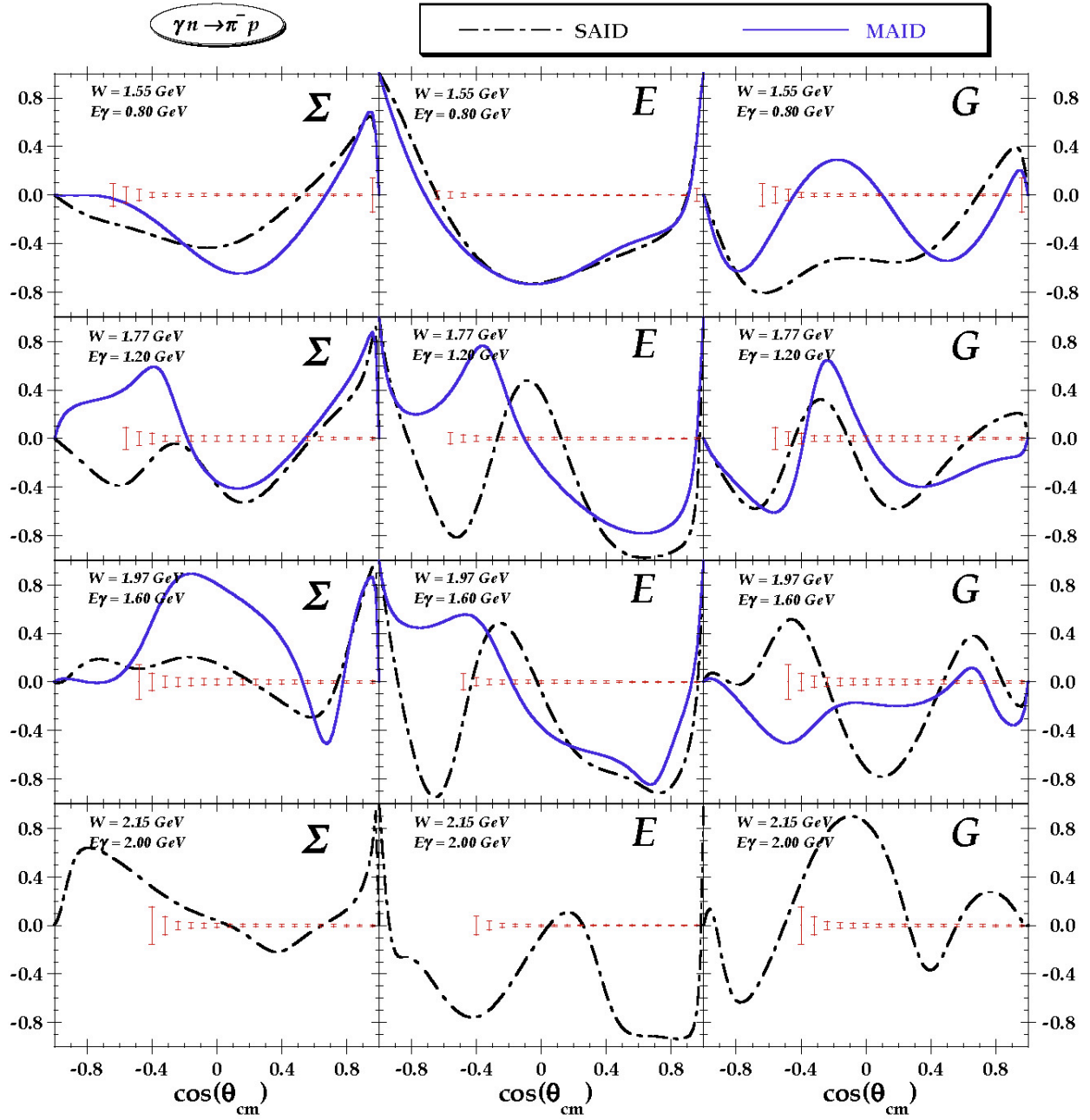


Figure 42. Projected errors (in red) in the $\gamma n \rightarrow \pi^- p$ channel for the beam asymmetry, Σ , and the beam-target asymmetries E and G , in 20 MeV bins centered at 0.8 GeV (top row), 1.2 GeV (2nd row), 1.6 GeV (3rd row) and 2.0 GeV (bottom row).

6 Discussion of systematic uncertainties

We estimate the systematic uncertainties for this experiment of the order of 4-10%, depending on the observable being considered. Obviously, for observables that do not depend on recoil polarization, the uncertainties listed under item (g) do not apply. A table at the end of the detailed list summarizes the different sources.

a) The uncertainty in determining the target polarization is discussed in Section A.4 of the Appendix and summarized in Table A.2: $\delta P(H) \approx 3.7\%$, $\delta P(D) \approx 4.2\%$. Tensor observables which have the same angular dependence as a vector-target polarization asymmetry (T_{20}^0 in eqn 2.1) will be separated by adiabatically reversing the holding field, thus flipping P_D^V but not P_D^T . We expect that the remaining systematic error on such vector-target asymmetries will be negligible. Possible corrections due to tensor observables which have the same angular dependence as target-independent nucleon asymmetries (T_{20}^L in eqn 2.1) will be estimated from the $\vec{H} \cdot \vec{D}$ data. Such corrections depend on the deuteron tensor polarization during the $H \cdot \vec{D}$ running period. The ratio of tensor/vector polarizations is fixed (eqn a2 of Appendix A), so that there are no additional systematic uncertainties involved.

b) Photon beam polarization:

- Circularly polarized photons: The longitudinal polarization of the CEBAF beam is typically changed pseudo-randomly with 60Hz. The beam polarization is measured by means of a Møller Polarimeter; typical uncertainties of these measurements are about 2%. We propose to measure it once per day. Beam charge asymmetry is monitored by means of a Synchrotron Light Monitor and is typically less than 0.2%.
- Linearly polarized photons: Energy and position stability of the coherent peak is continuously monitored by means of deadtime-less tagger scalers. Variations of the photon beam position are monitored by the four scintillators of the instrumented collimator and are typically of order $\sim 50\text{-}100\mu\text{m}^{12}$, which does not result in distortion of the collimated photon beam. In order to minimize false asymmetries due to changes in

¹² This reflects the typical position stability of the electron beam. Data taken during unstable beam conditions (ca. 60-90sec after beam trips) will not be reconstructed.

the detector performance, we change the polarization orientation every run in the cycle: -45° , 45° , -30° , 60° , 0° , 90° with respect to the horizontal. The main factor of uncertainty is the determination of the degree of polarization. Tagger-scaler readouts are inserted into the data stream every 4 sec, providing an ungated and gated photon spectrum, which is analyzed and compared to calculations that describe very accurately all contributing affects in coherent and incoherent bremsstrahlung (anb code)^[40]. From experience during the CLAS-g8 running period and experiments in Mainz we estimate the error to about 4% (absolute). Checks of the calculated degree of polarization will be obtained once per energy bite via direct measurement with a pair polarimeter, which will require special short runs.

- c) Detector performance: Stability of the response of all detector components is important to evade false asymmetries. Changes in the response of CLAS can usually be accounted for by modifications of calibration constants. However, short time variations may distort the asymmetry measurements, especially for runs with linearly polarized photons, since the angular distributions include $\cos 2\Phi$ and $\sin 2\Phi$ terms, which are difficult to disentangle if the asymmetries are small. Moreover, the orientation of the photon polarization cannot continuously be changed. Special attention will be given to these issues with an estimated error of 2-3%.
- d) Reaction identification and background subtraction: The Monte Carlo simulations have shown that extracted yield depends strongly on the cuts for small numbers of considered events and large background, esp. for K^0 events at backward angles. For these cases we estimate the systematic uncertainty at 5-6%, in general, however, the dependence from (small) variations of cut values was much smaller (ca. 2-3%). Data from target background (cooling wires and cell walls) is simultaneously taken with the production data and is subtracted on a bin-by-bin basis. Acceptance differences between the HD target and downstream "empty" target, separated by 5cm, is minimal except for the very forward direction ($\theta_{lab} < 15^\circ$). We estimate a systematic error of 1% for this subtraction procedure, which is negligible compared to the uncertainties of other background.
- e) Separation of quasi-free production: Additional beam time is requested to study the relation between production on free protons (on \vec{HD}) and on bound protons (on $H\vec{D}$) expecting that

the relation is very similar for production on free and bound neutrons. Thus, the reaction dynamical approach to identify the free neutron amplitudes will be tested on proton data. At this point we can only provide an educated guess for this systematic uncertainty (about 3-5%).

- f) Additional uncertainties for cross section measurements: photon flux normalization (ca. 3-4%), target length (2%), MC acceptance calculation (ca.2-3%).
- g) Limited knowledge of the hyperon decay parameters: $\alpha_\Lambda=0.642\pm0.013$ (i.e. 2% uncertainty), $\alpha_{\Sigma^+}=-0.980\pm0.017$ (2%), and $\alpha_{\Sigma^0}=-\frac{1}{3}\alpha_\Lambda=-0.214\pm0.004$ (2%) when averaged over the directions of photon emission. The relation $\alpha_{\Sigma^0}=-\frac{1}{3}\alpha_\Lambda$ is only correct in the Λ rest frame, which can only be determined if both decay particles (p, π^-) are detected; otherwise the effective decay parameter is about $30\pm5\%$ lower due to integration over the emission direction of Λ in the Σ^0 rest frame.

Table 9. Summary of systematic uncertainties. Note that many of the listed uncertainties are common to all observables.

	Σ	E	G	$d\sigma/d\Omega$	P	$C_{x',z'}$	$O_{x',z'}$	$L_{x',z'}$	$T_{x',z'}$
(a) Target pol.		4.3%	4.3%					4.3%	4.3%
(b) Beam pol.	4-5%	2%	4-5%			2%	4-5%		4-5%
(c) Detector	2-3%		2-3%		2-3%	2-3%	2-3%	2-3%	2-3%
(d) Background subtraction	2-3%	2-3%	2-3%	2-3%	2-3%	2-3%	2-3%	2-3%	2-3%
(e) Separation of quasi-free prod.	3-5%	3-5%	3-5%	3-5%	3-5%	3-5%	3-5%	3-5%	3-5%
(f) Normalization				3.5-5%					
(g) Decay param.					2%	2%	2%	2%	2%
Sum (quadratic)	6-8%	6-7.5%	7-9%	5-7.5%	4.5-7%	5-7%	6-8.5%	6-8%	8-10%

7 Summary of Beam Time Request

The run plan is optimized for the KA channel, for which we expect to obtain a complete (and over-) determination of the photo-production amplitude. The settings given in Table 8 are repeated below in summary.

Table 10. Summary of Run time request.

Setting	E_0 (GeV)	P_{el}	E_γ (GeV)	P_γ	Requested Beam time with $H\bar{D}$ (-1500 A)	Requested Beam time with $\bar{H}D$ (+1500 A)
Circ.pol	1.7	80%	0.7-1.6	41-79%	11 days	0 days
	2.6	80%	1.5-2.47	58-79%	14 days	2 days
Lin.pol.	3.0	-	0.7-0.9	89%	3 days	1 day
	3.0	-	0.9-1.1	85%	3 days	1 day
	4.5	-	1.1-1.3	90%	7 days	1 day
	4.5	-	1.3-1.5	87%	7 days	1 day
	5.5	-	1.5-1.7	88%	7 days	1 day
	5.5	-	1.7-1.9	85%	7 days	1 day
	5.5	-	1.9-2.1	82%	8 days	1 day
	5.5	-	2.1-2.3	79%	8 days	1 day

The total run request is 75 days with D polarization and 10 days with H polarization, for a total of 85 days.

Appendix A: Description and Characteristics of the Frozen-Spin HD Target

The FROST target now under development at Jefferson Lab is built on experiences at Bonn and is quite well known to the JLab community. The HD target is a new class of frozen-spin polarized target which the LEGS Collaboration has been developing over the past eight years at Brookhaven National Lab (BNL) for nucleon spin structure measurements ^[41]. This adventure has recently culminated in a series of highly successful data collection periods at LEGS. Here we provide a brief overview of the physics of this new target, report on its in-beam characteristics and discuss the modifications necessary to adapt it for use in the CLAS at JLab.

A.1 Basic HD target physics

An H₂ molecule, which consists of two identical protons, has two spin states with spins either parallel (*ortho*-H₂) or antiparallel (*para*-H₂). Ortho-H₂, which accounts for $\frac{3}{4}$ of room temperature hydrogen, is readily polarized at high magnetic field and low temperature while para-H₂ cannot be polarized. Because the two protons in H₂ are identical particles, para-H₂ is the lowest energy state of the molecule while ortho-H₂ has a temperature-equivalent energy of 172K. At a low temperature, ortho-H₂ decays to the para-H₂ state with a *1/e* time of about 6 $\frac{1}{2}$ days and as a result pure H₂ cannot reach a frozen-spin state.

The HD molecule has no limitations of symmetry and its proton and deuteron spins can be aligned with a magnetic field to an S= 3/2 state. Its lowest energy state is also L=0. With no phonons to couple to the crystal lattice in solid HD, spin-relaxation times are extremely long. While this makes HD a potentially ideal frozen-spin target, it also implies that direct polarization of pure HD would require impractically long preparation times. This limitation is circumvented with a small concentration of ortho-H₂ (on order of 10⁻⁴), which polarizes readily and then transfers its polarization to HD via a spin-spin coupling (between an H in H₂ and an H in HD). After a significant number of ortho-H₂ -to- para-H₂ half-lives (typically, about three months) almost all of the H₂ impurity has decayed to the magnetically inert para-H₂, leaving the HD target in a frozen-spin state.

The D in HD can be polarized in a similar manner, using a similarly small concentration of D₂. The ground state of D₂ is an L=0 state with a superposition of S=0 and S=2. (For historical reasons the ground state is referred to as *ortho*-D₂, even though the S=0 counter-part in hydrogen is called *para*-H₂). The L=0 implies a long relaxation time, which makes this difficult to polarize. However, the S=1 state of D₂ (which is referred to as *para*-D₂) has L=1 and a temperature-equivalent energy of 86K. This polarizes readily and transfers polarization to HD via spin-exchange. *Para*-D₂ decays to the *ortho*-D₂ ground state with a *1/e* time constant of about 18 days, so that after a sufficient number of half-lives, D in HD can also reach a frozen-spin state. However, the degree of D polarization that can be reached in this way is significantly less than the maximum H polarization, due to the smaller magnetic moment of the deuteron ($\mu_D/\mu_H \sim 1/3$).

The equilibrium H and vector-D polarizations that can be reached in this way are given by the Brillouin function,

$$P(x;J) = \frac{2J+1}{2J} \text{ctnh}\left(\frac{2J+1}{2J}x\right) - \frac{1}{2J} \text{ctnh}\left(\frac{x}{2J}\right), \quad \text{where } x = \frac{\mu B}{k_B T}. \quad (\text{a1})$$

Here, J is the nuclear spin, μ the nuclear magnetic moment, B the external magnetic field, T the temperature and k_B is Boltzmann's constant. This function is plotted in figure A1 against the B/T ratio for both H and vector-D. In reaching thermal equilibrium, the population of the $m_D = 0$ substate is the geometric mean of the ± 1 states, $\sqrt{(m_D=+1) \times (m_D=-1)}$. As a result, the deuteron also acquires a degree of tensor polarization given by,

$$P_T(D) = 2 - \sqrt{4 - 3[P_V(D)]^2}, \quad (\text{a2})$$

which is shown as the green short-dashed line in the figure.

The BNL dilution refrigerator and super-conducting magnet system reaches 15 Tesla with a base temperature of about 7 mK. However, other factors limit the temperature of the HD to levels above the refrigerator base value. The decays of the *ortho*-H₂ and *para*-D₂ impurities generate heat. Solid HD has poor thermal conductivity. The cooling of HD and removal of

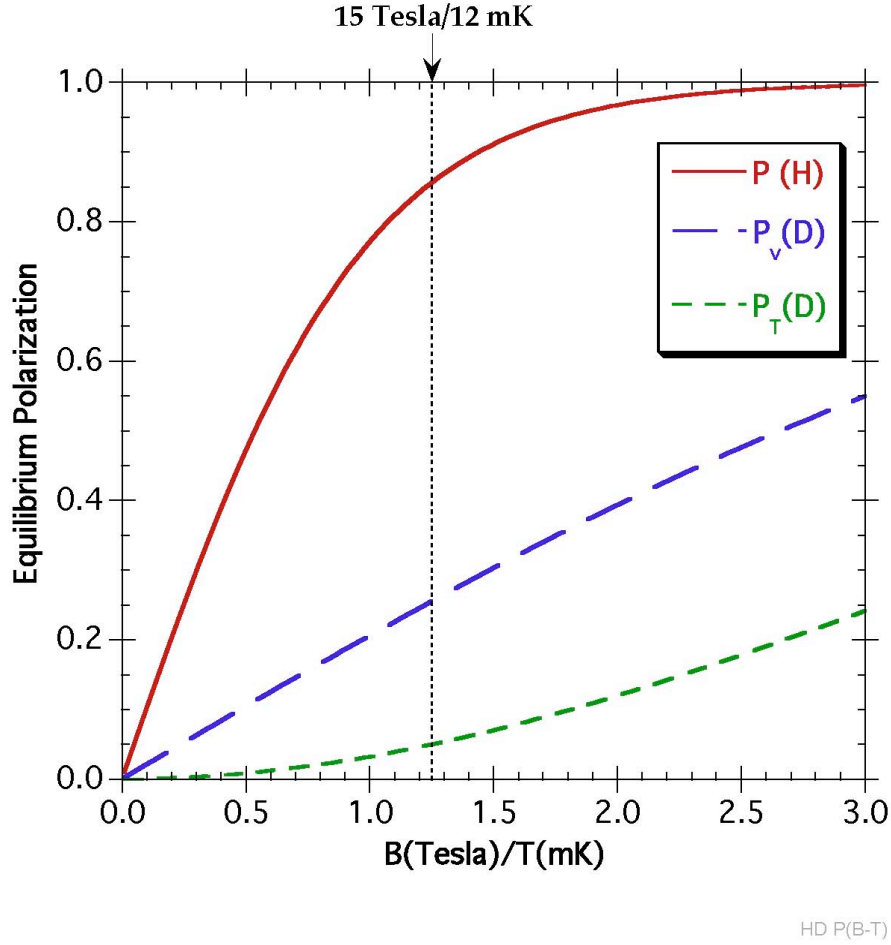


Figure A1. High-field/low-temperature equilibrium polarizations of H and D in HD.

impurity-decay heating is accomplished by imbedding 50 μm diameter aluminum wires within the solid HD. However, at low temperatures, energy is transported through phonons and these experience an impedance mismatch at the HD/Aluminum interface (a *Kapitza* resistance), which limits the HD temperature to about 12 mK. The $B/T = 15$ Tesla/12mK value is indicated by the dotted line in figure A1 ^[42]. So far, a number of competing factors have resulted in target polarizations in BNL that are somewhat smaller than these values. Targets are condensed at 4K where their equilibrium polarizations are measured to calibrate the NMR system. This calibration requires short spin relaxation times (T_1), which are generated by $L=1$ H_2 and D_2 impurities. Once they have been loaded into a copper fixture attached to the mixing chamber of the dilution refrigerator, the HD cools rapidly to about 25 mK, at which point heat from the alignment of spins in the copper fixture and from ortho- H_2 and para- D_2 decays competes with the cooling

power of the refrigerator and slows the cooling. However, T_1 in solid HD increases roughly as B/T and so becomes immediately larger by a factor of about 2400 at 25 mK and 15 Tesla, which slows the growth of polarization. As the ortho- H_2 and para- D_2 contaminants decay, the temperature drops, which raises the limiting equilibrium polarization values, but T_1 continues to grow with time, which in turn slows the growth of polarization. The frozen-spin targets polarized at BNL have had average polarizations of 60% H and 15% vector-D coming out of the refrigerator, which correspond to spin temperatures of 22 mK for H and 20 mK for D, noticeably higher than the 12 mK HD/Al Kapitza limit. The approach to thermal equilibrium is a delicate balance of factors, which if not tuned just right can easily become analogous to a plane chasing a setting sun.

A crucial control factor to the HD polarization process is the concentrations of the H_2 and D_2 contaminants. HD gas of the required purity cannot be purchased, but rather must be extracted by distillation from commercially available HD, which typically has impurity concentrations of a few percent. The HD gas that has been used in the BNL experiments was distilled by collaborators from the University of South Carolina and James Madison University. A cold helium leak that developed in the distillery impeded the production of high quality HD for several years. This has been repaired and HD gas of higher quality than used at BNL has already been produced. This will be used for the JLab experiments. Additional HD gas will be purchased and distilled at James Madison University to ensure adequate contingency supplies.

The initial stage of polarization growth can also be improved by eliminating the spin-heat generated at high fields in the copper fixture holding the targets. This can be accomplished by switching to a silver fixture, which has a much smaller magnetic moment ($\mu_{Ag}/\mu_{Cu} \sim 1/20$). This is planned for use in preparing the JLab targets.

For experiments focusing on D polarization, such as the present proposal, dipole-dipole couplings between neighboring HD molecules allow $P(D)$ to be further increased by transferring polarization from H to D. The Zeeman levels of HD are shown schematically in figure A2. After decay of ortho- H_2 and para- D_2 impurities, with thermal equilibrium conditions frozen in, the population of the $m_D = +1$ substate is greater than that of $m_D = -1$ and the population of $m_D = 0$ is

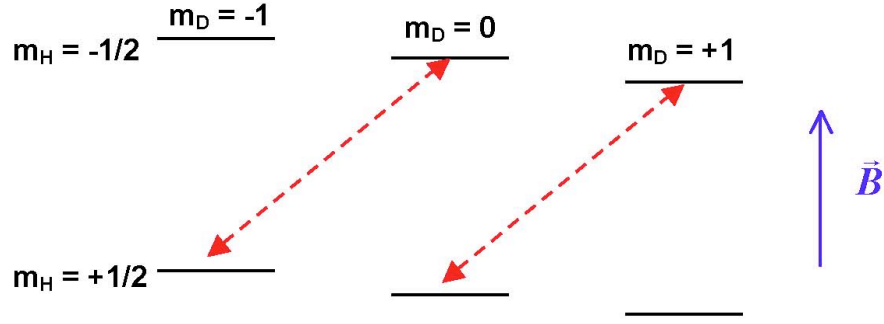


Figure A2. Zeeman splittings in solid HD.

their geometric mean. The *forbidden* RF transitions indicated by the red dashed lines, driven at the difference of the H and D Larmor frequencies, $\nu(\text{H-D}) = 36.0416 \text{ MHz/Tesla}$, move polarization from an H in one molecule to a D in a neighboring molecule with a coupling parameter $0 \leq \epsilon \leq 1$. To leading order, the resulting polarizations are given by,

$$\begin{aligned} P^f(H) &= \left(1 - \frac{4}{3}\epsilon\right)P^i(H) + \epsilon P_V^i(D) + \dots O(P^3) \\ P_V^f(D) &= +\frac{2}{3}\epsilon P^i(H) + \left(1 - \frac{1}{2}\epsilon\right)P_V^i(D) + \dots O(P^3) \\ P_T^f(D) &= +\frac{3}{2}\epsilon P^i(H)P_V^i(D) + \left(\frac{3}{4} - \frac{9}{8}\epsilon\right)P_V^i(D)^2 + \dots O(P^3) \end{aligned} \quad . \quad (\text{a3})$$

The application of RF power will move occupancy from the initially higher-populated levels with $|m_H=+1/2; m_D=-1,0\rangle$ to the $|m_H=-1/2; m_D=0,+1\rangle$ states, increasing D polarization at the expense of H polarization. Such transitions are referred to as *Forbidden* (molecule-to-molecule), *Adiabatic* (with respect to the Larmor frequencies), *Fast* (with respect to the spin-relaxation times) *Passage*, or *FAFP*. If $\epsilon = 1$, 2/3 of the H polarization can be moved to D. However, when $\epsilon < 1$ subsequent RF is not as effective, since the application of RF drives these transitions in both directions.

FAFP transitions require substantially more power than the allowed transitions (within one molecule) used to flip spins. At BNL, *FAFP* transitions with $\epsilon = 70\%$ have been achieved, but on small samples only. If the same RF fields could be maintained over large samples, this would result in a target with $P_V(D)$ in excess of 50%. However, RF field non-uniformity over large

samples becomes a critical factor. With present coil configurations, the RF power required to drive all parts of a large target efficiently would raise the temperature of the dewar containing the sample (due to eddy-current heating and I^2R heating of the leads) and result in an unacceptable loss of frozen-spin polarization. Overcoming this limitation requires a new coil design and modifications to the cryostat. While such R&D is planned for the next few years, it has not been assumed in the simulations discussed in this proposal.

The alternate approach that has been successfully used in LEGS experiments at BNL is to saturate the RF transition to equalize the populations (figure A2) of the $|m_H=+1/2; m_D=-1,0\rangle$ and $|m_H=-1/2; m_D=0,+1\rangle$ substates, $\epsilon=1/2$ in eqn. (a3), which can be carried out over a prolonged period (~ 15 min) with low-power RF that does not introduce excessive heating. This has resulted in targets whose polarization, $P_V(D)$, has been doubled from about 15% to 30%.

As an example, in-beam HD polarizations during a photon-beam experiment at BNL in April'05 are plotted in figure A3. At the start of the running period, RF was used to saturate the

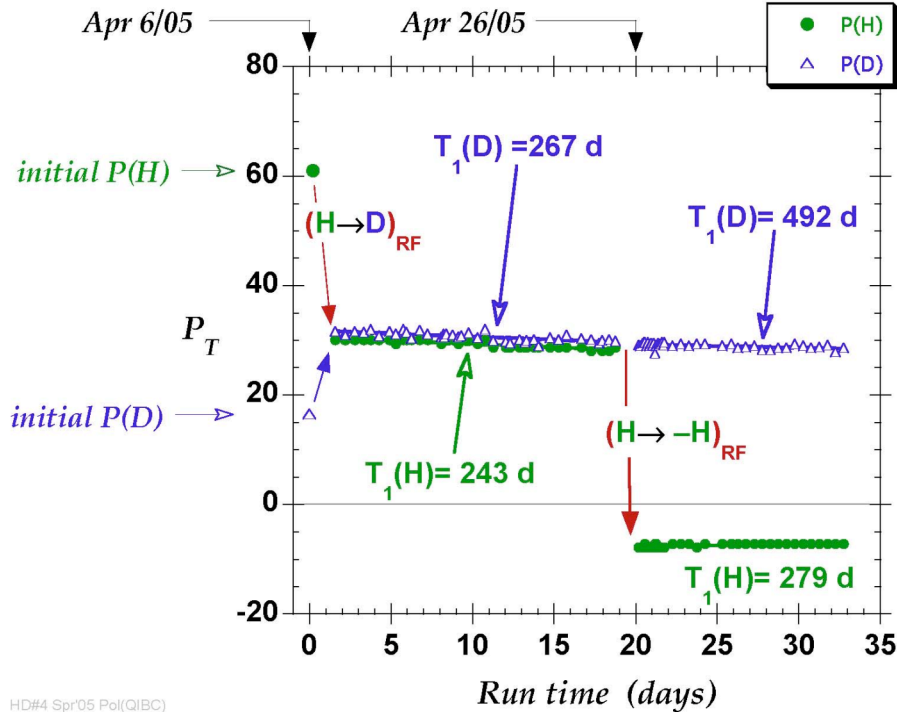


Figure A3. In-beam polarizations during an experiment at BNL in April'05.

forbidden $H \rightleftharpoons D$ transition. This brought both H and D polarizations to about 30%. The spin-relaxation times, T_1 , for both H and D were initially about 9 months. After 20 days running, the H polarization was flipped. (The flip here was incomplete due to a power-supply problem, which has since been corrected.) Data taken after the flip have longer T_1 values, with $T_1(D)$ increasing to 16 months. This reflects the continued decay of the ortho- H_2 and para- D_2 impurities.

A.2 Target geometry

Targets produced at BNL have contained one mole of HD, which at $\sim 1K$ temperatures occupies a cylindrical volume $2.5\text{ cm } \varnothing \times 5.0\text{ cm}$ in length. The same size targets have been used in the simulations in this proposal. (The 5 cm length had been chosen to optimize particle reconstruction resolutions at LEGS. Since the CLAS has higher resolution, longer targets could be used. While tests with a two mole, 10 cm long target are planned for BNL next year, a 5 cm length is assumed here.) A standard BNL target cell is shown to the left of figure A4, together



Figure A4. A typical target cell (left), together with an exploded view of its components.

with an exploded view of its components. The cell walls are made from CTFE (Chlorotrifluoroethylene), C_2ClF_3 , a hydrogen-free polymer that eliminates NMR backgrounds. A short inner and 5 cm longer outer CTFE cell stand the solid HD off from a copper cooling-ring to allow particles emerging at back angles to exit the cell through minimal material. The side walls of the CTFE cylinders are 0.5 mm thick while the faces through which the beam passes are thinned to 0.1 mm. The downstream face of the copper ring has 60 holes, into which are soldered bundles of 36 aluminum cooling wires (99.99% Al, 50 μm \varnothing), for a total of about 2100 wires. One such bundle is shown to the right of figure A4. The mass fractions of material in a standard target cell are listed in table A1.

Table A1. Composition of a standard target cell.

Material	gm/cm ²	mass fraction
HD	0.735	77%
Al	0.155	16%
CTFE	0.065	7 %

The Al and CTFE of the target cell contain the only unpolarizable nucleons and their contributions can be subtracted from runs with the HD removed. As an example, missing energy spectra from BNL data for π^0 -production from the neutron are shown in figure A5.

The target's copper cooling ring (figure A4) has right-hand threads along its outer surface and left-hand threads along its inner bore. These are used in the process of moving the target between dewars. The outer threads maintain thermal contact with one of several cryostats that can hold the target. To move the target between dewars, a Transfer Cryostat with left hand threads on a copper tool cooled to 2K is screwed into the inner bore of the target cell. When these are fully engaged, subsequent left-hand turns unscrew the outer (right-hand) threads and release the target from its holding dewar. Insertion into another cryostat is a similar operation but in reverse order.

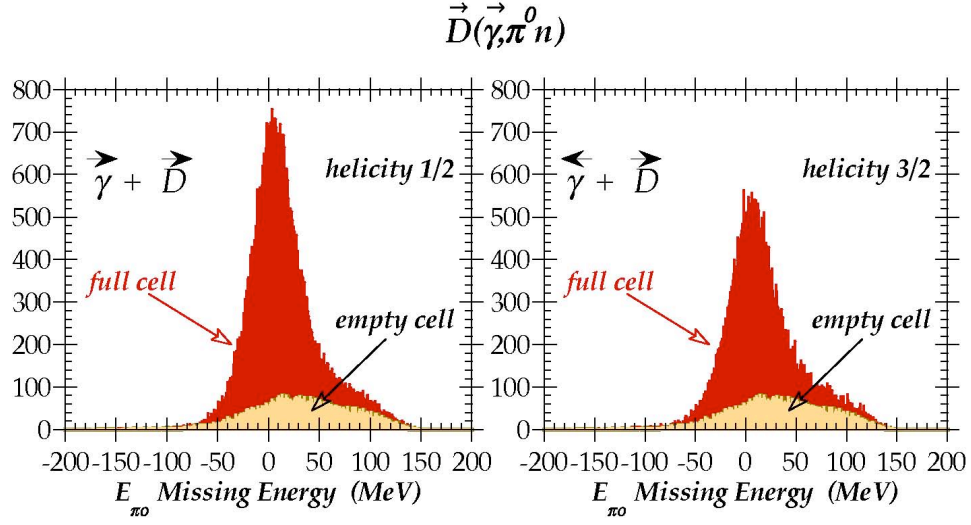


Figure A5. Missing energy spectra from the $\gamma + n(p) \rightarrow \pi^0 + n(p)$ reaction at $E_\gamma = 341$ MeV. The π^0 has been reconstructed from its two decay photons and the neutron has been detected in coincidence. The *full-target* spectra are in red. The flux-weighted yields from the empty cell are indicated.

A.3 HD Polarization and Transfer Protocol

The polarization of HD targets and their use in the present Hall-B experiment requires an involved sequence of steps. The major stages can be summarized as follows:

- High-purity HD gas is condensed into a CTFE cell through a thin capillary, liquefied and frozen in a Production Dewar (PD) at BNL. This dewar has a 2 Tesla magnet with high field uniformity. NMR calibration measurements are made at 4K and 2K where thermal equilibrium is reached in minutes. The equilibrium polarizations are known from the temperature and field.
- A 2K Transfer Cryostat (TC) is used to extract the solid HD target from the PD and load it into one of three positions in a fixture attached to the mixing chamber of an Oxford-1000 dilution refrigerator (DF).
- This sequence is repeated until two or three 5 cm HD targets have been loaded into the DF.
- The DF is cooled and its field is raised to 15 Tesla. The temperature drops to 25 mK in less than half a day. From this point, it currently takes between 10 and 20 days to reach 12 mK depending on gas purity and the number of targets. The use of a silver DF fixture and higher-purity gas will halve this time. The 7 mK base temperature is reached in about 2 months.

- After about 2 months in the DF the HD spins have reached a frozen spin state. At this point, the limiting factor affecting in-beam polarizations is the extraction loss in the warmer and lower-field TC, which operates at 2K and 0.12 Tesla. To minimize transfer and transportation losses, targets for JLab will be aged in the DF at BNL for a total of 5 months.
- After sufficient polarization and aging in the DF, the HD targets are extracted one at a time with the TC and transferred to the PD for NMR determination of their polarization.
- After the post-polarization NMR measurement, targets are moved with the TC from the PD to a Storage Dewar (SD). This cryostat can accommodate up to three 5 cm targets and maintains them at 1.6K and up to 8 Tesla.
- After all targets have been transferred to the SD, this dewar will be loaded into a shock-mounted fixture and onto a truck for transportation to JLab. The field during the ride to JLab will be held between 2 to 3 Tesla to prevent quenches from shocks triggered by road hazards. (This has been successfully tested in a 300 mile trip.) The PD and the TC will accompany the targets to JLab.
- Once at JLab, the 1st target will be transferred from the SD to the PD to re-check its polarization, and then returned to the SD. The SD field will then be raised to 8 Tesla until the start of the experiment.
- Once the In-Beam Cryostat (IBC) has been cooled, the first target will be transferred from the SD to the PD, for an NMR measurement, and then to the IBC. The target will then be transferred back to the PD for a second NMR measurement. The comparison of these NMR results calibrates the transfer loss in the TC. The target will then be transferred back to the IBC, at which point the IBC NMR is calibrated against the polarizations determined in the PD.
- The IBC operates at 250 mK and at a nominal holding field of 1 Tesla. For D-polarization running, polarization will be RF transferred from H to D, as in figure A2. This operation is carried out in the IBC where the temperature can be kept low during this low-field (~500 gauss) operation.
- The IBC with its frozen-spin target will then be rolled into the CLAS for experimental data collection. In-beam NMR provides a continuous measure of polarization during the experiment. We anticipate in-beam deuteron polarizations of at least $P(D) = 40\%$ with spin-relaxation times well in excess of a year.

- Part way through the running period, the H polarization will be flipped with an allowed RF transition to permit the separation of H and D observables for those reactions that are not completely exclusive.
- At the completion of the running period, the target will be removed from the IBC with the TC and transferred to the PD for post-run NMR measurements.
- The 1st HD is finally extracted from the PD and evaporated in the TC.
- The targets remaining in the SD may then be used as needed.

A.4 NMR Polarization Monitoring

A crossed coil NMR polarimeter (CC-meter) is used to monitor nuclear polarization in HD. This contrasts the more commonly used Q-meter circuit. The CC-meter replaces the single coil and resonant circuit of the Q-meter with a pair of coils arranged with orthogonal axes and a pair of associated resonant circuits, although a tuned input circuit is not essential ^[43].

The sensitivity of the circuit to target polarization enters through the dependence of the inductance of a coil on the susceptibility (χ) of the enclosed sample,

$$L = L_0 \left[1 + \eta \chi \right] , \quad (\text{a4})$$

and the constant relating susceptibility to change in inductance, η , is an effective *filling factor* for the target material within the coil. The presence of a polarizable sample increases the small mutual inductance coupling the two coils. For an NMR sample, the susceptibility is a complex valued resonance function (typically Lorentzian or Gaussian) with non-zero value only very near the Larmor frequency.

The voltage transfer function (gain) of the circuit is a rational polynomial in frequency with coefficients that can be expressed in terms of the circuit elements. The response of the polarimeter to polarization can be determined by expanding the voltage gain in a power series in susceptibility,

$$G(\omega) = G_0(\omega) + G_1(\omega) \cdot \chi + G_2(\omega) \cdot \chi^2 + \dots O(\chi^3) . \quad (\text{a5})$$

The first coefficient, $G_0(\omega)$, the gain of the circuit in the absence of a polarized target, is an undesirable background gain on which the signal due to the resonant susceptibility appears. The response to the susceptibility is determined by $G_1(\omega)$, the *transducer gain*. $G_2(\omega)$ is the lowest order non-linearity in the susceptibility response of the circuit, which ideally would be zero. An optimal circuit has G_0 and G_2 small and G_1 large.

Both the CC-meter and the more common Q-meter can be operated in modes where the non-linearities terms of eqn (a4) are small. However, we have found that the CC-meter has the following significant advantages. By proper design, the inductive and capacitive coupling between the two coils can be made very small, so that the background signal under the NMR resonance signal is very small. This leads to small systematic errors in the background subtraction, which result from the inevitable drift of the background during long measurement times. Also, since most of the noise comes from the RF signal source, the low background results in greatly improved signal-to-noise ratios for the CC-meter. The inductances and geometries of the two coils of the CC-meter can be separately optimized to achieve specific requirements (such as greater RF field uniformity over a large target).

To date, NMR spectra at BNL have been generated by sweeping the magnetic field at a fixed frequency. The low-field (~ 0.15 Tesla) and high-temperature (4K) NMR response for solid HD in the PD is shown in figure A6 at the beginning of the target cycle, before high polarization has been generated. Absorptive signals (top panels) and dispersive signals (bottom panels) are related by the Kramers-Kronig dispersion relation and provide an independent measure of polarization.

With conventional targets, the design of an NMR coil that will be used for both H and D is bounded by the conflicting requirements of a large enough Q to compensate for the small D magnetic moment, during the initial thermal equilibrium D calibration, but small enough Q to avoid a large non-linear response to polarized H. In HD, the stoichiometry of the molecule and the precisely known ratio of magnetic moments, μ_D/μ_H , allows the deuteron calibration to be calculated from that of the proton, so that in fact only hydrogen thermal equilibrium measurements are necessary.

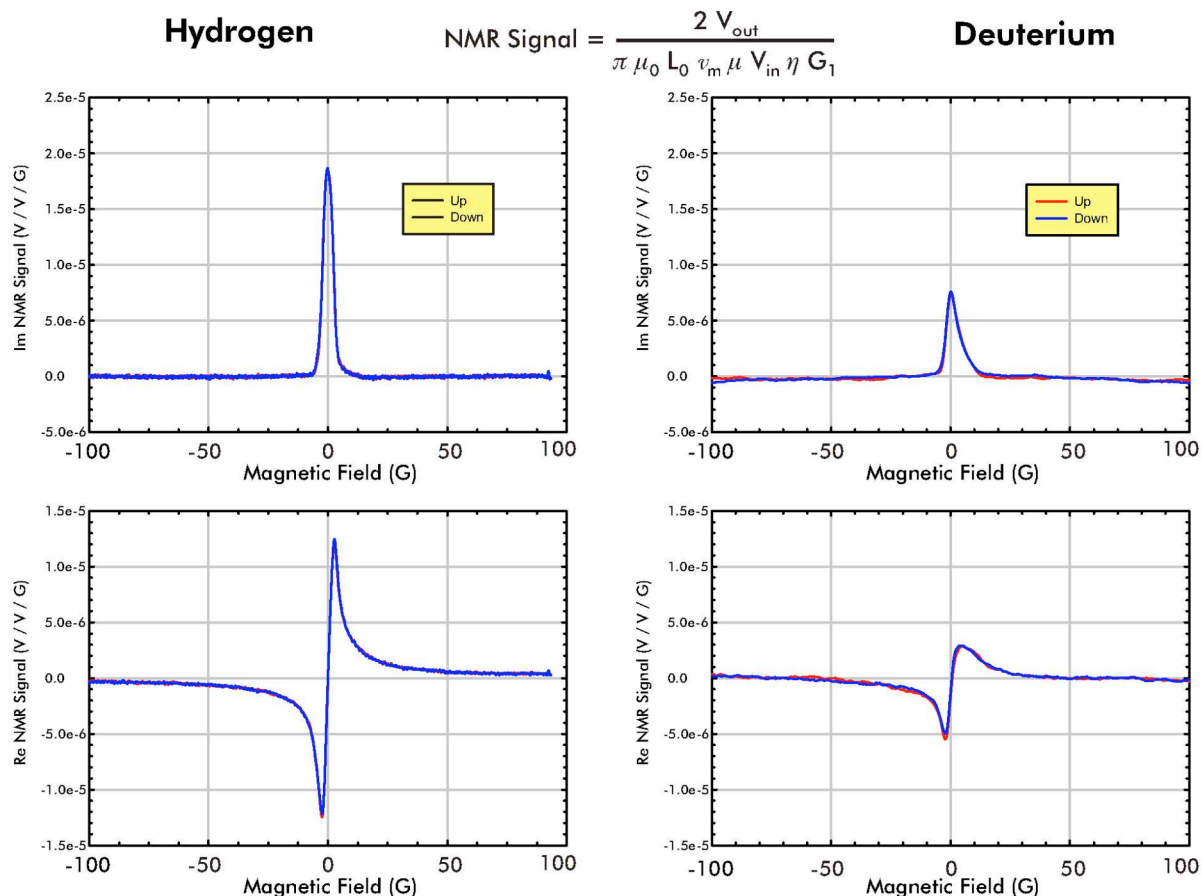


Figure A6. Equilibrium polarizations for H (left panels) and D(right panels) at 4K. Top and bottom panels show the absorptive and dispersive signals, respectively. *Up* and *Down* field sweep traces are plotted separately.

The absorption signal from a single trace over the deuterium NMR line in a 30% D-polarized frozen spin HD target is shown in figure A7. The deuterium NMR line in HD is as simple as the H NMR response. This is in contrast to deuterium signals from deuterated-butanol ($\text{C}_4\text{D}_9\text{OD}$). The latter forms an asymmetric crystal with an electric field gradient which interacts with the deuteron's Quadrupole moment and splits the $m_D = \pm 1$ deuterium substates, resulting in a complex structure. HD on the other hand forms a symmetric hexagonal-close-packed solid with negligible Electric field gradient and no line splitting.

The anticipated accuracy on target polarization is about 4%. A breakdown of the main contributing sources is given in table A2. The largest single contributing factor is the differential uncertainty on the gain of a lock-in amplifier whose scale must be changed by several orders of magnitude between PD equilibrium-polarization measurements and high-polarization frozen-spin measurements. If the gains of this lock-in can be cross-calibrated to another absolute instrument, the total errors can be reduced to about 3%. This will be pursued, but is not assumed for the present proposal.

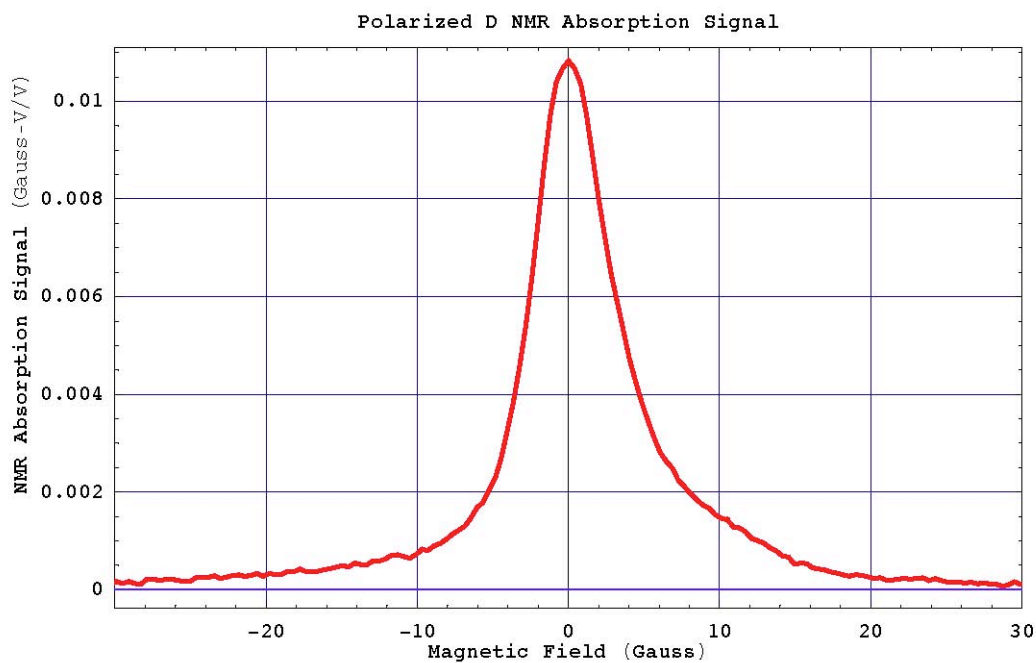


Figure A7. Absorption Deuterium NMR signal from a P(D)=30% frozen-spin HD target.

Table A2. Factors contributing to the systematic error on target polarization.

Source	$\delta P(H)$	$\delta P(D)$
thermal equilibrium calibration - noise, temperature, bkg, ...	0.9%	1.0%
frozen-spin measurement - white noise - holding field noise - non-linearities, homogeneity,...	0.4% 0.5% 1.0%	2.0% 0.5% 1.0%
calibration transfer - circuit drift, differential ramp - Lock-in gain differential error - cold-transfer loss	1.6% 2.8% 1.0%	1.6% 2.8% 1.0%
Total fractional error:	3.7%	4.2%

A.5 In-Beam Cryostat for use in CLAS

The various refrigerators, cryostats, cold-tools and NMR equipment needed to manufacture, calibrate, store and transfer frozen-spin HD targets have been developed at BNL and will be used for the proposed experiment in Hall-B at JLab. The one outstanding piece of equipment is a suitable In-Beam Cryostat (IBC) that can hold the polarized target at the center of the CLAS.

The current LEGS In-Beam Cryostat is a dilution refrigerator that holds an HD target cell threaded onto a mixing chamber that is on the end of a meter long extension in an open geometry with minimal material around the target cell. A thin one Tesla solenoid surrounds the target to maintain longitudinal polarization. However, this IBC is about 30 cm too tall to be used in CLAS. It must either be modified or a new cryostat constructed.

A conceptual design of a modified cryostat is shown in figure A8. In this approach, the 1 meter long, narrow diameter (80 mm) assembly containing 80K, 20K and 2K thermal shields surrounding the mixing chamber and NMR coils would be reused from the BNL IBC. Upstream

of this, a meter long 80K extension would be added. This combination allows use of the existing TC without modification. The inner limit of the region 1 gas-bag is indicated by the red dashed lines. The liquid helium and nitrogen reservoirs, together with the 1K pot and the still, are located in a cylindrical volume that is upstream of the inner drift chambers. This volume would be reduced from that of the BNL IBC so as to fit within the CLAS torus.

Funds have been requested for FY 2007 from DOE to support the design at BNL of a modified/new IBC for use in the CLAS. Pending the approval of this proposal, additional funds will be requested for construction and commissioning.

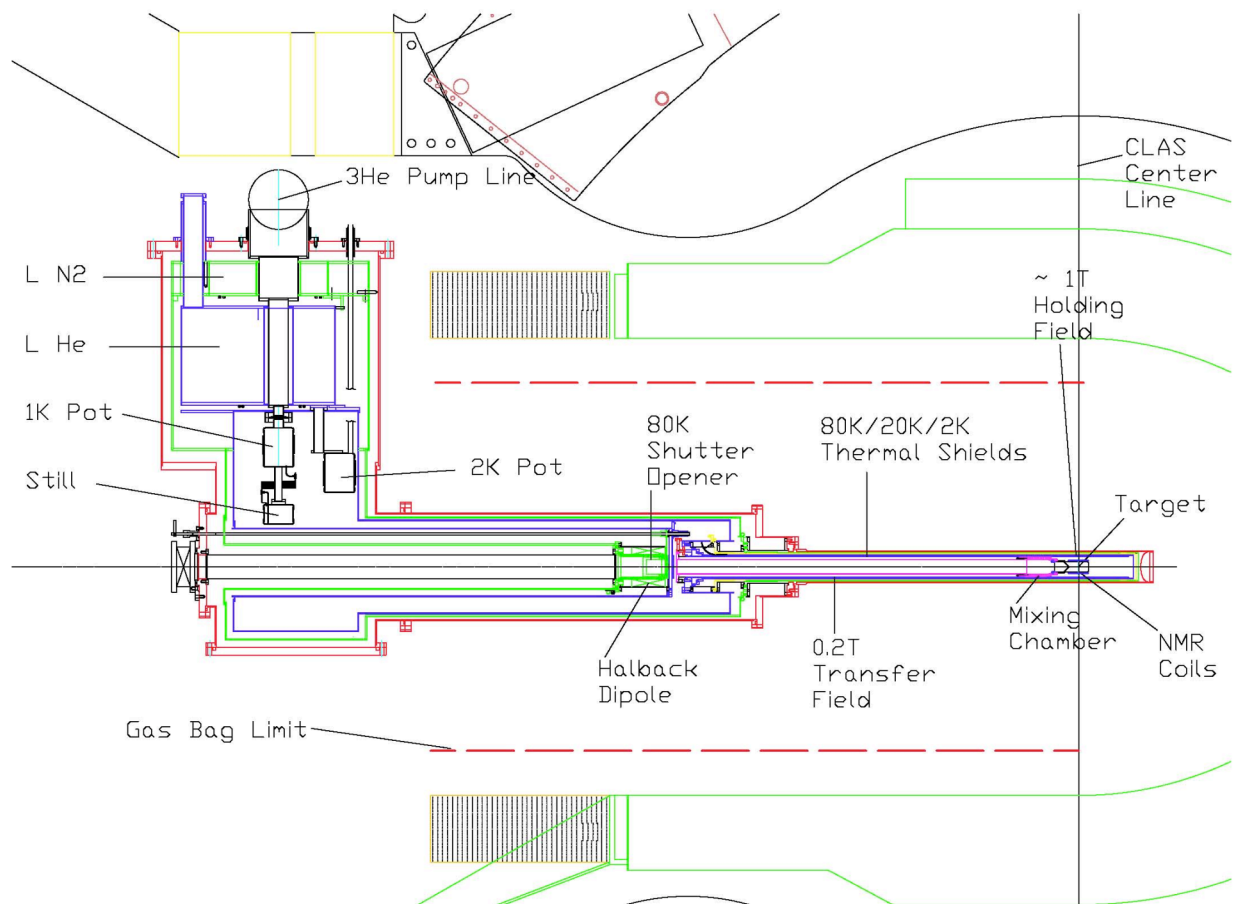


Figure A8. Conceptual design of modified version of the BNL IBC for use in the CLAS.

Appendix B: Relation to other photo-production experiments at JLab

The proposed experiment is closely related to corresponding experiments on unpolarized deuterium and experiments on polarized protons (butanol target).

a) The CLAS-g2 run group comprises 5 approved experiments:

E89-045 “*Studies of Kaon Photoproduction on Deuterium*”
(spokesperson: B. Mecking),

E93-008 “*Inclusive eta Photoproduction in Nuclei*”
(spokesperson: M. Vineyard),

E93-017 “*Study of $\gamma d \rightarrow pn$ and $\gamma d \rightarrow p\Delta^0$ Reactions for Small Momentum Transfers*”
(co-spokespersons: E. De Sanctis, P. Rossi),

E94-008 “*Photoproduction of eta and eta' Mesons from Deuterium*”
(spokesperson: B. Ritchie),

E94-103 “*The Photoproduction of Pions*”
(co-spokespersons: W. Briscoe, J. Ficenec, D. Jenkins).

Data were taken in August/September 1999, collecting 2.4 billion events at $E_0=2.5$ GeV and 3.1 GeV (torus current 3375A) and in May 2003, collecting 700 Million events at $E_0=3.8$ GeV (torus current 2250A). The beam current during both running periods was around 10-13 nA and the tagged photon flux about 70 to 90 MHz.

The reaction $\gamma n(p_s) \rightarrow K^+ \Sigma^-(p_s)$ has been analyzed (E89-045) and is under CLAS internal review, however the statistics is rather poor. Several analyses have been performed with this data to search for exotic baryon states - pentaquarks.⁴⁴

b) Beam time for CLAS-g10 was requested in order to overcome the low statistics of the invariant mass distributions in the pentaquark search from CLAS-g2 data:

E03-113 “*Investigation of Exotic Baryon States in Photoproduction Reactions with CLAS*”
(co-spokespersons: K. Hicks, S. Stepanyan).

CLAS-g10 took data from March 13 to May 16, 2004, at $E_0=3.8$ GeV and collected at each of the torus field settings (2250A and 3375A) roughly 10 times higher statistics than during the CLAS-g2 runs. However, contrary to CLAS-g2, the electron beam was not polarized. CLAS-g10 data have been thoroughly analyzed with respect to the pentaquark search⁴⁵, as well as with regard to other reactions on deuterons and neutrons.⁴⁶ The large data set provides an excellent

basis for cross sections of reactions with at least two charged particles in the final state (CLAS-g10 trigger condition).

c) The Hall-A photoproduction experiment on light nuclei,

E94-104 “*The Fundamental $\gamma n \rightarrow \pi^- p$ Process in 2D , 4He , and ^{12}C in the 1.2-6.0 GeV Region*”
(co-spokespersons: H. Gao, R. Holt),

collected cross section data on charged single pion production at various photon energies between 1.1 and 5.5 GeV in January/February 2001. Since the data was taken at only 2 to 5 production angles between 50° and 110° , this data set can only be used for comparison in limited kinematics.⁴⁷

d) The Hall-B proposal to PAC30,

PR-06 “Kaon Production on Deuteron Using Polarized Photons”,
(co-spokespersons: P. Nadel-Turonski, B. Berman, A. Tkabladze),

is expected to provide a large number of single polarization data (P, Σ , T) and Beam-Recoil double polarization data for $\gamma n \rightarrow K^0 \Lambda$, $K^0 \Sigma^0$, $K^+ \Sigma^-$ using circularly and linearly polarized photons and the CLAS detector. The advantage of this experiment – compared to the proposed experiment using the HD target – is obviously a higher luminosity, realized by a 40cm long deuterium target. This will allow for more accurate measurements as well as data points in forward and backward directions. Data for this experiment can be taken as early as Fall 2006. Its results will provide very useful constraints for models of kaon production and PWA's. However, ambiguities in the determination of the meson-production amplitudes will not be removed. To this end, a polarized-target experiment is required.

e) The FROST run group at CLAS will measure pion and kaon reactions on polarized protons using a butanol target. 89 days of beam time are allocated for this run. Data taking, scheduled for Winter 2006 to Fall 2007, will include all four combination of beam and target polarization. Despite the large background from reactions on bound nucleons, elementary proton processes can be extracted due to the sufficiently large acceptance for charged pion and kaon production. Five experiments form this run group:

E02-112 “*Search for Missing Nucleon Resonances in the Photoproduction of Hyperons Using a Polarized Photon Beam and a Polarized Target*”
(co-spokespersons: F. Klein, P. Eugenio, L. Todor),

E03-105 “*Pion Photoproduction from a Polarized Target*”

(co-spokespersons: S. Strauch, N. Benmouna, W. Briscoe, G. O’Rielly, I. Strakovski),

E04-102 “*Helicity Structure of Pion Photoproduction*”

(co-spokespersons: D. Sober, D. Crabb, M. Khandaker),

E05-012 “*Measurement of Polarization Observables in eta photoproduction with CLAS*”

(co-spokespersons: E. Pasyuk, M. Dugger),

E06-013 “*Measurement of $\pi^+\pi^-$ Photoproduction in Double-Polarization Experiments using CLAS*” (co-spokespersons: V. Crede, M. Bellis, S. Strauch)

f) Our proposed experiment using the HD target is complementary to the FROST program (e) as well as the proposed kaon production proposal on D₂ (d). The scope of our proposal, however, is considerably wider since the proposed HD target runs will allow the collection of a very large number of observables in different reaction channels, from both polarized neutrons and protons, simultaneously with common systematics. For the $\gamma n \rightarrow K^0 \Lambda$ channel in particular, a total of 13 observables from the four polarization sets of single-polarization and beam-target, target-recoil and beam-recoil double-polarization asymmetries will be determined, along with the cross section, in a single experiment. Asymmetries from all four polarization groups are necessary to determine the amplitude; the simultaneous measurement of beam-recoil observables is possible because the target molecule contains a single neutron in deuterium and the small contaminations from non-HD material in the beam path can be subtracted from concurrent empty cell data. This very large combination of measured observables will produce a complete (and over-) determination of the $\gamma n \rightarrow K^0 \Lambda$ amplitude, free from ambiguities. This will be a first in nearly 50 year of pseudoscalar meson production experiments.

-
- 1 S. Capstick and W. Roberts, Phys. Rev. **D47**, 1994 (1993).
 - 2 M. Ida and R. Kobayashi, Prog. Theor. Phys. **36**, 846 (1966);
D.B. Lichtenburg, Nuovo Cimento **A19**, 435 (1967);
J.W. Norbury, Can. J. Phys. **67**, 876 (1989), and references therein.
 - 3 D.B. Leinweber, R.M. Woloshyn and T. Draper, Phys. Rev. **D43**, 1659 (1991).
 - 4 T.D. Cohen and L.Y. Glozman, Int. J. Mod. Phys. **A17**, 1327 (2002).
 - 5 R. Koniuk and N. Isgur, Phys. Rev. **D21**, 1868 (1980).
 - 6 S. Capstick and W. Roberts, Phys. Rev. **D49**, 4570 (1994);
S. Capstick and W. Roberts, Phys. Rev. **D58**, 074011 (1998).
 - 7 K.H. Glander *et al.*, Eur. Phys. J. **A19**, 251 (2004).
 - 8 T. Mart and C. Bennhold, Phys. Rev. **C61**, 012201 (2000).
 - 9 A. Waluyo, Ph.D. thesis, The George Washington University, Washington, D.C. (2005).
 - 10 M.Q. Tran *et al.* (SAPHIR Collaboration), Phys. Lett. **B 445**, 20 (1998);
S. Goers *et al.* (SAPHIR Collaboration), Phys. Lett. **B 464**, 331 (1999).
 - 11 T. Mart, Phys. Rev. **C62**, 038201 (2000)
 - 12 T. Mart, A. Sulaksono and C. Bennhold, Nucl-th/0411035.
 - 13 S. Janssen, J. Ryckebusch, D. Debruyne and T. Van Cauteren, Phys. Rev. **C66**, 035202 (2002).
 - 14 A.V. Sarantsev, V.A. Nikonov, A.V. Anisovich, E. Klempt and U. Thoma, Eur. Phys. J. **A25**, 441 (2005).
 - 15 B. Juliá-Díaz, B. Saghai, T.-S.H. Lee and F. Tabakin, Phys. Rev. **C73**, 055204 (2006).
 - 16 W. Chiang and F. Tabakin, Phys. Rev. **C55**, 2054 (1997);
W. Chiang *et al.*, Phys. Rev. **C68**, 045202 (2003).
 - 17 J.W.C. McNabb *et al.*, Phys. Rev. **C69**, 042201 (2004).
 - 18 R.G.T. Zegers *et al.*, Phys. Rev. Lett. **91**, 092001 (2003).
 - 19 R.A. Arndt, W.J. Briscoe, I.I. Strakovsky and R.L. Workman, Phys. Rev. **C72**, 058203 (2005).
 - 20 H. Dutz *et al.*, Phys. Rev. Lett. **94**, 162001 (2005).
 - 21 H. Dutz *et al.*, Phys. Rev. Lett. **93**, 032003 (2004).
 - 22 F.X. Lee, T. Mart, C. Bennhold, H. Haberzettl, L.E. Wright, Nucl. Phys. **A695**, 237 (2001).
 - 23 W. Roberts and T. Oed, Phys. Rev. **C71**, 055201 (2005).
 - 24 A. Fix and H. Arenhövel, Eur. Phys. J. **A25**, 115 (2005).
 - 25 Y. Assafiri, *et al.*, Phys. Rev. Lett. **90**, 222001(2003).
 - 26 U. Thoma, in: FEW-BODY PROBLEMS IN PHYSICS: The 19th European Conference on Few-Body Problems in Physics, AIP Conference Proceedings 768, 197 (2005).

27 A. Fix and H. Arenhövel, Phys. Rev. **C72**, 064005(2005); *priv. comm.*.

28 J.-M. Laget, Phys. Rep. **69**, 1 (1981); Phys. Lett. **B 259**, 24 (1991); nucl-th/0507035 (2005).

29 T.-S. H. Lee, Phys. Rev. Lett. **50**, 1571 (1983).

30 A. Matsuyama and T.-S. H. Lee, Phys. Rev. **C34**, 1900 (1986).

31 T. Sato and T.-S. H. Lee, Phys. Rev. **C54**, 2660 (1996); *ibid*, **C63**, 055201 (2001).

32 A. Matsuyama, T. Sato, and T.-S. H. Lee, to be submitted for publication in Physics Report.

33 W.-T. Chiang, B. Saghai, F. Tabakin and T.-S.H. Lee, Phys. Rev. **C69**, 065208 (2004).

34 Z. Li and B. Saghai, Nucl. Phys. **A644**, 345 (1998);
B. Saghai and Z. Li, Eur. Phys. J. **A11**, 217(2001).

35 R. Bradford *et al.*, Phys. Rev. **C73**, 035202 (2006).

36 GEANT - Detector Description and Simulation Tool, CERN Program Library W5013,
Geneva, Switzerland (1993).

37 E. Hackett, W. Brooks, CLAS-Note 98-014 (1998); E. Dumonteil, G. Niculescu,
I. Niculescu, CLAS-Note 01-006 (2001).

38 K.-H. Glander *et al.* (SAPHIR Collaboration), Eur. Phys. J. **A 19**, 251 (2004).

39 R. Lawall *et al.* (SAPHIR Collaboration), Eur. Phys. J. **A 24**, 275 (2005).

40 F.A. Natter *et al.*, Nucl. Inst. Meth. Phys. Res. **B211**, 465 (2003).

41 X. Wei, C.M. Bade, A. Caracappa, T. Kageya, F.C. Lincoln, M.M. Lowry, J.C. Mahon,
A.M. Sandorfi, C.E. Thorn, C.S. Whisnant, NIM A526 (2004) 157, and references therein.

42 LEGS Spin Collaboration, M. Lowry *et al*, Workshop on *Testing QCD through Spin Observables*
in Nuclear Targets, University of Virginia, World Scientific (2002).

43 A. Caracappa and C. Thorn, *Proceedings of 15th International Spin Symposium*,
Brookhaven National Lab, Upton, New York, AIP 675, 867 (2002).

44 S. Stepanyan *et al.*, Phys. Rev. Lett. **91**, 252001 (2003).

45 B. McKinnon *et al.*, Phys. Rev. Lett. **96**, 212001 (2006); S. Niccolai *et al.*,
submitted to Phys. Rev. Lett.

46 CLAS Approved Analyses : P. Rossi ($\gamma n \rightarrow \pi^+ p$), P. Nadel-Turonski ($\gamma n \rightarrow K^0 \Lambda$),
D. Tedeschi ($\gamma n \rightarrow \Phi n$).

47 L.Y. Zhu *et al.*, Phys. Rev. **C 71**, 044603 (2005).